Bayreuth University
Department of Micrometeorology

Quality assessment of Eddy Covariance measurements above Tibetan Plateau grasslands

STEFAN METZGER

Diploma thesis in the study course of Geoecology
Supervisor: Prof. Dr. Thomas Foken

Bayreuth, 30 April 2007

Abstract

The Institute of Tibetan Plateau Research, Chinese Academy of Sciences, investigates the turbulent fluxes of sensible and latent heat as well as CO_2 under typical grazing conditions of the Tibetan grassland at altitudes up to 4745 m above sea level. For the two sites under investigation, Eddy Covariance flux measurements are set up at 3 m height above ground in addition to nearby PBL-, Wind Profiler- and Radio Acoustic Sounding System observations. Besides the Campbell CSAT-3 sonic anemometer and the LICOR-7500 infrared gas analyzer, instrumentation consists of radiation instruments for shortwave (Kipp & Zonen CM3) and longwave (Kipp & Zonen CG3) components along with soil heat flux measurements (Hukseflux HFP01). The datasets available almost cover a span of one year and therewith allow, besides assessment of the diurnal cycles, statements on the annual cycles including phenomena such as the Asian monsoon. After a high resolution land use classification based on satellite-imagery and ground verification a subsequent quality analysis including tests on stationarity, integral turbulence characteristics and footprint modeling has revealed spatial and temporal structures in the quality of the Eddy Covariance measurements. Vertical wind analysis revealed that up to 1/4 of the measurements do not fulfill assumptions necessary for a physically correct data processing. Despite this fact, flux measurements in general fulfill the quality test criteria to an extent that ≈50 % of the results can be regarded as suitable for fundamental research. Further, footprint analysis confirms high representativity of the flux measurements for the grassland component and revealed sectors of compromised data quality. Part of the latter could be interpreted as related to instrument set up, for what measures are proposed to improve data quality. Remaining indications could not be entirely explained due to local topography. Investigations of the energy balance revealed a non-closure of more than 30 % of the net radiation. Primary reasons are believed to be the regional topography leading to advection and unconsidered turbulent fluxes due to wavelengths longer than the averaging interval. Supplemented findings of Wind Profiler and Radio Acoustic Sounding System observations include the detection of two wind shears at 500 m and 1500 m above ground and the phenomenon of glacier wind with a reversed compensatory flow reaching up to 2000 m above ground. Together with the results from Eddy Covariance quality assessment, this gives way to the hypothesis of mesoscale flow patterns that contribute organized structures of long wavelength to the boundary layer affecting representativity of Eddy Covariance results.

Zusammenfassung

Das Tibet Plateau Forschungsinstitut der Chinesische Akademie der Wissenschaften untersucht den sensiblen und fühlbaren Wärmestrom sowie den CO_2 Fluss unter typischen Beweidungsintensitäten der Tibetischen Magerrasen auf Höhen bis zu 4745 m über Meeresspiegel. Für die beiden Untersuchungsgebiete dieser Studie sind hierzu neben den nahe gelegenen Profilmesstürmen, Wind Profiler und Radio Acoustic Sounding Systemen Eddy Kovarianz Messungen auf 3 m über Gelände angebracht. Außer dem CSAT-3 Ultraschallanemometer der Firma Campbell und dem Infrarot Gasanalysator LICOR-7500 besteht die Instrumentierung aus Strahlungsmessgebern für die kurzwellige (Kipp & Zonen CM3) und langwellige (Kipp & Zonen CG3) Komponente sowie einer Bodenwärmestromplatte (Hukseflux HFP01). Die verfügbaren Datensätze umfassen jeweils nahezu ein Jahr und erlauben dadurch neben der Auswertung von Tagesgängen Aussagen zum Jahreszyklus, was Phänomene wie den Asiatischen Monsun einschließt. Nach einer hochauflösenden satelliten- und bodengestützten Klassifizierung der Landnutzung wurde eine Qualitätsanalyse durchgeführt. Diese deckt an Hand von Tests zu Stationarität, integralen Turbulenzcharakteristiken und Footprint Modellierung räumliche und zeitliche Strukturen in der Qualität der Eddy Kovarianz Messungen auf. Hierbei zeigt die Analyse des Vertikalwindes, dass bis zu 1/4 der Messungen nicht die Annahmen erfüllen, welche für eine physikalisch korrekte Datenverarbeitung vorausgesetzt werden. Ansonsten erfüllen die Flussmessungen die Qualitätskriterien in soweit, als dass im Mittel ≈50 % der Ergebnisse als tauglich für die Grundlagenforschung erachtet werden können. Die Footprint Analyse bestätigt die Repräsentativität der Messungen für Weideland und zeigt Sektoren auf, in denen grundlegende Annahmen nicht erfüllt sind. Ein Teil dieser Sektoren wird auf die Störung des Strömungsbildes durch Anbringung der Instrumente zurückgeführt, wofür Maßnahmen zur Qualitätsverbesserung vorgeschlagen werden. Die verbleibenden Störungen lassen sich jedoch nicht alleine durch Einflüsse der lokalen Topografie erklären. Des Weiteren zeigen Untersuchungen zur Energiebilanz eine nicht-Schließung von bis über 30 % der Strahlungsbilanz. Als Hauptursachen werden Advektion in Folge der regionalen Topografie und Nichtberücksichtigung von Flussanteilen aufgrund von Wellenlängen längerer als das Mittelungsintervall vermutet. Ergänzende Untersuchungen von Wind Profiler und Radio Acoustic Sounding System für eine Station zeigen Scherwinde auf 500 m und 1500 m über Grund und Gletscherwind mit einem Ausgleichsfluss auf bis zu 2000 m über Grund. Zusammen mit den Erkenntnissen aus der Eddy Kovarianz Qualitätsanalyse lässt sich so die Hypothese eines mesoskaligen Fließregimes formulieren, welches organisierte Strukturen großer Wellenlängen in die atmosphärische Grenzschicht einbringt und somit die Repräsentativität der Eddy Kovarianz Ergebnisse beeinträchtigt.

Contents

List of notation

a	absolute humidity	$[kgm^{-3}]$
a.g.l.	above ground level	
a.s.l.	above sea level	
BST	Beijing Standard Time	
c	CO_2 concentration	$[mmolm^{-3}]$
c_1	Magnus c.: 22.46 ($t<0$) or 17.62 ($t>0$) respectively	[-]
c_2	Magnus c.: 272.62 ($t<0$) or 243.12 ($t>0$) respectively	[°C]
CAMP	Asia–Australia Monsoon Project	
CAS	Chinese Academy of Sciences	
CMA	Chinese Meteorological Administration	
c_p	specific heat at constant pressure	$[Jkg^{-1}K^{-1}]$
ΔQ_s	storage term	$[Wm^{-2}]$
E	East	
e	water vapor pressure	[hPa]
E	Saturation water vapor pressure	[hPa]
EC	Eddy Covariance	
F	Footprint period, followed by an index	
g	gravity acceleration	$[ms^{-2}]$
GAME	Asian Monsoon Experiment	
GLCF	Global Land Cover Facility	
GPS	Global Positioning System	
ITP	Institute of Tibetan Plateau Research	
L	longwave radiation	$[Wm^{-2}]$
$l\uparrow$	outgoing longwave radiation	$[Wm^{-2}]$
$l\downarrow$	incoming longwave radiation	$[Wm^{-2}]$
LAI	Leaf Area Index	[-]
MORP	Monitoring and Research Platform	
N	North	
NEE	Net Ecosystem Exchange	$\mu molm^{-2}s^{-1}$
p	atmospheric pressure	[hPa]
PBL	Planetary Boundary Layer	
p_R	atmospheric pressure at reference station	[hPa]
p_S	atmospheric pressure at station under investigation	[hPa]
q	specific humidity	$[kgkg^{-1}]$
Q_C	CO_2 flux	$[mmolm^{-2}s^{-1}]$
Q_E	latent heat flux	$[Wm^{-2}]$
Q_G	ground heat flux	$[Wm^{-2}]$
Q_H	sensible heat flux	$[Wm^{-2}]$
$-Q_s^*$	surface radiation balance	$[Wm^{-2}]$

R	Planar Fit Rotation period, followed by an index	
R_L	gas constant of dry air	[Jkg^{-1}K^{-1}]
R_v	gas constant for water vapor	[Jkg^{-1}K^{-1}]
S	South	
S	extraterrestrial radiation	[Wm^{-2}]
$s\uparrow$	outgoing shortwave radiation	[Wm^{-2}]
$s\downarrow$	incoming shortwave radiation	[Wm^{-2}]
S_0	solar constant	[Wm^{-2}]
SRTM	Shuttle Radar Topography Measurement	
T	temperature	[K]
t	temperature	[°C]
t	time	[s]
TK2	Turbulence Knight 2	
T_L	temperature at Lhasa reference station	[K]
TP	Tibetan Plateau	
T_R	temperature at reference station	[K]
T_S	temperature at station under investigation	[K]
T_s	sonic temperature	[K]
u	horizontal wind in mean wind direction	[ms^{-1}]
u_*	friction velocity	[ms^{-1}]
W	West	
w	vertical wind speed	[ms^{-1}]
x	scalar atmospheric quantity	
y	scalar atmospheric quantity	
z_a	aerodynamic measurement height	[m]
z_{a_N}	aerodynamic measurement height for N half space	[m]
z_{a_S}	aerodynamic measurement height for S half space	[m]
z_o	roughness length	[m]
z_p	vegetation height	[m]
z_s	snow height	[m]
α	Planar Fit Rotation coefficient	[-]
β	Planar Fit Rotation coefficient	[-]
ε	emissivity	[-]
γ	vertical temperature gradient	[Km^{-1}]
γ	Planar Fit Rotation coefficient	[-]
λ	heat of evaporation	[Jkg^{-1}]
θ	solar zenith angle	[°]
ρ	air density	[kgm^{-3}]
σ	Stefan-Boltzmann constant	[Wm^{-2}K^{-4}]
τ	optical depth of atmosphere	[-]
ξ, ψ	horizontal distances in a orthogonal coordinate system	[m]

1   Introduction

Land surface - atmosphere interaction processes play an important role in the energy and matter cycles, such as that of CO_2 and water, over a wide magnitude of scales. Considerable deficit exists concerning the ability to properly describe these processes, especially in high elevation environments, which among others leads to systematically biased assessment of climate anomalies by numerical models.

With an elevation of more than 4000 m above sea level (a.s.l.) in average, the Tibetan Plateau (TP) represents the most prominent and complicated highland on the globe, making up approximately one-fourth of the land area of China (Ma et al., 2007). Investigations on the TP have shown that the giant prominence exerts thermal effects on the atmosphere, withal influencing circulations over China and Asia, where a major part of world population lives today, and even the globe (Ye and Wu, 1998). Due to its topography, the plateau surface absorbs a large amount of solar radiation energy and undergoes tremendous seasonal changes of surface heat and water fluxes (Ye, 1981; Yanai et al., 1992). The lack of quantitative understanding of interactions between the land surface and atmosphere makes it difficult to understand the complete energy and water cycles over the TP and their effects on the Asian monsoon system by means of numerical models. Therefore the number of land surface processes studies over the TP has increased in the past 30 years, unfortunately only carried out at the local level for short periods during summer with limited observational instrumentation (Gao et al., 1981; Zhang et al., 1988). In the first place the observations during the Asian Monsoon Experiment on the TP (GAME-Tibet) from 1996 to 2000 and the Asia–Australia Monsoon Project on the TP from 2001 to 2005 (CAMP-Tibet) provide comprehensive datasets for the study of energy and water cycle over the TP (Ma et al., 2003).

As to initiate a continuous data collection of high precision and resolution, the Institute of Tibetan Plateau Research (ITP) was founded by the Chinese Academy of Sciences (CAS) in 2003 with three campuses in Lhasa, Beijing and Kunming. For the study of the land surface and atmospheric processes the Monitoring and Research Platform (MORP) is currently being established and set up over the TP area (Figure 1-1). The instrumentation of the sites will among others consist of Planetary Boundary Layer (PBL) towers, radiation measurement systems, wind profiler, Radio Acoustic Sounding Systems (RASS) and Eddy Covariance (EC) measurements including CO_2 and H_2O probes. Two stations, namely Namco (Figure 1-1: Nam Cuo) and Everest (Figure 1-1: Mt. Qomolangma) have already been established at the initiation of this study and provide the data for this study from August 2005 on (Ma et al., 2007).
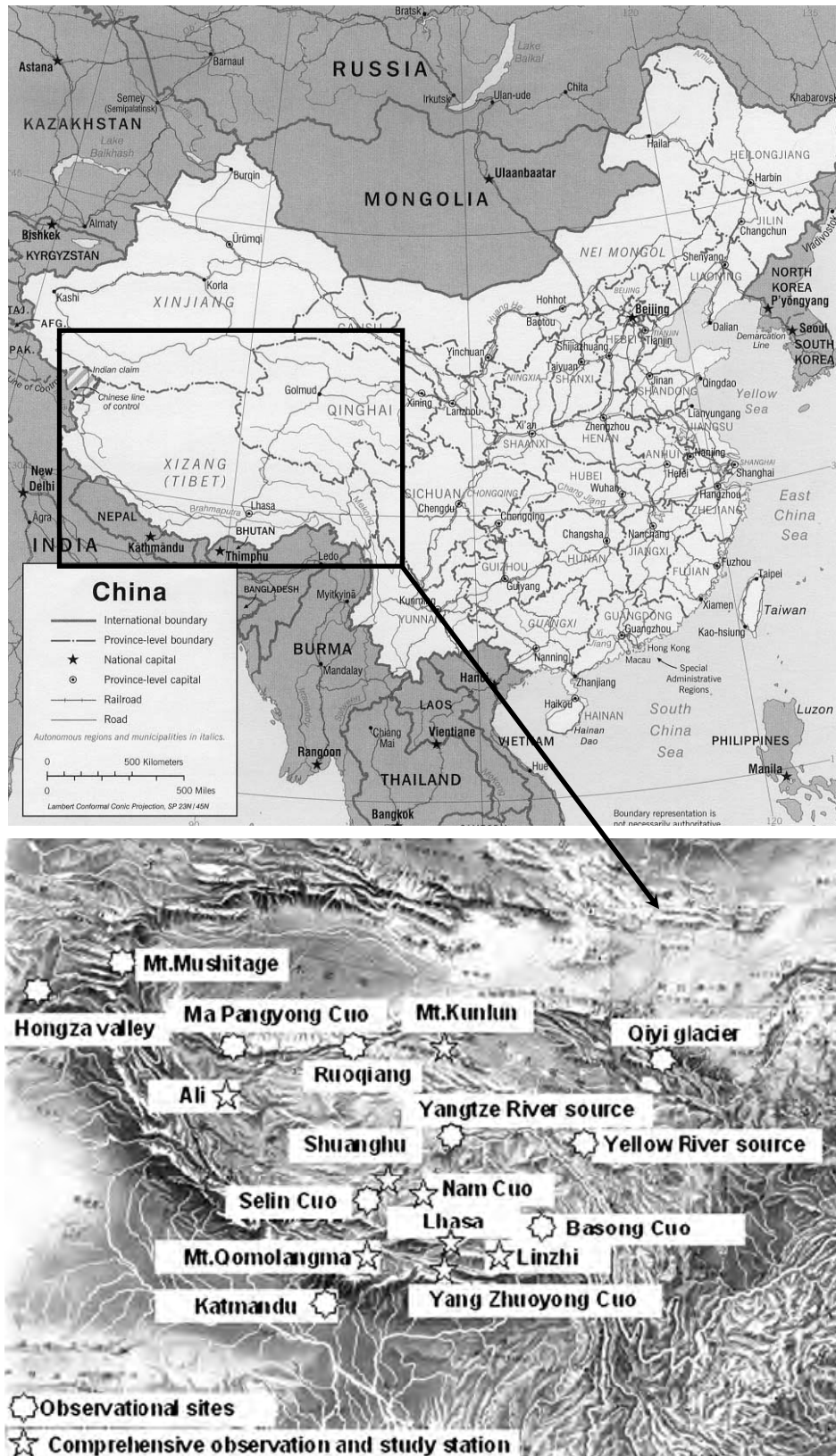
Figure 1-1: Above: China at a glance (Central Intelligence Agency, 2001); below: Monitoring and Research Platform (MORP) with eight comprehensive observation and study stations and 10 observational sites over the TP area, no scale given (Ma et al., 2007).

1.1 Motivation and problem formulation

The EC method is the best measurement technique currently available for the integrative determination of matter and energy fluxes between the atmosphere and the underlying surface of entire ecosystems. Therefore, EC method has become a widely accepted tool for the determination of matter and energy fluxes, applied by several flux networks such as Ameriflux, AsiaFlux, ChinaFLUX, EUROFLUX and KoFlux, overall coordinated within FLUXNET (Baldocchi et al., 2001), whereas the MORP is not yet integrated.

However, EC method is rarely used at alpine grassland stations and much of the research, in particular regarding CO_2 fluxes, is carried out at elevation below 3400 m a.s.l. (Xu et al., 2005b; Xu et al., 2005c; Zhao et al., 2005a; Hirota et al., 2006; Kato et al., 2006; Li et al., 2006b; Zhao et al., 2006), not least due to logistic conditions and metrological challenges increasing with altitude and pronounced topography. The latter arise from assumptions of the EC method such as homogenous terrain, steady state conditions and full developed turbulence. In general problems are demonstrated by the widespread shortfall of the sum of latent and sensible heat fluxes measured by the EC method as compared to the available energy (Wilson et al., 2002), the suspected underestimation of nighttime ecosystem respiration during calm and stable conditions (Gu et al., 2005a), and the inability of the EC method to match net ecosystem production estimates derived independently from carbon inventories (Barford et al., 2001; Curtis et al., 2002; Ehman et al., 2002). While these problems are not fundamentally linked to complex terrain, they may be aggravated by it (Finnigan et al., 2003; Hammerle et al., 2007). It now appears that the development of an automated quality control and site characterization procedure (Rebmann et al., 2005; Göckede et al., 2006) has shown that non-ideal conditions are common for a wide range of sites. The procedure consists of quality tests (Foken and Wichura, 1996; Foken et al., 2004) in combination with a forward Lagrangian footprint model (Rannik et al., 2000; Rannik et al., 2003a) using detailed terrain data gathered by remote sensing methods. Quality tests cover e.g. steady state and developed turbulence assumptions and lead to an overall flagging of the flux data quality. Footprint modeling defines the spatial context of these fluxes, thereby the quality flags can be allocated to different wind directions under varying meteorological conditions.

Thus, this procedure enables for the detection of compromised measurements and the interpretation of their origin and cause, so as to commence measures improving the survey. Accordingly, high-quality data sets for the assignment of these fluxes to different land use types on landscape scale can be collected, not until now leading to representative ground truth for the amendment of numerical models. For this reason, Energy and water cycles over the TP and their effects on atmospheric circulations and water cycle over China, Asia and the globe can be understood more accurate, only

now allowing for the currently best possible formulations of sustainable management practices.

Consequently, this study aims at:
- ⇨ Derivation of the fluxes of sensible- and latent heat, momentum and CO_2 for annual time series of Namco and Everest station employing EC methodology.
- ⇨ Quality evaluation of turbulent flux- and radiation measurements regarding setup and terrain effects.
- ⇨ Formulation of measures to improve the data quality.

Herewith for the first time an extensive assessment of the extent the EC method can be applied to the conditions of shallow PBL, low pressure and absolute humidity and extreme daily and seasonal cycles of temperature and stratification as found on the TP is given for sites at elevations up to 4745 m a.s.l..

1.2 Collaboration

The framework for this study has been established by the collaboration of the Department of Micrometeorology, University of Bayreuth, and the ITP, CAS. A leadoff visit to the ITP laboratories in Beijing and the exchange of first datasets took place in spring 2006. In autumn 2006, preliminary results were presented at the International workshop on energy and water cycle over the TP in Lhasa. The workshop was followed by a field trip, including the examination of the Namco and Everest sites and the remapping of their adjacence, carried out on base of CAS land use data. Whilst a last visit to Beijing, the overall datasets of this survey were transferred and revised results were presented to affiliated institutes of the ITP, such as the State Key Laboratory of Numerical Modeling for Atmosphere Sciences and Geophysical Fluid Dynamics, Institute of Atmospheric Physics, CAS, the Chinese Academy of Meteorological Sciences, China Meteorological Administration and the School of Geography, Beijing Normal University.

Besides bilateral contributions of the collaborators, this survey was supported by the German Academic Exchange Service program 'Overseas Graduation Thesis' and the University Association Bayreuth.

2 Theory

Strictly speaking, EC method is exclusively defined for homogenous terrain. Anyhow, recently EC studies in heterogeneous terrain increase, whereat high alpine grassland sites are among them because of the eminent influence of topography.

2.1 Eddy Covariance investigations of high alpine grasslands

The first EC measurements on grasslands beyond 4000 m a.s.l. at altitude have commenced during the GAME-Tibet campaign from 1996 to 2000, whereat instrumentation includes the setup of two EC towers in central Tibet near Naqu and Amdo at elevations surpassing 4500 m a.s.l. and 4700 m a.s.l. respectively. The overall goal of GAME-Tibet is to clarify the interactions between the land surface and the atmosphere over the TP in the context of the Asian monsoon system (Ma et al., 2003). Hereby subsequent analysis include the determination of surface roughness length (z_0) and energy fluxes (Gao et al., 2000), differentiation of fluxes during monsoon- and non-monsoon season (Tanaka et al., 2001), energy balance closure studies (Tanaka et al., 2001; Tanaka et al., 2003), the parameterizations of the sensible heat flux for modeling reasons (Gao et al., 2003), a comparison of the EC and flux variance method (Choi et al., 2004), a test on the applicability of the band-pass covariance technique to portable flux measurements (Asanuma et al., 2005) and various upscaling and modeling approaches (Ma et al., 2002; Yang et al., 2004; Hu et al., 2006; Ma et al., 2006).

The subsequent CAMP-Tibet campaign from 2001 to 2005 continues the EC measurements on the TP with more precise objectives. Those are the observation of local circulation and its impact on plateau scale water- and energy cycle and the establishment of quantitative observational methods for derivation of the entire water and energy cycle between land surface and atmosphere with the aid of remote sensing methods (Ma et al., 2003). Consequently, important achievements include the investigation of the turbulence structure and transport characteristics in the surface layer (Li et al., 2006a) and the comparison of regional distributions of surface variables and their inter-monthly variations derived from satellite data with field observation data (Ma et al., 2003; Ma et al., 2005; Ma et al., 2007).

The MORP aims at providing a basis for expansion of the CAMP-Tibet objectives from the mesoscale observation area to plateau scale. Therefore, eight new comprehensive observation and study stations including EC measurements are currently being established and set up over the TP area (Figure 1-1). As a first achievement, preliminary Quality Assessment (QA) has been introduced for two EC stations (Metzger et al., 2006).

Besides the forenamed infrastructure, two high alpine grassland sites have been established on the TP in association with ChinaFLUX, being part of the Chinese Ecosystem Research Network (CERN) and affiliated to FLUXNET. In contrast to the forenamed campaigns, the ChinaFLUX objectives more focus on the determination of

controlling mechanism on ecosystem carbon and water cycle and the validation of soil-vegetation-atmosphere models (Yu et al., 2005; Yu et al., 2006a). Hereby Haibei Research Station was set up in 2002 in the NE of the TP, consisting of three flux towers at altitudes around 3300 m a.s.l.. Major achievements include the decomposition of net ecosystem CO_2 exchange (NEE) into its constituents and the calculation of ecosystem respiration (Kato et al., 2004a; Kato et al., 2004b; Xu et al., 2005b; Zhao et al., 2005a; Fu et al., 2006; Kato et al., 2006; Zhao et al., 2006), further the explanation of diurnal and annual variations in CO_2 emission and CO_2 absorption as controlled by photosynthetically active radiation (PAR) and temperature (Gu et al., 2003; Gu et al., 2005b; Gu et al., 2005c; Li et al., 2006b).

The worlds highest FLUXNET station was set up in 2003 at 4250 m a.s.l. near Dangxiong in the S of the TP. Major fields of research include the modulation of NEE rates by the interaction of Leaf Area Index (LAI) with PAR (Xu et al., 2005a; Xu et al., 2005c; Shi et al., 2006; Xu et al., 2006) and the development of a carbon dynamics model for alpine grasslands in response to the high-irradiance environment (Zhang and Tang, 2005). Due to comparison of the forenamed FLUXNET sites, differences in carbon source/sink between different types of vegetation in the TP alpine meadow ecosystem and their relatively high CO_2 release potential have been revealed (Zhao et al., 2005b).

On international level, EC method is rarely used at comparatively high alpine research stations, simply due to the lack of corresponding topography. To make an exception, the FLUXNET station of at Niwot Ridge, USA (Huxman et al., 2003; Turnipseed et al., 2003; Turnipseed et al., 2004), is set up at 3050 m a.s.l., but here the ecosystem is a coniferous forest and for this reason not comparable to the present study.

Whereas the Chinese FLUXNET sites follow approved data quality control steps (Aubinet et al., 2000; Foken et al., 2004; Yu et al., 2006a; Yu et al., 2006b), yet no comparable measures have been carried out for the GAME-Tibet and CAMP-Tibet EC data, possibly leading to misinterpretations (Tanaka et al., 2003). For the reason of proper ground truth verification of satellite based upscaling approaches, a thorough QA shall be introduced with this study to the MORP EC data from the very first.

2.2 Energy balance

The MORP aims at the metrological determination of ground truth data to improve our understanding of the water and energy exchange between land surface and atmosphere by means of remote sensing methods (Ma et al., 2003), which in turn are a consequence of the surface radiation balance (Equation 2-1).

$$-Q_s* = s\uparrow + s\downarrow + l\uparrow + l\downarrow$$ Equation 2-1

employing:

$l\uparrow$	outgoing longwave radiation	[Wm^{-2}]
$l\downarrow$	incoming longwave radiation	[Wm^{-2}]
$s\uparrow$	outgoing shortwave radiation	[Wm^{-2}]
$s\downarrow$	incoming shortwave radiation	[Wm^{-2}]
$-Q_s*$	surface radiation balance	[Wm^{-2}]

The non radiative emitted excess of energy $-Q_s*$ is converted into turbulent energy and soil heat flux according to Equation 2-2.

$$-Q_s* = Q_H + Q_E + Q_G + \Delta Q_s$$ Equation 2-2

employing:

Q_E	latent heat flux	[Wm^{-2}]
Q_G	ground heat flux	[Wm^{-2}]
Q_H	sensible heat flux	[Wm^{-2}]
$-Q_s*$	surface radiation balance	[Wm^{-2}]
ΔQ_s	storage term	[Wm^{-2}]

The method for a direct derivation of the turbulent fluxes will be introduced in the following.

2.3   Eddy Covariance method

The QA of measurements conducted with the EC method is object of this study. Essential steps in the development of EC method include the formulation of the theoretical framework (Reynolds, 1895), first studies on momentum transfer with simple analog instruments and strip-chart data logging (Scrase, 1930) and the first fast responding hot-wire anemometry and thermometry (Obukhov, 1951; Swinbank, 1951). First EC studies were conducted over short vegetation at locales with extremely level terrain and focused on the structure of turbulence in the atmospheric boundary layer and the transfer of heat and momentum (Swinbank, 1951; Kaimal and Wyngaard, 1990). First EC measurements of CO_2 exchange occurred in the early 1970s but were badly criticized because of their large errors (~40%) due to the slow time response of the sensors (Garrat, 1975). Consequently the next wave of improvements bestrode the development of sonic anemometers and rapid-responding, open path infrared gas analyzers (Jones et al., 1978; Brach et al., 1981; Ohtaki and Matsui, 1982). Still, due to limitations in sensor performance and data acquisition systems, prior to 1990 EC studies were restricted to short field campaigns. With the improve in metrology, nowadays regional networks of continuous flux measurement sites operate worldwide, many of them affiliated to the FLUXNET program (Baldocchi et al., 2001; Baldocchi, 2003).

The EC method is based on the Navier-Stokes equations consulting Reynolds decomposition (Reynolds, 1895). Hereby a variable is decomposed in a time averaged part in the following denoted with overbars and a second part fluctuating from the time average denoted with primes (Equation 2-3).

$$x = \overline{x} + x'$$
Equation 2-3

employing:
x   scalar atmospheric quantity

Further, Reynolds postulates (Reynolds, 1895) are assumed (Equation 2-4, Equation 2-5).

$$\overline{x'} = 0$$
Equation 2-4

$$\overline{xy} = \overline{x}\,\overline{y} + \overline{x'y'}$$
Equation 2-5

employing:
x, y   scalar atmospheric quantities

Employing Equation 2-5 assuming a mean vertical wind of $\overline{w} = 0$, the fluxes of the scalar atmospheric quantities *u*, *T*, *q* and *c* (Equation 2-6 - Equation 2-9) can be formulated. At this, negative signs for sensible-, latent heat- and CO_2 fluxes as well as for the radiation components indicate fluxes to the surface, whereas positive signs indicate fluxes away from the surface.

$$u_* = \sqrt{-\overline{u'w'}}$$
Equation 2-6

employing:
u_*	friction velocity	[ms^{-1}]
u	horizontal wind in mean wind direction	[ms^{-1}]
w	vertical wind speed	[ms^{-1}]

$$Q_H = \rho c_p \overline{T'w'}$$
Equation 2-7

employing:
c_p	specific heat at constant pressure	[Jkg^{-1}K^{-1}]
Q_H	sensible heat flux	[Wm^{-2}]
T	temperature	[K]
w	vertical wind speed	[ms^{-1}]
ρ	air density	[kgm^{-3}]

$$Q_E = \rho \lambda \overline{q'w'}$$

Equation 2-8

employing:

Q_E	latent heat flux	[Wm^{-2}]
q	specific humidity	[kgkg^{-1}]
w	vertical wind speed	[ms^{-1}]
λ	heat of evaporation	[Jkg^{-1}]
ρ	air density	[kgm^{-3}]

$$Q_C = \overline{c'w'}$$

Equation 2-9

employing:

c	CO_2 concentration	[mmolm^{-3}]
Q_C	CO_2 flux	[mmolm^{-2}s^{-1}]
w	vertical wind speed	[ms^{-1}]

Admittedly, the determination of turbulent fluxes according to Equation 2-6 - Equation 2-9 requires a number of simplifications regarding the Navier-Stokes equations (Stull, 1988). Most important assumptions are the absence of density fluctuations (Equation 2-10), stationarity of all scalar atmospheric quantities *x*, *y* respectively (Equation 2-11), no advection, horizontal homogeneity (Equation 2-17) and validity of mass conservation (Paw et al., 2000; Massman and Lee, 2002; Foken, 2006).

$$\frac{\varphi'}{\varphi} << 1$$

Equation 2-10

$$\frac{\partial x}{\partial t} = 0 \ \text{ and } \ \frac{\partial y}{\partial t} = 0$$

Equation 2-11

$$\frac{\partial x}{\partial \xi} = 0 ; \ \frac{\partial y}{\partial \xi} = 0 ; \ \frac{\partial x}{\partial \psi} = 0 \ \text{ and } \ \frac{\partial y}{\partial \psi} = 0$$

Equation 2-12

employing:

t	time	[s]
x, y	variables	[-]
ρ	air density	[kgm^{-3}]
ξ, ψ	horizontal distances in a orthogonal coordinate system	[m]

2.4 Quality Control and Quality Assessment

For the employment of EC method for real measurements, a set of corrections has to be applied and the compliance with forenamed assumptions can be tested.

2.4.1 Correction of fluxes

Preliminary tests include a check for consistency limits, the raw data is checked for physically not possible values, and a spike test (Vickers and Mahrt, 1997). Values failing those tests were omitted, no gap filling took place.

Further necessary raw data corrections were applied in the following order: (a) Cross correlation to maximize covariances of gas concentration and vertical wind signals to compensate a possible time offset. (b) Correction of spectral loss (Moore, 1986). (c) Conversion of the buoyancy flux into sensible heat flux (Schotanus et al., 1983) and after all the (d) WPL Correction, the correction for density fluctuations (Webb et al., 1980; Fuehrer and Friehe, 2002; Liebethal and Foken, 2003; Liebethal and Foken, 2004).

2.4.2   Rotation

For the calculation of the fluxes with EC the mean vertical wind component must be zero. However in reality, due to a variety of factors, such as sensor induced flow distortion or local topography, the half hour values seldom fulfill this presumption. In order to approach the mean vertical wind field towards this criteria, Planar Fit Rotation procedure (Wilczak et al., 2001) is applied. This procedure often succeeds in realigning the wind field in such a manner, that the mean vertical wind is close to zero, provided that the unrotated mean vertical wind speed is below the threshold of $|0.35 \text{ ms}^{-1}|$ (Foken and Wichura, 1996; Rebmann et al., 2005). Therefore this threshold is used to determine the influence of the local flow field to the measurements.

Since at Namco site a misplacement of the CSAT3 of 13 ° downward has been detected in September 2006, a major challenge of the coordinate rotation is to figure out the initiation and developing of the affectation so as to retrieve the data for analysis. Therefore, as many planar fit periods as necessary to approach a nullification of the mean vertical wind speed were introduced according to the wind direction and unrotated vertical wind speed data.

2.4.3   Stationarity

The quality tests consist of a stationarity test and a test on fulfillment of the integral turbulence characteristics (ITC) for each flux. For the stationarity tests, the 30-minute covariances of two raw data signals were compared with the mean out of six 5-minute covariances from the same interval (Foken and Wichura, 1996). Quality flags for stationarity were then assigned to each half-hourly flux according to the range of deviations found between both values (Table 2-2 a)).

2.4.4   Integral Turbulence Characteristics

ITC are basic similarity characteristics of atmospheric turbulence and indicate whether or not the turbulent flow field is fully developed. The development of turbulence was investigated by comparing the normalized standard deviations of the measured wind components and temperature with theoretical values (Obukhov, 1960; Wyngaard et al., 1971; Foken and Wichura, 1996; Thomas and Foken, 2002; Foken et al., 2004). Since no formulations at all exist for CO_2 and H_2O and the temperature under neutral conditions, the investigations of ITC are restricted to vertical and horizontal wind components and the temperature under stable and unstable

Table 2-1: Overview of test criteria on the different fluxes

parameter	stationarity	$ITC\left(\dfrac{\sigma_{T_s}}{T_*}\right)$	$ITC\left(\dfrac{\sigma_w}{u_*}\right)$	$ITC\left(\dfrac{\sigma_u}{u_*}\right)$
Q_h	$\overline{T'w'}$	x (no neutral)	x	
Q_e	$\overline{a'w'}$		x	
u_*	$\overline{u'w'}$		x	x
Q_c	$\overline{CO_2'w'}$		x	

stratification. Hereunto Table 2-1 gives an overview on the test criteria composition for the different fluxes.

Quality flags for each half-hourly flux were assigned according to the same deviation range between measured and theoretical values as taken for the stationarity test (Table 2-2 a)). The final half-hourly quality flag for a specific flux was assigned by taking into account both quality flags, for stationarity and ITC (Table 2-2 b)). Classes 1 and 2 are suitable for fundamental research, whereas classes 3 and 4 can still be used for continuously running measurement programs to obtain monthly or annual sums of fluxes. Data of quality flag 5 should be excluded for any further analysis.

2.4.5   Footprint modeling

A footprint function relates individual flux and concentration measurements of a quantity to its sources (Schmid, 1994).

2.4.5.1   Footprint models

In this study, a Lagrangian stochastic (LS) forward flux footprint model (Rannik et al., 2000; Rannik et al., 2003b) is used to define the footprints of individual measurements. The model resolves individual paths of $5 \cdot 10^4$ air parcels using a 3D LS trajectory model (Thomson, 1987) to describe the parcel dispersion in the turbulent

Table 2-2: (a) Classification scheme for stationarity and ITC test (Foken et al., 2004); (b) overall flag scheme (Rebmann et al., 2005)

Class	Range
1	0–15 %
2	16–30 %
3	31–50 %
4	51–75 %
5	76–100 %
6	101–250 %
7	251–500 %
8	501–1000 %
9	> 1000 %

steady state (flag)	integral turbulence characteristic (flag)	Final flag
1 – 2	1 – 2	**1**
1 – 2	3 – 4	**2**
3 – 4	3 – 4	**3**
3 – 4	5 – 6	**4**
5 – 9	7 – 9	**5**

flow field. For simulations the air parcels are released from the height equal to z_0 and their dispersal in the surface layer is followed until the upwind distance accounts for at least 90% of the total footprint. Dimensions of an individual footprint depend on measurement height, stability of stratification and aerodynamic roughness of the fetch. Because of relatively long computing times of stochastic footprint models, the source areas are pre-calculated separately for a set of 21 stability classes, 20 roughness lengths and 28 observation heights (Göckede et al., 2006). Besides the forenamed three parameters, wind direction is the only input parameter left for a spatial allocation of the quality flags and the vertical wind field, later referred to as 'quality features'. All meteorological input parameters (stability class and wind direction) are withdrawn after all the previous steps data processing. Further, the roughness length of the surrounding terrain has to be provided as a rectangular matrix with regular grid spacing.

2.4.5.2   Spatial averaging

To determine the so called 'footprint climatology' (Amiro, 1998), i.e. the characteristic source of long term measurements, it is necessary to overlay the footprints of individual measurements. This is done by assigning a contribution factor for each half hour measurement to each cell of the matrix. For each cell the contribution factor is greater than 0%, additionally the flag of the corresponding quality features for each half hour measurement are stored. Due to accumulation of all contribution factors of one specific cell for a certain measurement period, the overall contribution of this cell to the measurement can be determined. By calculating the median of all flags of one quality feature assigned to one cell during this period, the dominating quality of this cell can be calculated. Additionally, the output is accessible for the three stability classes unstable, neutral and stable separately. This option enables for a quality assessment according to stratification. Interpolating the matrices of accumulated contribution factors on an arbitrary level up to 100% originates the so called effect level rings, which are later shown on the maps as white contour lines (e.g. Figure 4-12, Figure 4-14). The extent of the 5% effect level ring is regarded as the maximum extent significantly influencing the measurement quality, later referred to as 'central footprint'. Only quality ratings lying within this extent are taken into account for statements on the actual measurement quality. Quality ratings beyond this limit, later referred to as 'extended footprint', might still reveal disturbances of the local flow field, but have to be evaluated carefully, since the number of measurements for calculating statistics is decreasing with distance.

2.4.5.3   Spatial quality structures

Four different turbulent fluxes are analyzed in the context of this study. Finding any kind of correlation between the qualities of these fluxes at one site is straightforward, as in most cases effects found are rather caused by local terrain characteristics or the

installation than by device failure. For the quality treatment, a general overview on the different types of effects detected shall be given.

Isolated effects on the data quality can be roughly described as a narrow wind direction sector with reduced data quality in an otherwise higher quality region of the map. In most of the cases when this effect occurs, the total number of low-quality measurements is rather low, so that they could easily be overlooked as insignificant in a normal QAQC-analysis. Combined with the footprint model, these low quality data can more easily be identified when they fall together in one wind sector, sometimes just for one class of stability of stratification. Therefore, this is the best example of the usefulness of coupling QAQC-approaches for eddy-covariance with footprint modeling.

Omnidirectional effects show the same characteristics as the isolated effects outlined above in a way, that they can only occur during a specific stability of stratification or for a specific flux. The difference is that they are not restricted to a specific wind sector and therefore indicate a manifold problem with the terrain characteristics or the installation.

2.5 Conversions

Beyond the data processing for the derivation of the fluxes and the QA, certain time series have to be converted for the means of comprehensible presentation. For instance no additional temperature sensor has been laid out. For this reason the only measurement available to derive the air temperature is the sonic anemometer. The so called sonic temperature (Kaimal and Gaynor, 1991) as measured is therefore converted into actual temperature employing water vapor pressure (Equation 2-13).

$$T = \frac{T_s}{1 + 0.32\dfrac{e}{p}}$$
Equation 2-13

employing:

e	water vapor pressure	[hPa]
p	atmospheric pressure	[hPa]
T	temperature	[K]
T_s	sonic temperature	[K]

However, for the calculation of water vapor pressure over absolute humidity, the measure of humidity in the raw data for this study, in turn the temperature is requested (Equation 2-14).

$$e = aR_vT$$
<div align="right">Equation 2-14</div>

employing:

a	absolute humidity	$[\text{kgm}^{-3}]$
e	water vapor pressure	$[\text{hPa}]$
R_v	gas constant for water vapor	$[\text{Jkg}^{-1}\text{K}^{-1}]$
T	temperature	$[\text{K}]$

Since no other temperature reference is available, in step 1, water vapor pressure has been calculated employing sonic temperature. In step 2, actual temperature has been calculated employing the water vapor pressure of step 1. For validation reasons, two more iteration steps have been carried out. For the underlying climate conditions small values of water vapor pressure are to be expected. Thus, up to fourfold supersaturation in the measured values has been neglected, since Equation 2-13 is therefore relatively insensitive.

    Further, saturation water vapor is needed to derive the relative humidity and has therefore been calculated over temperature according to the Magnus formula (Sonntag, 1990) with a case differentiation for surfaces containing solid ($t<0$) and liquid ($t\geq0$) water:

$$E = 6.112 \cdot e^{\frac{c_1 t}{c_2 + t}}$$
<div align="right">Equation 2-15</div>

employing:

c_1	22.46 (t<0) or 17.62 (t>0) respectively	$[-]$
c_2	272.62 (t<0) or 243.12 (t>0) respectively	$[°\text{C}]$
E	Saturation water vapor pressure	$[\text{hPa}]$
t	temperature	$[°\text{C}]$

2.6 Plausibility tests

As to check plausibility ranges for the radiation and pressure measurements and the sensitivity of the results from preceding steps to those, a set of basic equations is needed. Thus for the estimation of the maximum extraterrestrial radiation, the cosine theorem has been consulted (Equation 2-16).

$$S = S_0 \cos\theta$$
<div align="right">Equation 2-16</div>

employing:

S	extraterrestrial radiation	$[\text{Wm}^{-2}]$
S_0	solar constant	$[\text{Wm}^{-2}]$
θ	solar zenith angle	$[°]$

To conclude maximum incoming solar radiation at surface level, atmospheric extinction has to be considered (Equation 2-17).

$$S_s = S \cdot e^{\frac{-\tau}{\cos\theta}}$$ Equation 2-17

employing:

S	extraterrestrial radiation	[Wm^{-2}]
S$_s$	solar radiation at surface level	[Wm^{-2}]
θ	solar zenith angle	[°]
τ	optical depth of atmosphere	[-]

Moreover, longwave radiation has been estimated using the Stefan Boltzmann law (Equation 2-18). Therefore, normally the temperature of the pyrgeometers termistors is used. However, no termistor data was available and the estimates had to be calculated employing air temperature.

$$L = \varepsilon\sigma T^4$$ Equation 2-18

employing:

L	longwave radiation	[Wm^{-2}]
T	temperature	[K]
ε	emissivity	[-]
σ	Stefan-Boltzmann constant	[Wm^{-2}K^{-4}]

Applying the Barometric formula in terms of the polytrope atmosphere (Equation 2-19), the pressure measurement at the station under investigation can be compared to a reference station at different altitude.

$$p = p_R \left(\frac{T}{T_R} \right)^{\frac{g}{R_L\gamma}}$$ Equation 2-19

employing:

g	gravity acceleration	[ms^{-2}]
p	atmospheric pressure	[hPa]
p_R	atmospheric pressure at reference station	[hPa]
R_L	gas constant of dry air	[Jkg^{-1}K^{-1}]
T	temperature	[K]
T_R	temperature at reference station	[K]
γ	vertical temperature gradient	[Km^{-1}]

After all, uncertainties of air density due to errors in pressure and temperature measurements can be assessed with the ideal gas law (Equation 2-20). Since virtual- and sonic temperatures diverge little, sensitivity of air density can be calculated employing sonic temperature (Foken, 2006).

$$\rho = \frac{p}{R_L T_s}$$

Equation 2-20

employing:

p	atmospheric pressure	[hPa]
R_L	gas constant of dry air	[Jkg^{-1}K^{-1}]
T_s	sonic temperature	[K]
ρ	air density	[kgm^{-3}]

3   Materials and Methods

3.1   Areas under investigation

The analysis was carried out for two sites in Tibet, China, namely Namco, lying on the SE banks of Lake Namco, located 150 km N of Lhasa (Figure 1-1: Nam Cuo), and Everest, located in vicinity of the #1 Mount Everest Base camp (Figure 1-1: Mt. Qomolangma). For exact coordinates see Table 3-2.

3.1.1   Exposure and geomorphology

The Namco site (Appendix Picture 1) at 4745 m a.s.l. is located between the Lake Namco in 1 km distance NW, and a NEE-SWW oriented mountain range peaking 5700 m above sea level (a.s.l.) in 15 km distance SSE (Figure 3-1). The measurement itself is located on a level plane, dominating land use class is grass(-). Another small lake is located 150 m NW of the tower stretching NE-SW for 2 km. 80 m W of the measurement the station building, 40 m and 80 m NE a 30 m profile tower and a container for trace gas measurements are established (Figure 4-9).

   The Everest measurement (Appendix Picture 1) at 4475 m a.s.l. is located in an s-shape valley inclining from SW to NE (Figure 3-1, Figure 3-2) with a steep slope ascending no further than 300 m N of the tower (Figure 4-34, Appendix Picture 2). The crests along the valleys slopes display a height of 600-800m a.g.l., comparatively
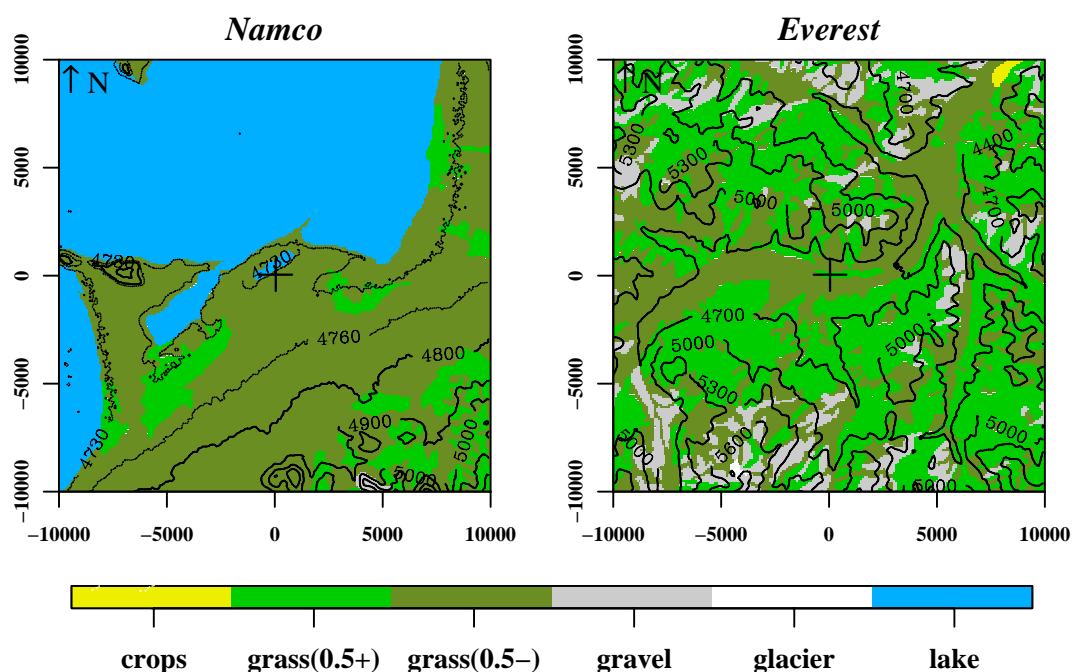

Figure 3-1: Land use map for Namco and Everest site. The position of the flux measurement is indicated with the central cross-hair, black contour lines indicate the elevation a.s.l. [m]. Land use classes are distinguished according to the color bar.
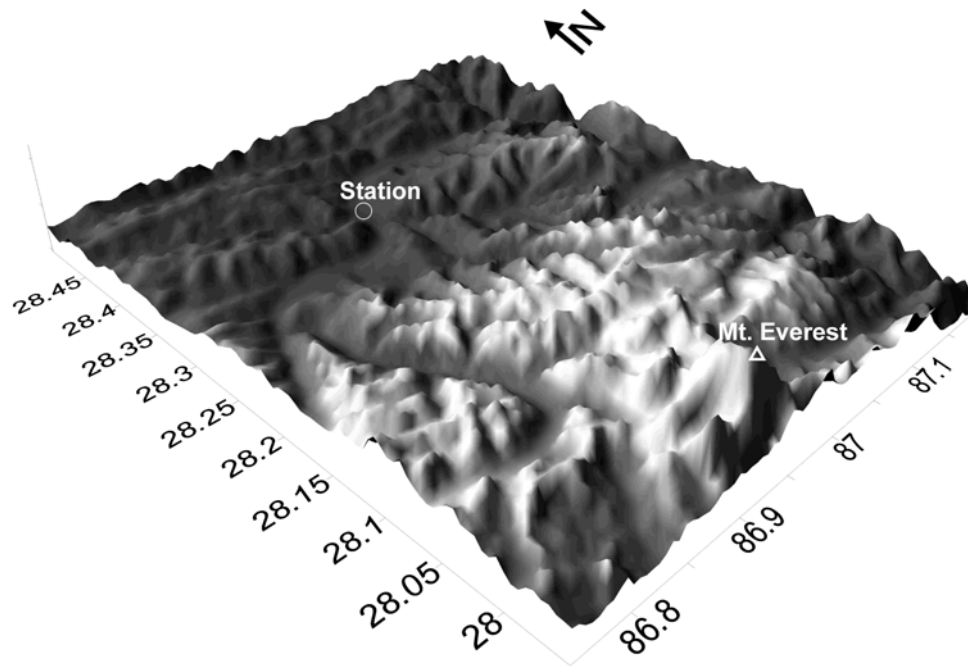
Figure 3-2: Three dimensional topography map of the region near Mt. Everest with the coordinates in degree. Glaciers cover the regions atop 6000m a.s.l, displayed in white X- and Y axis display °

higher in the S of the valley crook, peeking at 7000m a.s.l. and partially covered by glaciers. The dominating land use type is grass(+) and hummock, patches of harvested grain fields are located 70 m N and SE, whereas an unpaved road passes in E-W direction 60 m S of the measurement. Beyond the road, a small village stretching E is attached to the SE grain field (Figure 4-31).

3.1.2   Vegetation

The CAS commenced a vegetation inventory for the MORP stations: The vegetation at Namco site is a rather homogenous Potentilla fructicosa shrub, a typical kind of vegetation extensively distributed in China's alpine areas. Species include Carex atrata, Stipa aliena, Helictotrichon tibeticum, Elymus nutans, Festuna rubra, Kobresia capillifolia, Aster flaccidus, Poa orinosa, Oxytropis ochrocephala, Polygonum viviparum, Leontopodium nanum. Since grazing intensity is rather high, vegetation height does not exceed 4 cm (Table 3-1). Distribution is rather sparse and bare soil spots are frequent, LAI amounts from 0.3 to 0.5, ≈20 % is the fraction of herbs.

The land use at Everest site is rather heterogeneous. Areas referred to as grass(-) and grass(+) (Figure 4-31) resemble a Potentilla fructicusa shrub likewise Namco site, but denser (LAI 1-2) with only 10 % fraction of herbs. However, on the hummocks of the swamp area rather a Kobresia meadow is established. The meadow mainly consists of Kobresia pygmaea, K. humilis and Carex atrata sedge associated with Polygonum sphaerostachyum, Thalictrum alpinum, Anaphalis xylorrhiza, Leontopodium pusillum,

Meconopsis horridula, Potentilla spp., Pedicularis spp., and Gentiana spp. On the farming area, a Tibetan type of barley, Hordeum namto, is cultivated.

3.1.3   Weather and climate

The climate on the TP is based on subtropical-autochthonal boundary conditions. Westerlies control the general circulation, whereat monsoon modifies the circulation during summertime. Despite the gorges of Yangtze, Saluen and Mekong, air masses have to traverse the at least 4500 m a.s.l. high mountain ranges surrounding the plateau, wherefore in general only few precipitable water is available on the TP. Precipitation mainly originates from convective processes, e.g. Cumulus congestus and Cumulonimbus clouds. Major source for water vapor is the SE Asian monsoon current, wherefore precipitation gradually decreases from annual 600 mm - 1000 mm in the SE to 100 mm - 300 mm in the NW of the TP. On this account, the S TP is classified as HCw (Subtropical Summer Rain High Mountain Climate), whereas HBS (Steppe High Mountain Climate) is assigned to the central and N TP (Köppen, 1931; Trewartha and Horn, 1980).

   In winter, extensions of the thermal Asia-/ Mongolia- anticyclone display a pressure of hypothetically 1020 hPa - 1030 hPa over the TP. Outcome is a dry, clear and cold weather situation with temperature minima below -40 °C. In springtime, the TP heats up and resolves the anticyclone, precipitation probability slightly increases (Figure 3-3). During summer, the subtropical jet stream has been wandering from 27 ° N latitude to 40 ° N latitude, trailing the summer anticyclone at around 4500 m a.s.l. over Tibet, subsequently leading to higher atmospheric pressures than in winter time (Figure 3-3). Simultaneously, moist air masses press from the convergence zone of Indian and E Asian monsoon in SE Asia along meridional river gorges onto the TP, substantially increasing precipitation (Figure 3-3). During autumn, again dry, clear and cold weather situation prevails (Weischet and Endlicher, 2000).

   A 30 year time series for Lhasa Observation Station (Lhasa55591) has been supplied by the China Meteorological Administration (CMA). The Lhasa reference measurement (Figure 3-3) displays an annual mean temperature of 8.6 C, 426 mm precipitation and an average atmospheric pressure of 652.5 hPa.

3.1.3.1   Everest site

WP and RASS datasets have been obtained in the same valley as the Everest EC measurement took place. Primarily results (Sun et al., 2007), reflecting the average structure of the PBL in pre-monsoon season, shall be presented briefly to prepare a more comprehensive discussion of EC results: The setup utilized consists of a Vaisala LAP3000 WP/RASS, and a Vaisala MILOS520 Automated Weather Station (AWS) located next to the LAP3000 with the anemometer at 20m height a.g.l. in a PBL tower. In the following, all terms regarding boundary layer structure and dynamics are standardized (Seibert et al., 2000).

Lhasa (3650 m)
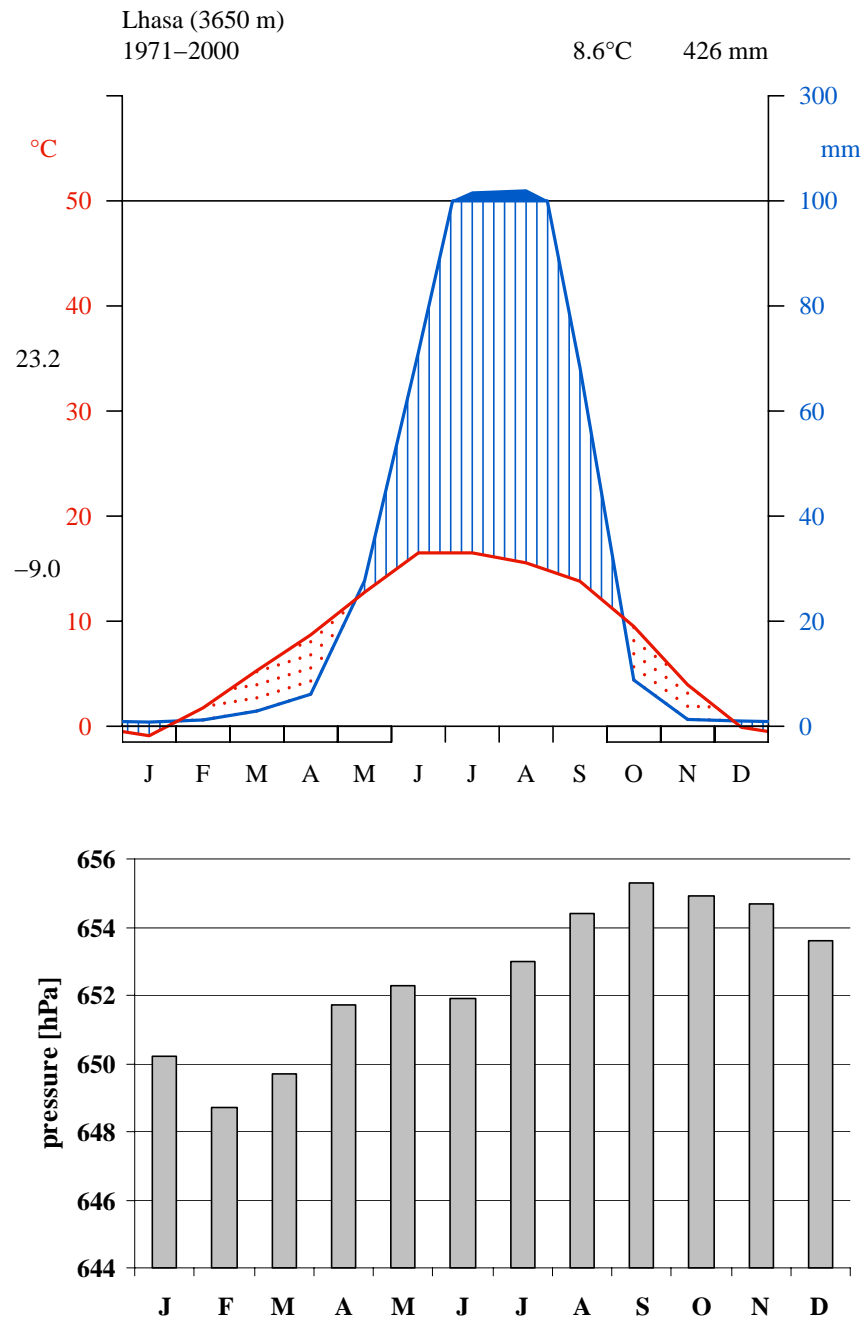1971–2000   8.6°C   426 mm

Figure 3-3: Climate chart (Walter and Lieth, 1960) and corresponding atmospheric pressure for Lhasa Meteorological Observation Station (Lhasa 55591).

The valley under investigation stretches N-S with high mountains in the S, therefore, general surface layer circulation (Figure 3-4) agrees with the slope- and along-valley wind phenomenon (Whiteman, 2000). As for the sudden change of wind direction and increase of wind speed in the afternoon, the glacier wind phenomenon (Gao, 1985), must be taken into account: Southerlies agree with the location of the most prominent glaciers nearby (Figure 3-2). The development and speed of glacier wind depends on the temperature difference between the ice surface and the air nearby. The maximum difference is to be expected around 14:00 (local time), 16:00 Beijing Standard Time
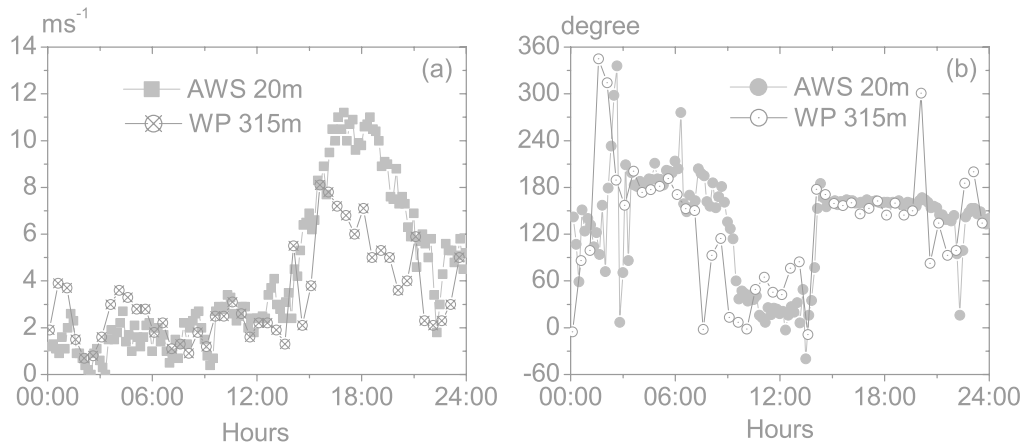
Figure 3-4 Variations of wind speed and direction near ground level, 19 June 2006 (BST). (a) wind speed (b) wind direction. Grey symbols represent the AWS result with anemometer at 20m high; black symbols represent the result of LAP3000 at a height of 315m.

(BST) respectively, when the air temperature reaches its maximum. Considering the stretch of way from the glacier slope to the station, speckled with sizable roughness elements, it's reasonable to detect a maximum of wind speed at the station approximately one hour later(Figure 3-4, 17:00 (BST)). According to glacier wind theory, the peak value of the wind speed profile is to be expected near surface height.

Wind shears have been detected at 500m and 1500m a.g.l. (Figure 3-5 (a)). Since at all times wind directions between surface and middle layer are contorted for at least 90 °, the middle layer apparently displays a compensatory flow pattern preserving mass balance for the surface layer circulation. Besides, an altitude of 500m a.g.l. for the first wind shear points to an influence of the crests along the valley. On the other hand, above the second wind shear southwesterlies can be found at most of the times, the direction of the geostrophic wind and therewith pointing at the transition to the free atmosphere.

The turning and powerful increase of surface wind from 15:00 to 21:00 in Figure 3-5 (b) displays the vertical scale of the glacier wind in the valley, that reaches about 700m a.g.l., close to the average height a.g.l. of the crests along the valley.
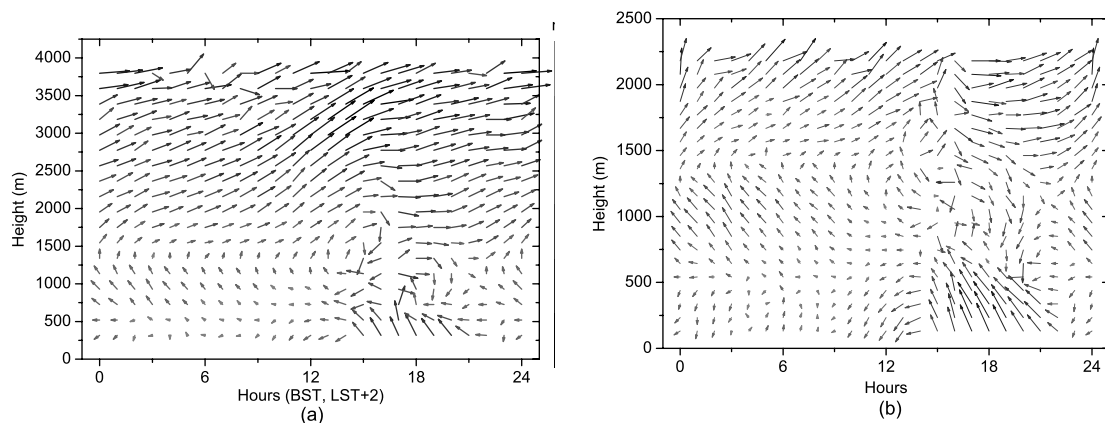

Figure 3-5: Vector maps of average wind speed variation for 29 days, from May 24 to June 21 2006. (a) high mode; (b) low mode. The vector's length represents its relative magnitude.
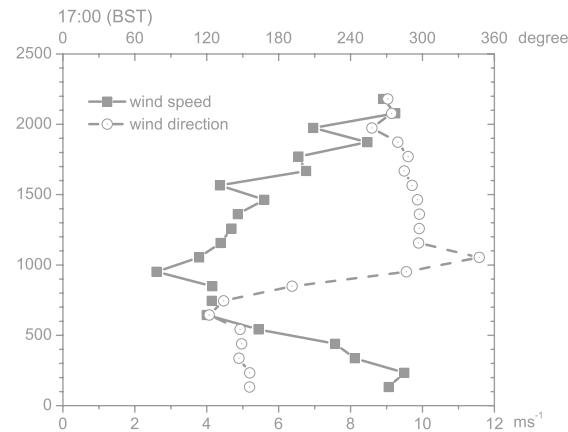
Figure 3-6: average wind profile at 17:00(BST) for 29 days, from May 24 to June 21 2006

Furthermore, the disturbance provoked by the glacier wind can reach up to 2000m a.g.l., since atop the glacier wind, a strong simultaneous inverse flow was found (Figure 3-6). Thus, a possible explanation is that the strong downslope glacier wind causes a lack of air around the glacier. At this point, a compensatory flow is likely to set in from north, since the glacier wind has accumulated air in this direction. This compensatory flow, under the influence of the geostrophic wind, gains northwestern direction.

As for the current context, the key findings of this investigation are:
(a) Two wind shears at 500 and 1500m a.g.l. exist, seemingly providing compensatory flow patterns between surface and middle layer and geostrophic wind in the upper layer.
(b) The phenomenon of glacier wind exists at a distance of 25km from the glaciers, with a vertical impact up to 700m a.g.l.
(c) The glacier wind leads to a compensatory flow with a vertical scale of up to 2000m a.g.l., by far exceeding the valleys crests and even penetrating the free atmosphere, thereby pointing at a supra regional phenomenon.

3.2   Periods under investigation

Measurements for Namco site are available for exactly one year, from 2005-09-12 to 2006-09-12, whereas the Everest measurement lasts from 2005-06-17 to 2006-04-28, 8 ½ month. Thereafter the Everest measurement was moved to the main station few kilometers down the valley because of damages due to cattle.

As to satisfy the assumption of a nullified mean vertical wind speed, the Planar Fit Rotation has been carried out individually for periods with characteristic fetch conditions or equipment misalignment (Table 3-1, Table 3-3). These periods are named R, followed by an index. To further meet the succession phases of the vegetation as well as snow cover periods, which substantially alter the terrain roughness in the course of the year, footprint periods named F, followed by an index,

Table 3-1: Namco site: Periods of varying Planar Fit Rotations in the upper and corresponding footprint parameterizations in the lower half of the table. Rotation / Footprint periods are labeled with index 'R' / 'F' respectively, followed by a number for each period. Footprint periods F_{w1} and F_{w2} account for scenarios over the whole measurement, parameterized by the fetch conditions of periods where denominated.

Rotation period		R_1		R_2	R_3	R_4
from		2005-09-12		2005-11-10	2006-04-14	2006-08-14
to		2005-11-09		2006-04-13	2006-08-13	2006-09-12
coeffecients	α	0.028		0.025	0.042	0.041
	β	-0.002		-0.018	-0.031	-0.140
	γ	-0.036		-0.048	-0.049	-0.060

Footprint period		F_1 / F_{w1}	F_2 / F_{w2}	F_3	F_4 / F_{w2}	F_5 / F_{w1}
from		2005-09-12	2005-10-01	2005-11-01	2006-03-01	2006-05-01
to		2005-09-30	2005-10-31	2006-02-28	2006-04-30	2006-09-12
z_p [m]		0.040	-	-	-	0.040
z_s [m]		-	0.200	0.500	0.200	-
z_a [m]		2.973	2.800	2.500	2.800	2.973
z_0 [m]	lake	0.002	0.002	0.002	0.002	0.002
	grass(-)	0.010	0.002	0.002	0.002	0.010
	grass(+)	0.020	0.002	0.002	0.002	0.020
	slope, edge	0.100	0.080	0.060	0.080	0.100
	settlement	0.500	0.400	0.300	0.400	0.500

3.3 Experimental setup

Both sites are equipped similarly, with a CSAT3 sonic anemometer for three wind-speed components and air temperature measurement and a LI-COR 7500 gas analyzer for H_2O and CO_2 concentrations. The measurement height is 3 m a.g.l., both devices work with a sampling frequency of 10 Hz. For the exact alignment of the turbulent measurement see Table 3-2.

The pyrgeometers in use for the longwave radiation measurement are Kipp&Zonen CG3, the pyranometers for the short wave radiation measurement are Kipp&Zonen CM3, measuring at 1.2 m a.g.l. respectively. Further, data of Vaisala PTB220A pressure sensors mounted at similar height and Hukseflux HFP01 heat flux plates at

Table 3-2: Alignment of the turbulent measurement, coordinates for ellipsoid WGS84

Topic	Feature	Namco site	Everest site
Measurement	Latitude [°]	30.77281	28.31027
	Longitude [°]	90.96302	86.89597
	Elevation a.s.l. [m]	4745	4475
Instrument alignment	Angle (CSAT3 / north)	135	180
	Angle (LICOR / north)	165	192
	Horizontal disparity (CSAT3 - LICOR) [m]	0.35	0.15

Table 3-3: Everest site: Periods of varying Planar Fit Rotations in the upper and corresponding footprint parameterizations in the lower half of the table. Rotation / Footprint periods are labeled with index 'R' / 'F' respectively, followed by a number for each period. Footprint periods F_{w1} and F_{w2} account for scenarios over the <u>w</u>hole measurement, either parameterized by the fetch conditions of the period where denominated (F_{w2}), or reflecting other mean fetch conditions (F_{w1}).

Rotation period		R_1
from		2005-06-17
to		2006-04-28
coeffecients	α	0.033
	β	-0.155
	γ	-0.027

Footprint period		F_1 / F_{w2}	F_2	F_3	F_4	F_{w1}
from		2005-06-17	2005-07-01	2005-08-01	2005-10-01	2005-06-17
to		2005-06-30	2005-07-31	2005-09-30	2006-04-28	2006-04-28
z_{a_N} [m]		3.400	3.400	3.400	3.400	3.400
z_{a_S} [m]		3.000	3.000	3.000	3.000	3.000
z_0 [m]	grass(-)	0.010	0.010	0.010	0.010	0.010
	grass(+)	0.020	0.020	0.020	0.020	0.020
	crops	0.030	0.040	0.050	0.010	0.020
	hummocks	0.060	0.060	0.060	0.060	0.060
	slope, edge	0.100	0.100	0.100	0.100	0.100
	settlement	0.500	0.500	0.500	0.500	0.500

10 cm belowground have been utilized in this study. All data was logged with Campbell CR5000 data loggers at both sites. For this study, raw data from the loggers has only been received for the turbulent fluxes, other data sets such as the radiation components and soil heat flux had already been derived.

3.4   Data flow

Figure 3-7 displays the data flow for this study. In the following, the processing steps as indicated will be explained as well the derivation of terrain information and the construction of the main four types of figures created to visualize the results.

3.4.1   Calculation and display of turbulent fluxes and quality flags

In the first step (Figure 3-7: Conversion), the meteorological dataset was converted from the Campbell binary format 'TOB' into ASCII files and subsequently into the internal binary format of TK2, a Software Package developed by the department of Micrometeorology, University of Bayreuth (Mauder and Foken, 2004). In the second step, all three parts of QA, preliminary tests, raw data corrections and test on fulfillment of EC assumptions as introduced in chapter 2.4 plus the calculation of the fluxes after correction were carried out using TK2. For Everest site this step worked out unobstructed, but for Namco site first a planar fit coefficient for the 2005 data
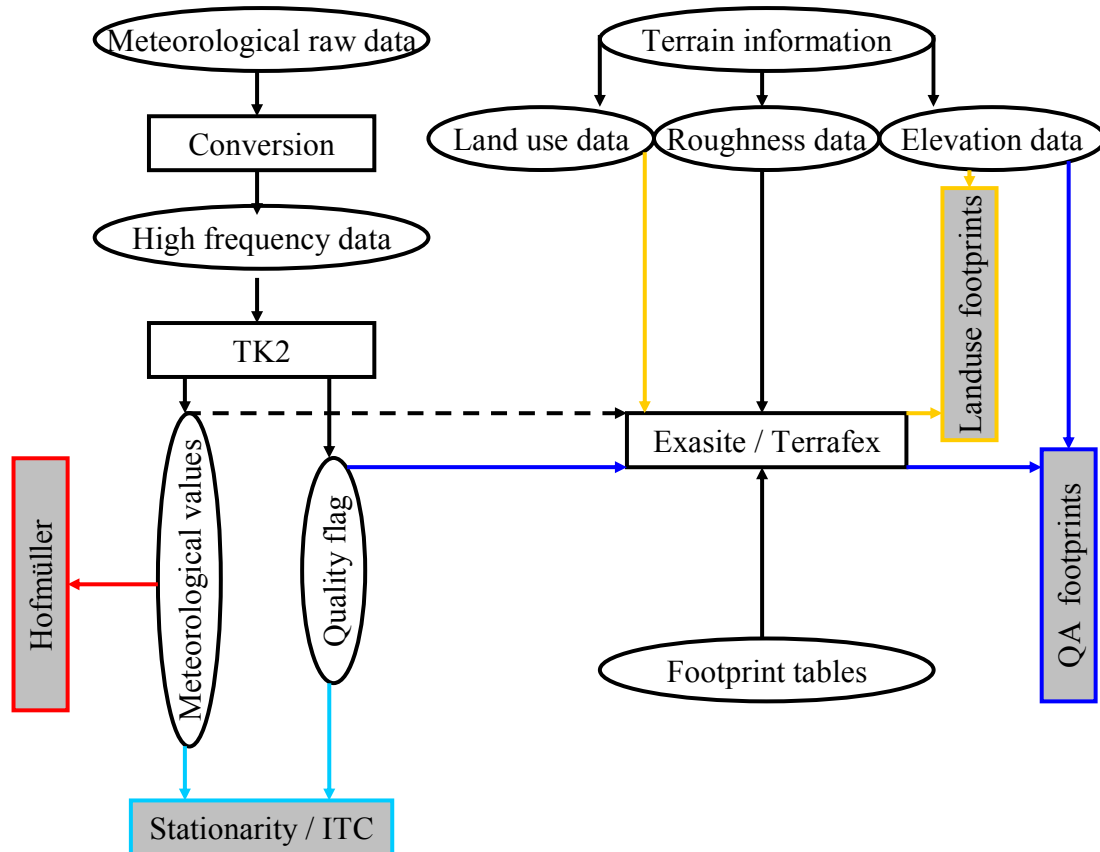
Figure 3-7: Flow chart for the data processing. Ellipses display the data at different stages of the processing, black frames indicate a data processing step, whereas color frames display the types of figures derived. Black arrows indicate the flow of the driving parameters, whereas color arrows highlight the flow of parameters processed and visualized.

with seemingly no misplacement of the sonic had to be determined. For this reason, subsequent datasets have been calculated on basis of the same planar fit coefficient, so as to detect the initiation moment and development of the displacement. Ultimately, four Planar Fit Rotation periods had to be introduced until the vertical wind field could be nullified satisfactorily. As for the estimation of yearly sums of NEE, no gap filling has been applied, but rather have the present measurements been extrapolated to one year.

The results of these steps are visualized in the Hofmüller- and Stationarity- / ITC plots (Figure 3-7). In the Hofmüller plots (e.g. Figure 4-1), the meteorological parameters of this study are displayed in a diurnal vs. annual resolution. The Stationarity / ITC plots have been created on basis of these two quality criteria: For each flux a combination of stationarity- and ITC flag time series is classified for 30 ° wind sectors. In a subsequent step, stationarity flags are classified according to ITC flag and the median stationarity flag of each wind sector / ITC flag class is calculated. Now the median of stationarity is displayed against ITC for each wind sector class with contour lines overlaid, which display the number of stationarity flags in each wind sector / ITC flag class relative to the whole sample size (e.g. Figure 4-15). These

figures are best to use after a sector of comprised quality has been identified. In that case one can look up the relevant sector and conclude, whether the dominating failure is due to instationarity or undeveloped turbulence and whether or not the measurement is regularly affected by this feature.

3.4.2   Derivation of land use - and roughness length information

Land use data of the Chinese Academy of Sciences (CAS) with a resolution of 50 m was used.

3.4.2.1   Digital land use data

Land use classes had been distinguished due to unsupervised classification of Landsat TM/ETM images, verified during on-the-spot investigations in 2000. For refinement and evaluation, the direct surrounding of the flux tower was remapped in 2006 with a resolution of 20 m due to on-the-spot investigations, covering areas of 1.6 km^2 (Namco) and 0.3 km^2 (Everest) respectively. Spatial Reference was obtained using the Garmin eMap GPS. Measurements were carried out receiving 5-9 satellites causing a spatial precision of 5-7 m. In total, 7 land use classes were distinguished, whereas thereof the target land use type grassland was divided in two classes with vegetation covering degrees exceeding or undercutting 50%, later referred to as 'grass(+)' and 'grass(-)' (e.g. Figure 3-1). Covering degrees less than 5% are included in class 'Gravel'. Further grassland class 'hummock' has been distinguished from type 'grass(+)' for Everest site, since the roughness of this area is notably increased due to sandy tumuli. Elevation data with a resolution of 90 m from Shuttle Radar Topography Measurement (SRTM) provided by the Global Land Cover Facility (GLCF) has been utilized.

3.4.2.2   Roughness length matrix

To obtain the roughness length matrix for the footprint analysis, discrete roughness length values were assigned to every land use type (Table 3-1, Table 3-3). No fixed scheme (Troen and Petersen, 1989) has been adopted, since they do not consider plant growth in the annual cycle. Because no profile measurements were yet available, the roughness length for each land use type except for snow was rather parameterized as 10% of the vegetation height (Foken, 2006). Therefore 5 / 4 periods at Namco / Everest site, respectively have been introduced so as to account for temporal roughness length changes of the substratum. Additionally the class 'slope, edge' has been introduced (e.g. Figure 4-9) in order to account for additional generation of turbulence due to roughness steps, e.g. surrounding the lake in the N at Namco site or directly N of the tower at Everest site. Hereby, a roughness length matrix of 20 m spatial resolution covering 16 km^2 has been derived for each Footprint period.

3.4.3   Footprint modeling and display

In the second loop of data processing, the spatial context of the land use types, quality flags and the unrotated and rotated vertical wind field is determined applying a footprint model to the quality results above. For the initiation of the model by aerodynamic measurement height, displacement height was deducted, wherefore vegetation was multiplied with $^2/_3$, whereas snow height was adapted (Table 3-1, Table 3-3). At Everest site, the measurement is directly located an edge, 40 cm elevated against the N half space as compared to the S half space. Therefore, independent runs for each sector has been carried out, after what the results where merged again. The execution of the model via precalculated footprints (Chapter 2.4.5.1) was carried out by Terrafex and Exasite, two Software Packages developed by the department of Micrometeorology, University of Bayreuth (Göckede et al., 2006). Both packages base on the same core algorithm, but Exasite outputs the land use contributions, whereas Terrafex assigns the spatial extend and its contribution of a quality feature to the measurement. The Exasite results are displayed as histograms for each land use type (e.g. Figure 4-10), whereas the Terrafex results are displayed as map with quality ratings, vertical wind field or land use in the background. Contour lines indicate the relative flux contribution and optional contour lines for elevation can be displayed, as to e.g. assess the influence of topography on the vertical wind field (e.g. Figure 4-33).

4 Results and discussion

For the reason of instrumentation, Beijing Standard Time (BST) is used for all depictions in this study. As for interpretation, one must keep in mind, that local time is two hours behind BST. Since both sites boast a broad variety of individual features to be analyzed, results are for the moment presented independently.

4.1 Namco site

4.1.1 Meteorological data

Meteorological data is shown at an annual basis in the form of so called Hofmüller- or fingerprint plots as known for CO_2 flux visualization. A clear diurnal cycle of wind direction can be identified (Figure 4-1), with southeasterlies at nighttime and west-southwesterlies at daytime. This might be ascribed to an interaction of catabatic and land-lake wind effect, whereas the yearly cycle seems to be triggered super-regional. The distribution of wind direction also varies in the course of the year, west-southwesterlies prevailing in the colder season and southeasterlies in the warmer season of the year. Comparing the available periods of September 2005 and 2006, a transition of wind directions from west- southwesterlies to west- northwesterlies and south- southeasterlies to east- southeasterlies can be detected. Looking at R3 in the mid of April 2006, it seems that a bias commenced after the short data gap and increased by-and-by.

Horizontal wind speed values below 5 ms^{-1} dominate, whereat a clear dependence on west- to southwesterlies during wintertime for values exceeding 6.5 ms^{-1}. Westerlies are the prevailing winds in the lower middle latitudes during wintertime. Since the measurement displays a free fetch for this direction, horizontal wind speed values exceeding 6.5 ms^{-1} coincide with westerlies during wintertime.

Calculation of actual temperature over sonic temperature, as illustrated in chapter 2.5, showed a maximum alteration of -5.4 K after step 1 (Equation 2-13, Equation 2-14) and +0.1 K, 1.9 % relative to step 1 respectively, after step 2. The annual mean temperature of -1.4 °C after step 1 undercuts the Lhasa reference measurement (Figure 3-3) by 10.0 K at an altitude difference of 1095 m. This results in a vertical lapse rate of 9.1 Kkm^{-1}, almost meeting the dry adiabatic lapse rate of 9.8 Kkm^{-1} which concords with extremely low humidity. From mid of October to mid of May, temperatures above the freezing point are limited to sparse periods around sun apex. Altogether measured air temperature values show a similar annual cycle like the Lhasa reference station (Figure 3-3).

According to the barometric formula (Equation 2-19), employing the 30 year average values of atmospheric pressure and temperature for Lhasa reference station (Figure 3-3) and the lapse rate as above as calculation basis, an annual mean atmospheric pressure of 569.9 hPa is expected at Namco station. Hereby the measured average of 568.6 hPa agrees well as does the annual cycle of the air pressure
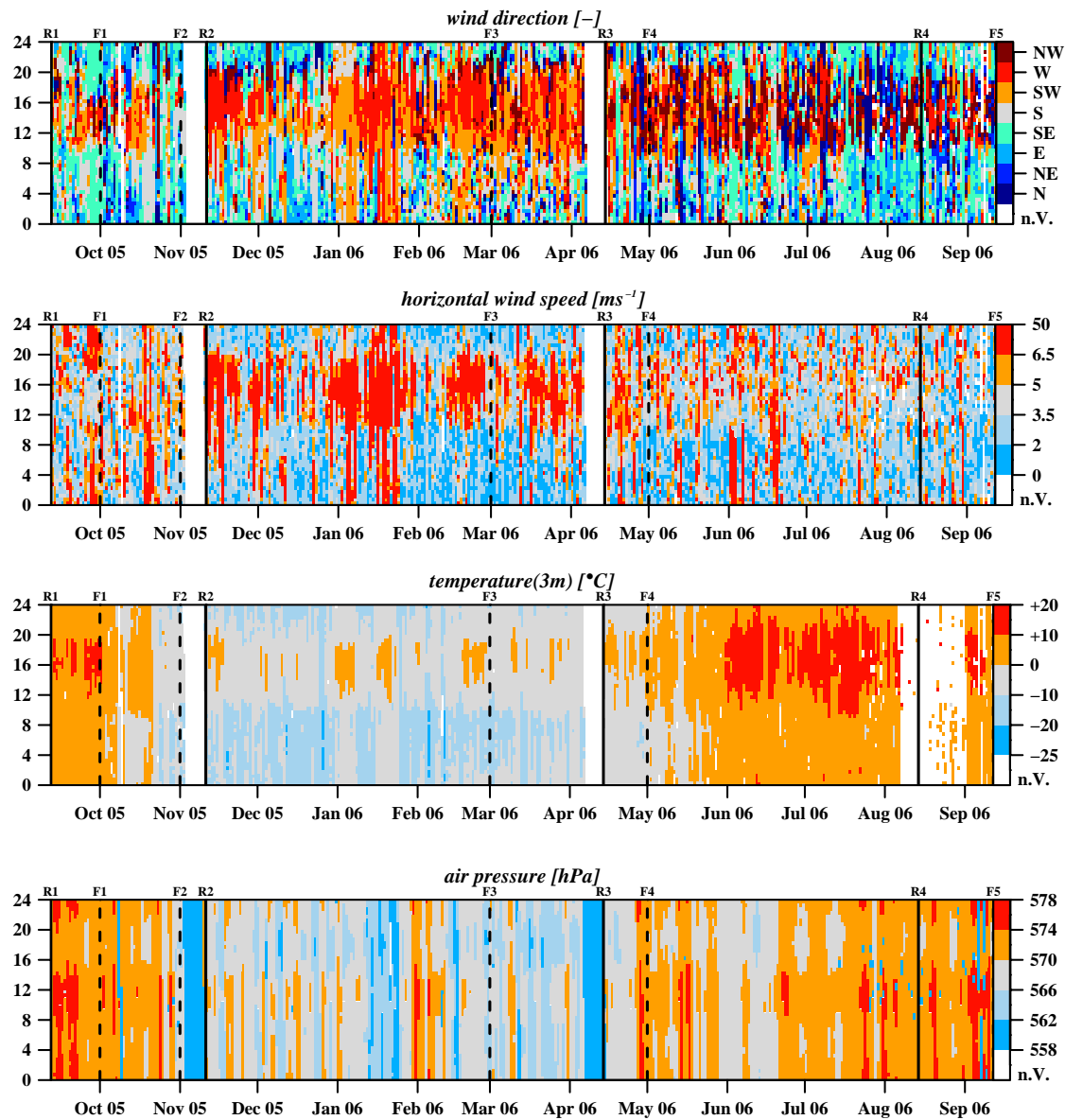
Figure 4-1: Wind direction [-], horizontal wind speed [ms^{-1}], temperature [°C] and air pressure [hPa] for the entire measurement period. X-axis displays the day of the year, Y-axis displays the time of the day, and colors represent quantities according to the color bar attached respectively. Planar Fit Rotation periods are separated by solid lines, the beginning labeled with index 'R', each followed by the number of the period. Footprint periods are separated by dashed lines, the end labeled with index 'F', each followed by the number of the period.

measurement conform to the Lhasa reference station measurement. However, one must be suspicious of the diurnal cycle where lower pressure coincides with higher temperature. Leaps of up to 20 hPa at constant temperature, such as reported in September 2006, are accompanied by an uncertainty of 4.4 % (Equation 2-20) in air density, which directly affects the fluxes of heat (Equation 2-7, Equation 2-8) and indirectly comprises all fluxes due to the WPL correction (Chapter 2.4.1). The Vaisala PTB220A pressure sensor is mounted in a white enclosure directing E and the sensor

possesses a capacitive temperature compensation sensor. Besides, total accuracy after proper calibration within a pressure range from 500 hPa to 1100 hPa and temperature range from -40 °C to 60 °C amounts to ±0.15 hPa according to the manufacturer. Therefore, a bias of the measurement can not be ascribed to heating and cooling effects at the sensor.

The saturation water vapor pressure calculated according to the Magnus formula (Equation 2-15) rarely exceeds the preferably use criteria for infrared hygrometers of 10 hPa (Foken, 2006), and if so only in the warmer period of the year (Figure 4-2).

Calculation of water vapor pressure over absolute humidity and temperature, as illustrated in chapter 2.5, showed a maximum alteration of -0.68 °hPa after step 1 and +0.01 °hPa, 1.9 % relative to step 1 respectively, after step 2.

Relative humidity calculated for water vapor pressure values after step 1 show up to fourfold supersaturation for 70.1 % of all values, especially from mid November to May, where temperatures rarely exceed the freezing point leading to extremely low saturation water vapor pressures. In particular the initiation of high supersaturation in November 2005 starts abrupt, coinciding with a decrease in temperature (Figure 4-1) and humidity measurement. Applying the preferably use criteria for infrared hygrometers to the calculation of relative humidity would decrease supersaturation to a maximum of twofold for 19.8 % of all values, but discards 82.5 % of all values. Then supersaturation exclusively prevails in cases the saturation water vapor pressure barely exceeds 10 hPa. These findings indicate severe problems with the accuracy of the humidity measurement, therefore the measurement itself as well as parameters derived thereof, such as the latent heat flux, must be addressed critically.

Since the test on spike values has been carried out on the raw data of absolute humidity during the data preparation (Chapter 2.4.1), a processing failure can be expelled. Instead, calibration and maintenance reasons must be addressed, that can be divided in two error types, offset and drift: (a) Offset: For measurements of tiny water vapor concentration and relative humidity calculations, as found on the TP, just a small measurement error will create a large percentage error. For measurements below a water vapor pressure of 10 hPa (Foken, 2006), the zero water must be very accurately set to zero due to the insensitivity of infrared hygrometers. (b) Drift: 'Zero drift' can move the water vapor up to ±0.05 mmolmol^{-1}K^{-1} caused by the LI-7500 internal electronics due to contracting/expanding from laboratory (indoor) to outside conditions.

Since the humidity measurement more or less follows the annual cycle of the calculated saturation water vapor pressure (Figure 4-2), ascertained errors seem to be a matter of offset. While turbulent measurements display an offset but not a drift, no influence is to be expected on the flux calculation, in that case the latent heat flux, since average values are subtracted calculating the covariance. Still, the abrupt increase in relative humidity during November 2005 also coincides with an abrupt increase of the measured water vapor pressure, pointing at maintenance problems such as contamination of the sensor windows. Eventually, the latent heat flux
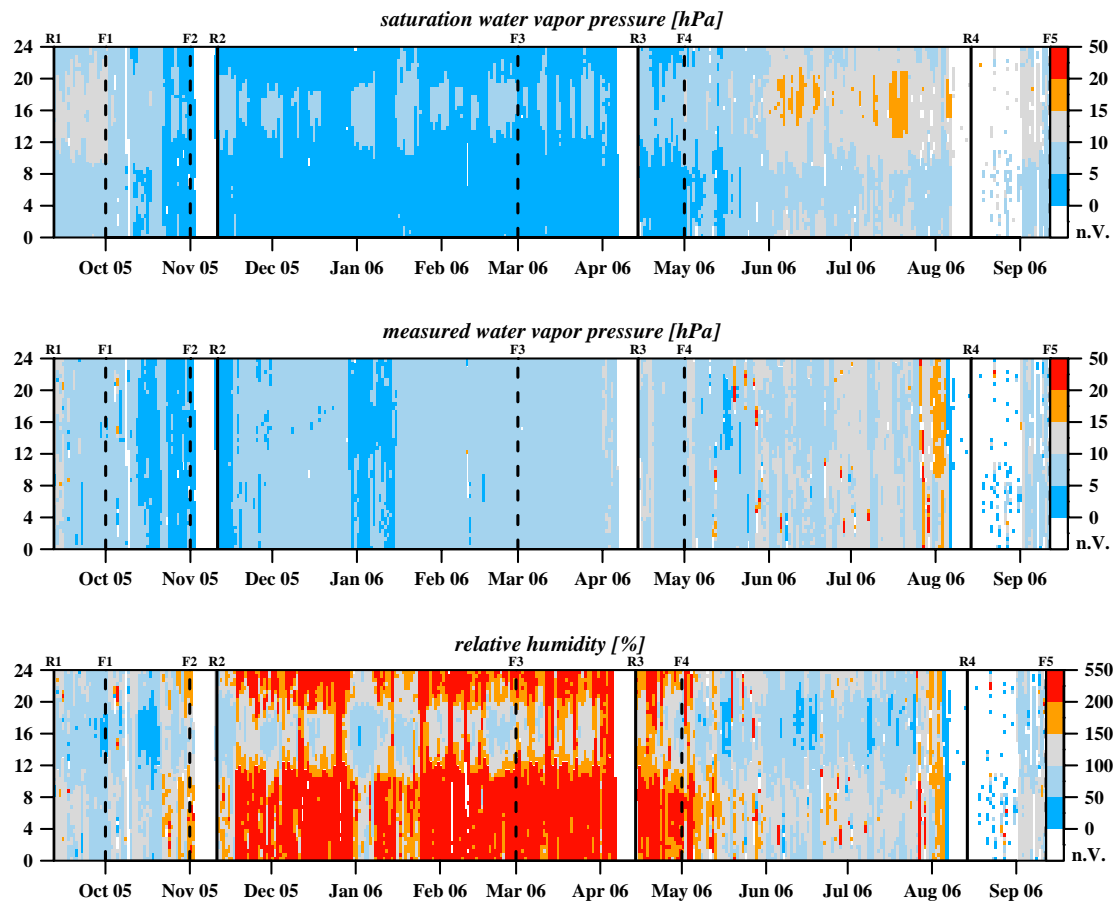
Figure 4-2: Measured water vapor pressure [hPa], saturation water vapor pressure [hPa] and relative humidity [%] for the entire measurement period. X-axis displays the day of the year, Y-axis displays the time of the day, and colors represent quantities according to the color bar attached respectively. Planar Fit Rotation periods are separated by solid lines, the beginning labeled with index 'R', each followed by the number of the period. Footprint periods are separated by dashed lines, the end labeled with index 'F', each followed by the number of the period.

calculated can be utilized in respect of humidity measurement errors, but must still be evaluated carefully all the more regarding stationarity and ITC.

4.1.1.1 Radiative fluxes

According to the dependency of solar radiation on the latitude, (Equation 2-16), values ranging from -801.4 Wm^{-2} to -1358.8 Wm^{-2} between winter- and summer solstice are to be expected at Namco site for extraterrestrial radiation. Assuming an optical depth of 0.1 for clear and 0.8 for overcast conditions, daily maxima of solar radiation at surface level ranging from -204.1 Wm^{-2} to -675.5 Wm^{-2} at winter- and from -606.5 Wm^{-2} to -1227.8 Wm^{-2} at summer solstice are to be expected (Equation 2-17). Supposed that the solar radiation is the only shortwave radiation source and entirely emitted in the spectral range of the CM3 pyranometer in use, which is from 305 nm to 2800 nm, measured incoming shortwave radiation (Figure 4-3) fits well
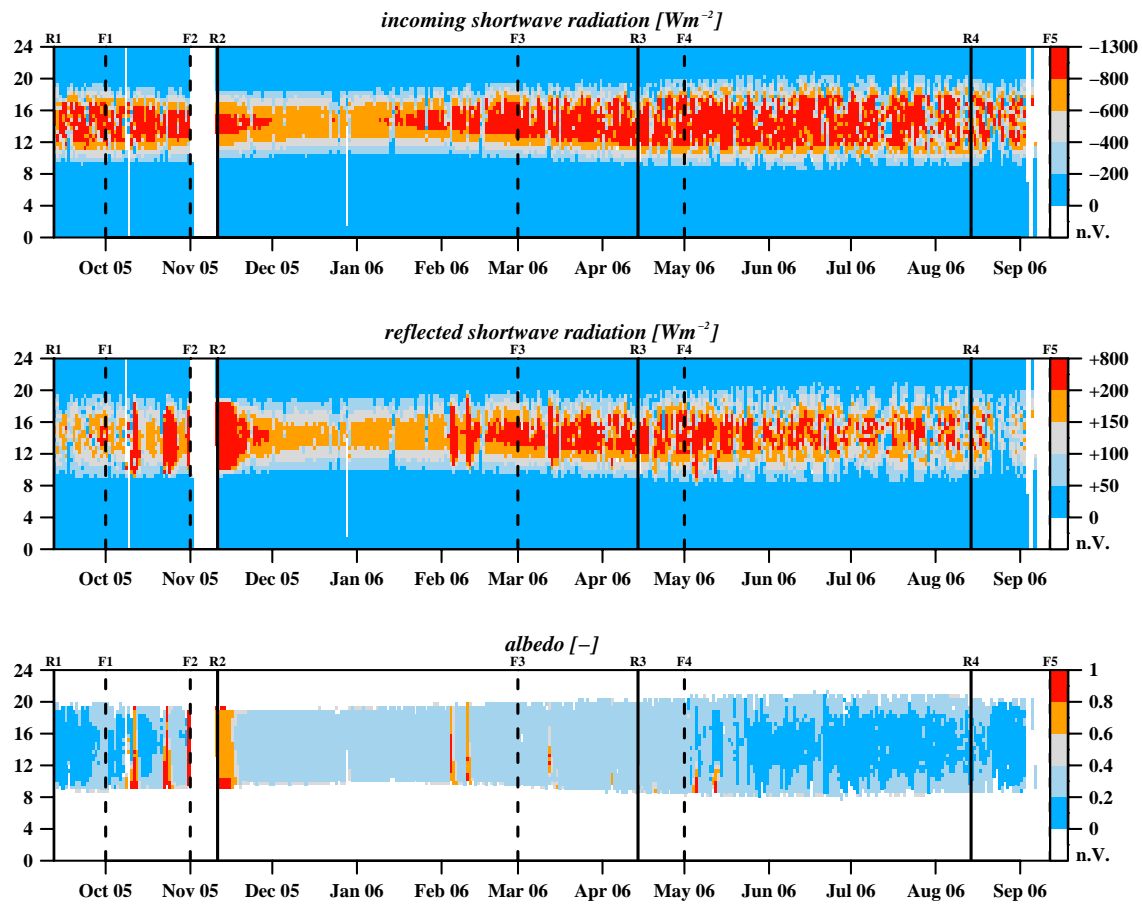
Figure 4-3: Incoming shortwave radiation [Wm^{-2}], reflected shortwave radiation [Wm^{-2}] and Albedo [-] for all cases the incoming shortwave radiation exceeds 50 Wm^{-2}, for the entire measurement period. X-axis displays the day of the year, Y-axis displays the time of the day, and colors represent quantities according to the color bar attached respectively. Planar Fit Rotation periods are separated by solid lines, the beginning labeled with index 'R', each followed by the number of the period. Footprint periods are separated by dashed lines, the end labeled with index 'F', each followed by the number of the period.

within the calculated ranges of daily maxima for most of the days. Only few but pronounced daytime measurements thereunder, especially in July 2006, can be related to dense cloud cover and precipitation during monsoon season.

Albedo has been calculated for all cases the incoming shortwave radiation exceeds 50 Wm^{-2} (Foken, 2006). Consequently, daytime Albedo values ranging from 0 to 1 indicate a proper measurement of the reflected shortwave radiation.

Maxima of Albedo exceeding 0.8 indicate fresh-fallen snow, well lying within the snow periods F2, F3, F4 (Table 3-1). The altering of Albedo due to snow aging and soiling during these periods conforms with tabulated values ranging from 0.25 to 0.75 (Bauer and Raith, 1997), but also agrees with values for dry grey soil (0.25 - 0.30) (Geiger et al., 1995). In the warmer and wetter period, Albedo values agree with those of moist grey soil (0.10 - 0.12) and grass (0.18 – 0.20) (Geiger et al., 1995).
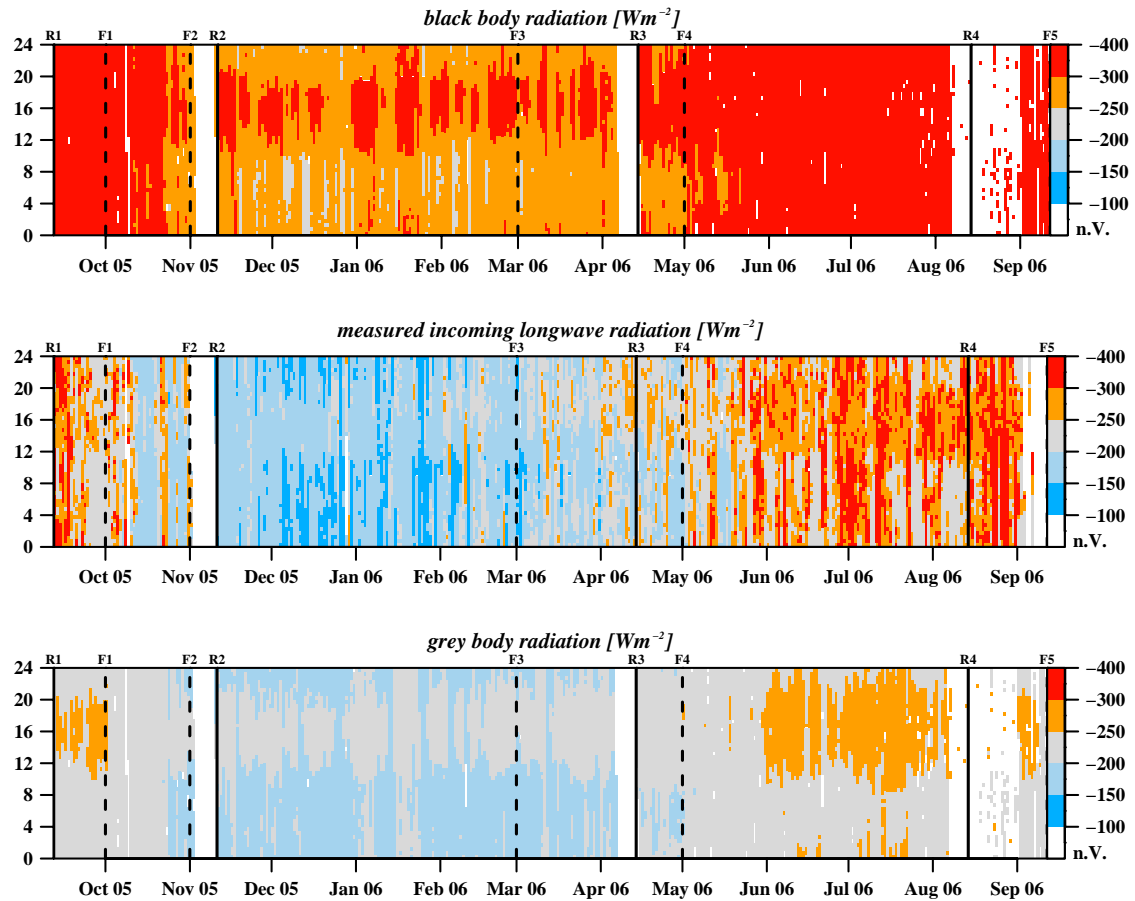
black body radiation [Wm^{-2}]

measured incoming longwave radiation [Wm^{-2}]

grey body radiation [Wm^{-2}]

Figure 4-4: Black body radiation [Wm^{-2}], measured incoming longwave radiation [Wm^{-2}] and grey body radiation [Wm^{-2}] for the entire measurement period. Black- and grey body radiation are calculated after the Stefan-Boltzmann law with emissivities of 1 and 0.7 respectively. X-axis displays the day of the year, Y-axis displays the time of the day, and colors represent quantities according to the color bar attached respectively. Planar Fit Rotation periods are separated by solid lines, the beginning labeled with index 'R', each followed by the number of the period. Footprint periods are separated by dashed lines, the end labeled with index 'F', each followed by the number of the period.

To check plausibility of incoming longwave radiation, measured values are compared to black- and grey body radiation with emissivities of 1 and 0.7 respectively (Equation 2-18, Figure 4-4). At this, measured values do not exceed the black body radiation, whereas a critical period in August 2006 can not be tested because of lacking temperature values. Still, black body radiation before and thereafter agrees with the measurement and the reference climate chart (Figure 3-3) does not show a pronounced decline of temperature for this period. But from October 2005 to May 2006 incoming longwave radiation undercuts grey body radiation. Assumed an air temperature of -20.0°C as calculation basis, grey body radiation implies a temperature of the radiator of -41.6°C. Measured values of incoming longwave radiation as low as 121.2 Wm^{-2} are found in wintertime, indicating a much lower temperature of the radiator of -58.1 °C. This can be regarded as comprehensible, since no clouds are to be expected due to the winter anticyclone above the TP and extremely low humidity.
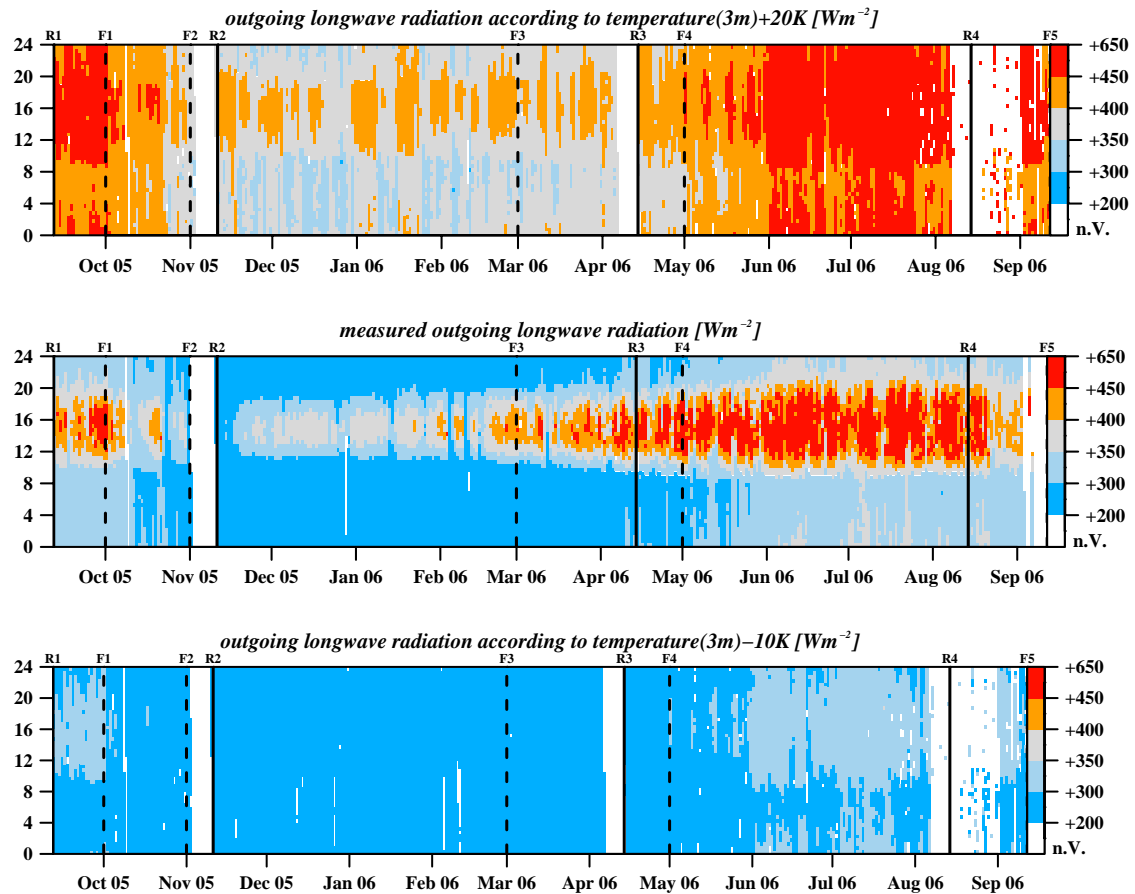
Figure 4-5: Outgoing longwave radiation according to temperature(3m)+20K [Wm^{-2}], measured outgoing longwave radiation [Wm^{-2}] and outgoing longwave radiation according to temperature(3m)-10K [Wm^{-2}]. Parameterizations according to temperature(3m) are calculated after the Stefan-Boltzmann law with temperature deviations as stated. X-axis displays the day of the year, Y-axis displays the time of the day, and colors represent quantities according to the color bar attached respectively. Planar Fit Rotation periods are separated by solid lines, the beginning labeled with index 'R', each followed by the number of the period. Footprint periods are separated by dashed lines, the end labeled with index 'F', each followed by the number of the period.

To check plausibility of outgoing longwave radiation, measured values are compared to the black body radiation according to the measured temperature within certain ranges (Equation 2-18, Figure 4-4). In a mesoscale model approach covering an area near Namco site, 20 % of all cells exceed a surface temperature of 40 °C for 12th of June 1998 (Ma et al., 2002). Since the annual maximum of 3 m temperature at Namco site only amounts to 17.1 °C, the broadening of the deviation for the daytime test from +5 K to +20 K seems obvious. The deviation of the nighttime test has been broadened from -5 K to -10 K due to extremely low humidity, atmosphere constituents and shallow boundary layer. At this, measured values exceed the probability ranges from March to June 2006. This is off-key all the more, since a snow cover has been reported from October 2005 until May 2006. At this point, one should keep in mind that values of air temperature at 3 m were taken for the plausibility parameterizations. During the period under discussion, the temperature of
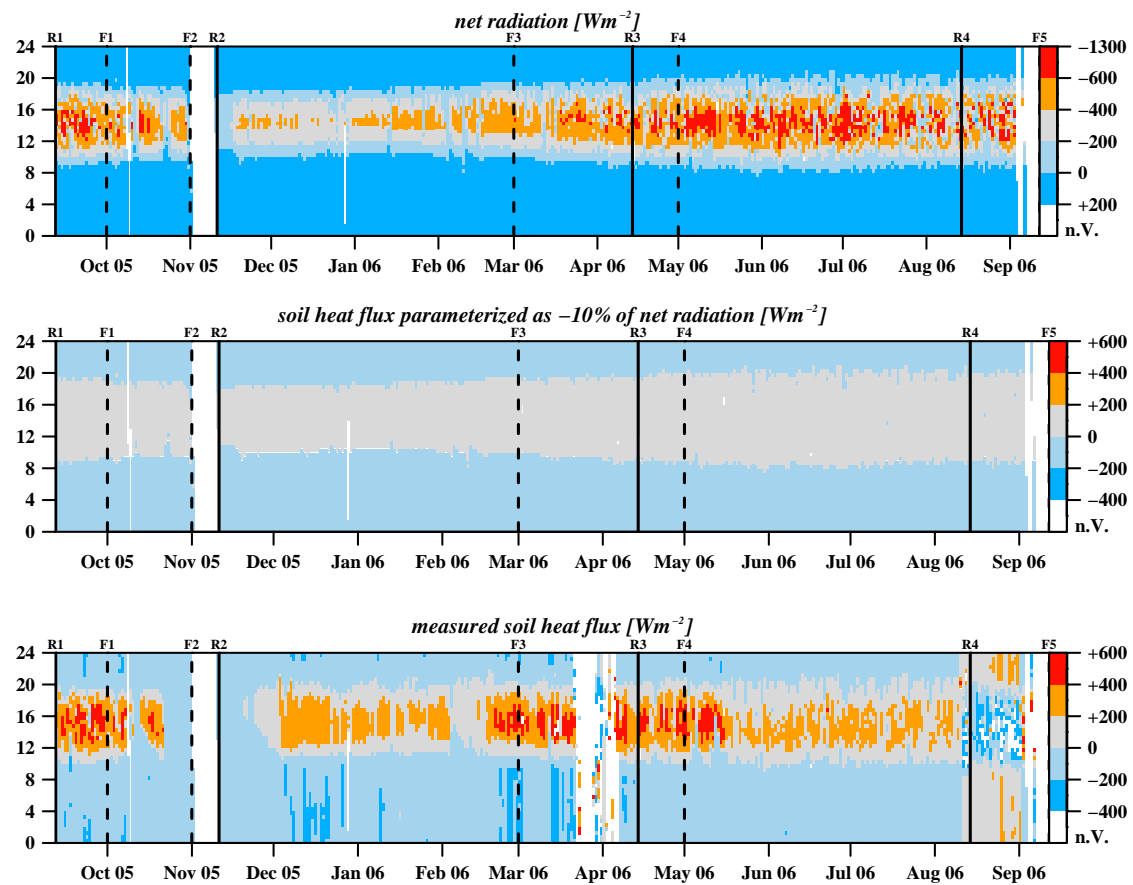
Figure 4-6: Net radiation [Wm^{-2}], soil heat flux parameterized as -10% of net radiation [Wm^{-2}] and measured soil heat flux [Wm^{-2}] for the entire measurement period. X-axis displays the day of the year, Y-axis displays the time of the day, and colors represent quantities according to the color bar attached respectively. Planar Fit Rotation periods are separated by solid lines, the beginning labeled with index 'R', each followed by the number of the period. Footprint periods are separated by dashed lines, the end labeled with index 'F', each followed by the number of the period.

spacious air masses still remains below 10 °C even at sun apex, but the incoming shortwave radiation already exceeds -800 Wm^{-2}. On this account the surface temperature possibly even exceeds the plausibility limit of air temperature at 3 m+20 K, with a sharp gradient near surface. In other respects, the outgoing longwave radiation dataset seems consistent.

   The net radiation (Figure 4-6) agrees quite well with the field observations of GAME Tibet (Ma et al., 2005). Neither in the parameterization approach of the soil heat flux as -10 % of the net radiation (Stull, 1988) nor in the GAME Tibet project, soil heat fluxes exceeding |200| Wm^{-2} are observed on the TP. That in mind, the character of the measured time series can not be physically alleged meteorological reasons and should therefore be discarded. One possible reason is that the heat flux plate is at times not covered by soil and exposed to atmospheric short- and longwave radiation. On the other hand, from August 2006 on, the heat flux plate seems to be installed wrong sided.

4.1.1.2 Turbulent fluxes

The annual cycle of the sensible heat flux (Figure 4-7) corresponds to the net radiation measurement (Figure 4-6) and therewith dominates the surface-atmosphere heat exchange. A relative superelevation against net radiation from December 2005 to May 2006 can be ascribed to the adoption of the latent heat flux for this period. Values ranging from -100 to +200 Wm^{-2}, as found at Namco site, have also been reported during the CAMP Tibet project (Ma et al., 2005) at a research site featuring comparable conditions.

The reliability of the latent heat flux is uncertain, since it can not be assured that humidity fluctuations needed to derive the flux are measured properly. However, despite high fluxes in the mid of November 2005, lowered daytime fluxes from December 2005 to May 2006 coincide with the regional precipitation regime (Figure 3-3), therefore little moisture is available for evapotranspiration. Low latent heat flux during this period is also reproducible because of low temperature and therewith low saturation water vapor pressure (below 5 hPa). This comprehensibility points at an offset but not a drift of the humidity measurement which legitimates the calculation of the latent heat flux.

Consequently, Bowen ratio displays a decrease in mid November 2005, possibly induced by negative sensible- and highly positive latent heat flux due to snow melting processes. From May to December, daytime Bowen ratio reflects environmental conditions dryer than those typical for grassland (Bo≈0.5) and conditions typical for semi-arid regions from December to May (Bo≈5) (Stull, 1988). Negative values point at the oasis effect taking place in the early evening and dew formation in the early morning.

Friction velocity behaves analogous to the horizontal wind speed (Figure 4-1), high values in daytime and shallow breeze at night, with the surface layer kinetic energy reaching its maxima in wintertime. For corresponding discussion see above.

The annual NEE amounts to -150.0 gCm^{-2}, double to triple the amount reported in grassland studies carried out at 3250 m a.s.l. under no grazing conditions on the TP (Xu et al., 2005c; Zhao et al., 2006). Since the Namco measurement is carried out under grazing conditions at much higher altitude with different vegetation characteristic, the studies are not exactly comparable. But it seems consistent, that, assumed comparable precipitation regime, under a shallower boundary layer more photosynthetic active radiation is available. Together with the growing stress due to grazing, this might lead to a higher CO_2 assimilation rate as long as the soil is cold enough so that plant- and microbial respiration of accumulated organic C still undercuts plant CO_2 assimilation. The major C-uptake period stretches from January to October with CO_2 uptake from around 08:00 to 19:00 and CO_2 release from around 20:00 to 08:00. During the cold season, for a short period in the mid of November 2005, CO_2 release persists during daytime, concurring with the fresh-fallen snow event according to surface Albedo (Figure 4-3).
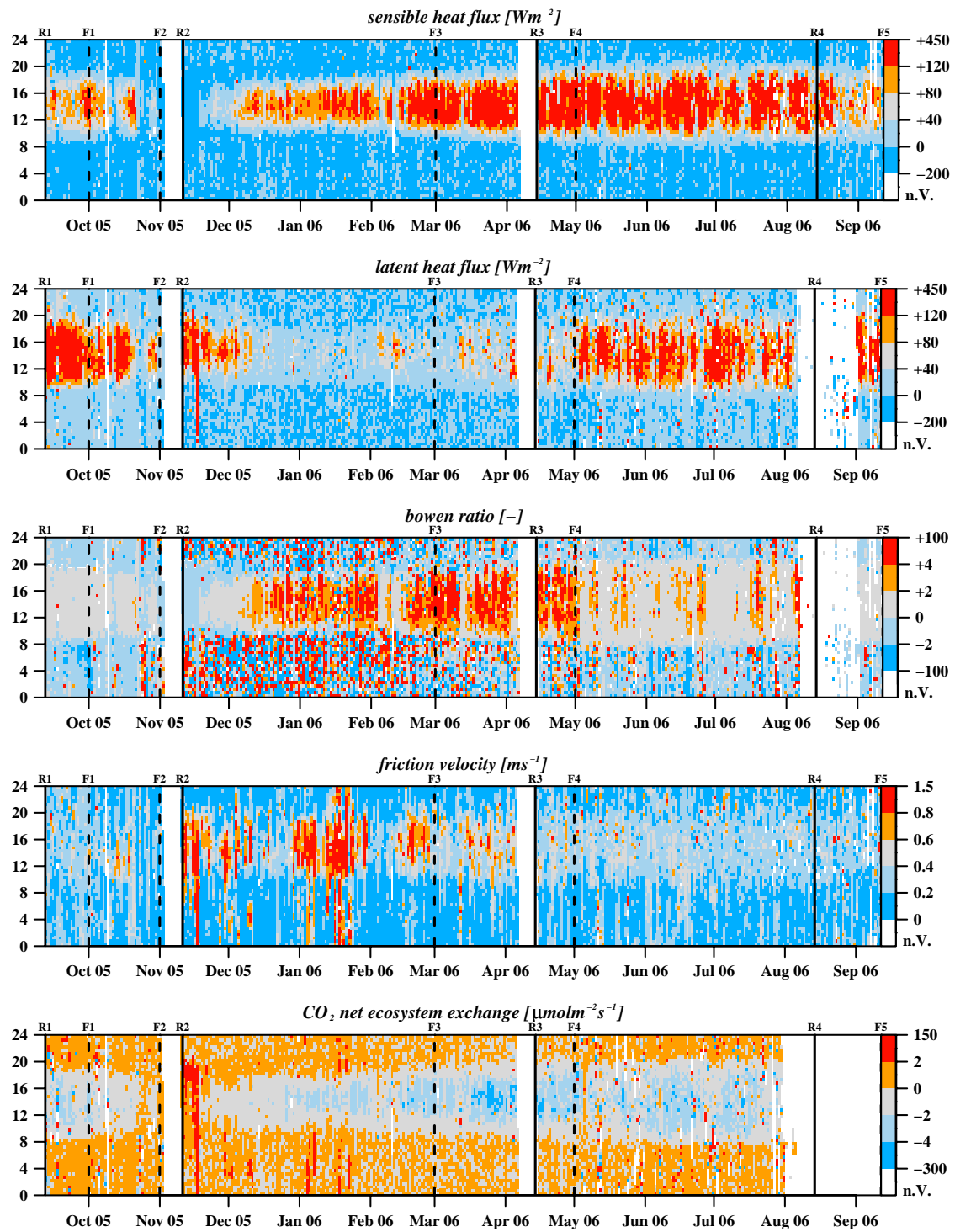
Figure 4-7: Sensible heat flux [Wm^{-2}], latent heat flux [Wm^{-2}], bowen ratio [-], friction velocity [ms^{-1}] and CO_2 NEE [µmolm^{-2}s^{-1}] for the entire measurement period. X-axis displays the day of the year, Y-axis displays the time of the day, and colors represent quantities according to the color bar attached respectively. Planar Fit Rotation periods are separated by solid lines, the beginning labeled with index 'R', each followed by the number of the period. Footprint periods are separated by dashed lines, the end labeled with index 'F', each followed by the number of the period.

4.1.1.3   Energy balance

The characteristic of the residuum time series (Figure 4-8) seems to be triggered by soil heat flux (Figure 4-6) and shows similar fluctuations. Putting values of soil heat flux exceeding |200| Wm^{-2} aside, the energy balance is unclosed for in average more than +150 Wm^{-2} at daytime and less than -50 Wm^{-2} in the evening (late November 2005, early February 2006), amounting to more than 30 % of the net radiation which reflects earlier measurements on the TP (Tanaka et al., 2001; Tanaka et al., 2003).

Stability displays a continuous circle of the year with less unstable cases prevailing at daytime in the cold than in the warm season lead from the decrease of sensible heat flux during that time. Stability relates cubed friction velocity to sensible heat flux. Making use of Figure 4-7, it can be seen that daytime decreases of turbulent energy production by buoyancy (negative stability) are provoked by isochronous maxima in friction velocity and minima of sensible heat flux, e.g. in mid November and mid January. Maxima for unstable cases are registered in footprint period F5, summertime, for neutral cases in F2, autumn, and for stable cases in F3, winter (Table 4-1).

4.1.2   Quality assessment

Footprint periods have been introduced (Table 3-1, Table 3-3) to meet the alteration of terrain roughness with succession phases of the vegetation as well as snow cover periods. Consequently, a temporal assessment for spatial quality structures, as they are revealed by footprint analysis, can be given. Since this procedure yields large
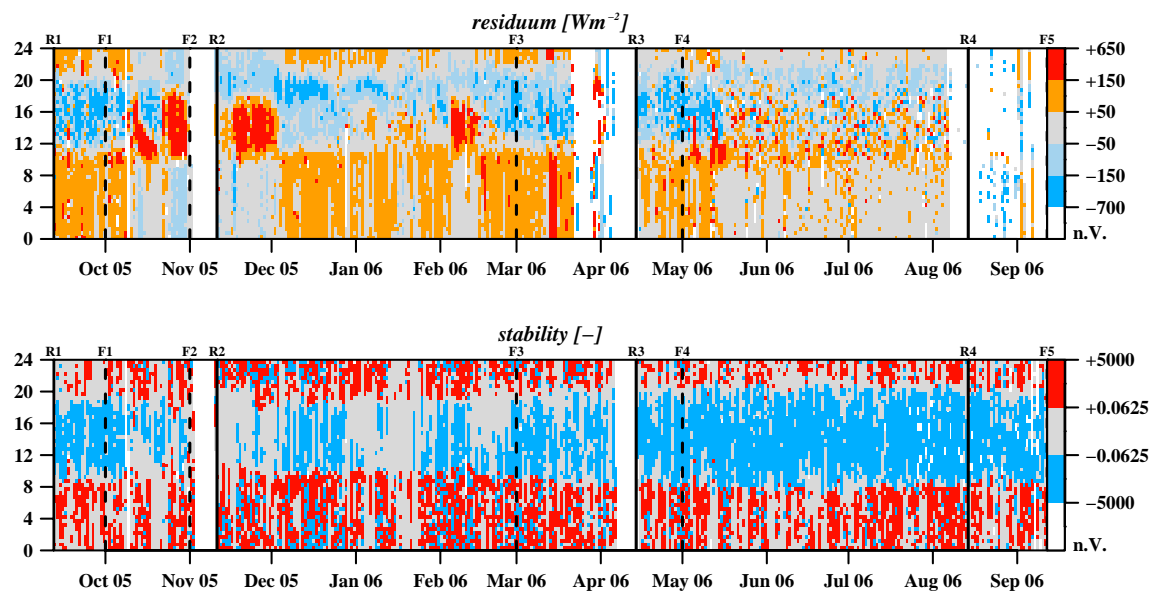

Figure 4-8: Residuum [Wm^{-2}] and stability [-] for the entire measurement period. X-axis displays the day of the year, Y-axis displays the time of the day, and colors represent quantities according to the color bar attached respectively. Planar Fit Rotation periods are separated by solid lines, the beginning labeled with index 'R', each followed by the number of the period. Footprint periods are separated by dashed lines, the end labeled with index 'F', each followed by the number of the period.

Table 4-1: Distribution of stratification throughout the whole observation period (F_w) and within the footprint periods F1 – F5 [%].

Footprint period	F_1	F_2	F_3	F_4	F_5	F_w
unstable	29.6	20.8	23.1	35.7	43.6	33.0
neutral	48.1	51.8	46.3	38.8	34.0	41.1
stable	22.3	27.4	30.5	25.5	22.4	26.0

quantities of graphical information, figures are only presented where denominated and otherwise referred to without depiction. Further, only temporal, spatial and quality patterns containing remarkable contributions are dealt with.
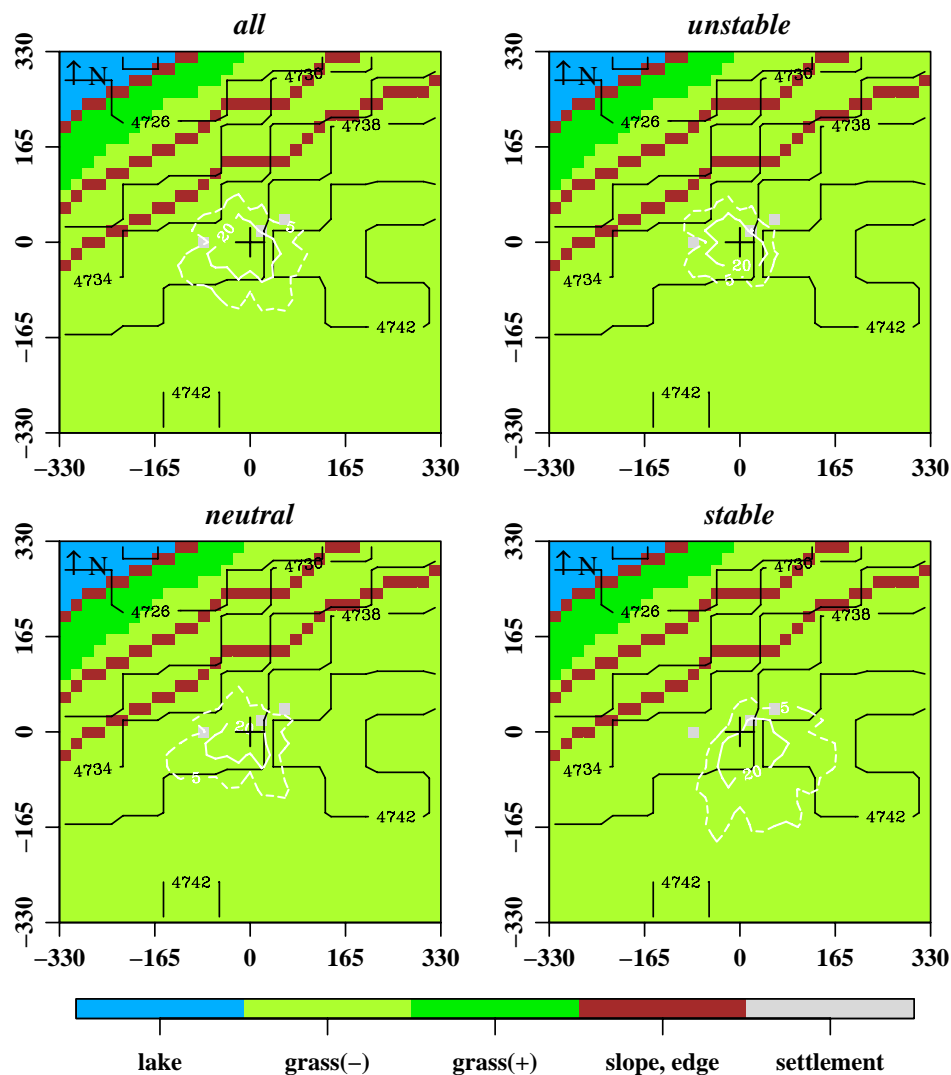

Figure 4-9: Land use contribution according to stratification, scenario F_{w1}, as related to footprint climatology. The position of the flux measurement is indicated by the central cross-hairs. 5 land use classes are distinguished according to the color bar. Black contour lines indicate the elevation a.s.l. [m]; white contour lines display the 5% (dashed) and 20% (solid) effect level rings of the measurements

4.1.2.1   Land use contribution

In accordance with the distribution of the wind direction, the central footprint at Namco site is in average omnidirectional with its centre shifted 20 m from the tower in SW direction. At this, only during unstable stratification, the footprint is truly omnidirectional. However, southwesterlies mainly contribute during neutral stratification and southeasterlies during stable stratification.

Concerning the area covered by measurement, the size of the 5-percent effect level ring during stable stratification was used as an indicator. Multiplying the maximum E-W extension with the maximum N-S extension yields the total area, for Namco site during all stratifications amounting from 3.5 ha for F1 to 16.7 ha for F4 with an average of 6.8 ha for scenario F_{w1}. From Figure 4-9 can be seen, that the central footprint for all stratifications mainly covers the land use of type grass(-). Only three obstacles, the station building in the W, the PBL tower in the nearer NE and the gas measurement container in the farther NE disrupt homogeneity, but the slopes do not directly contribute.

For the assessment of the land use contribution, no distinction of roughness length as provided e.g. by indicating slopes as displayed in Figure 4-9, but rather a distinction of the surface coverage is of interest. Therefore, land use type slope, edge has been restored to the adjacent land use types grass(-) and grass(+). As a result it can be seen from Figure 4-10, land use type grass(-) dominates with an average contribution of 99.1 % to the measurement, followed by the settlement with merely 0.8 %. Maximum average contributions are achieved in F1 for type grass(-) with
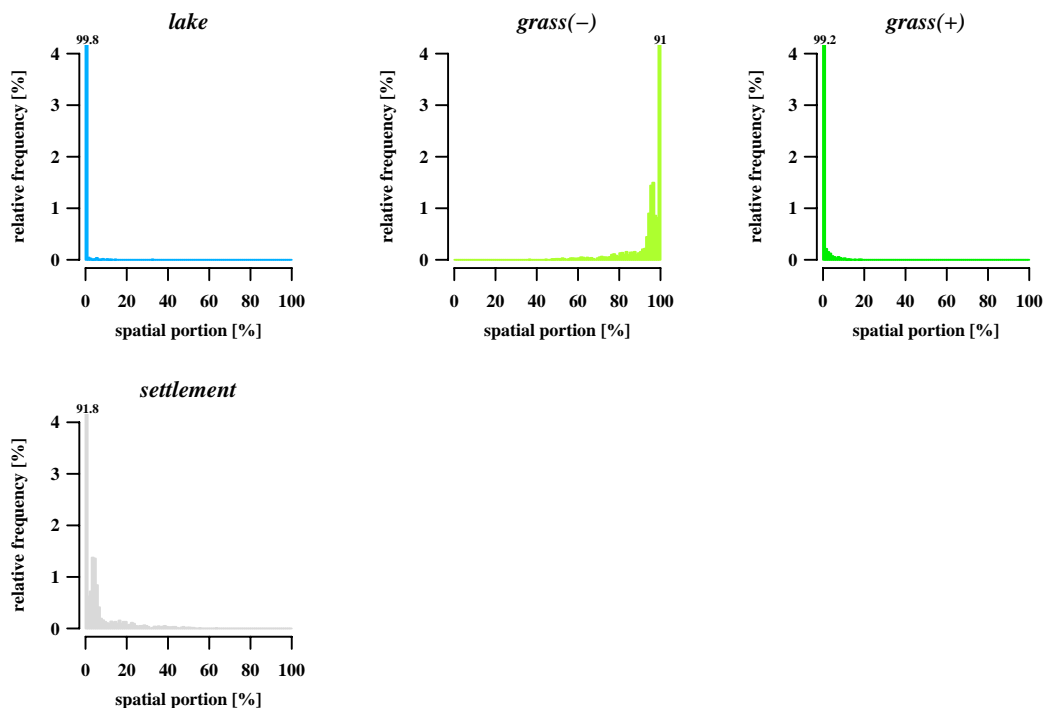

Figure 4-10: Frequency of spatial contribution for land use types as indicated for scenario F_{w1}.

99.6 %, in F2 and F4 for type grass(+) with 0.4 % and type settlement with 1.0 % and in F4 for type lake with 0.2 %.

Finally, as to create the target land cover type grassland, land use types grass(-) and grass(+) have been recombined, so as to be contrasted against the types lake and settlement. At this, introduced a threshold of 95 % of spatial contribution for the target land coverage type attesting homogenous terrain (Göckede et al., 2004), in average 95.8 % of all measurements surpass this threshold with a maximum of 98.4 % in F1 and a minimum of 94.5 % in F4.

4.1.2.2 Vertical wind

The interrelation as found between wind direction and horizontal wind speed (Figure 4-1) can be extended to the unrotated vertical wind speed (Figure 4-11). On this account, a clear dependence of the degree fulfilling the vertical wind nullification on the fetch condition can be stated. Thereby, rotation period R2, with 14.9 %, contained most values exceeding the threshold of $+0.35$ ms^{-1}, whereas R4, with 4.4 %, contained most values undercutting the threshold of -0.35 ms^{-1}. Looking at R3 in mid April 2006,
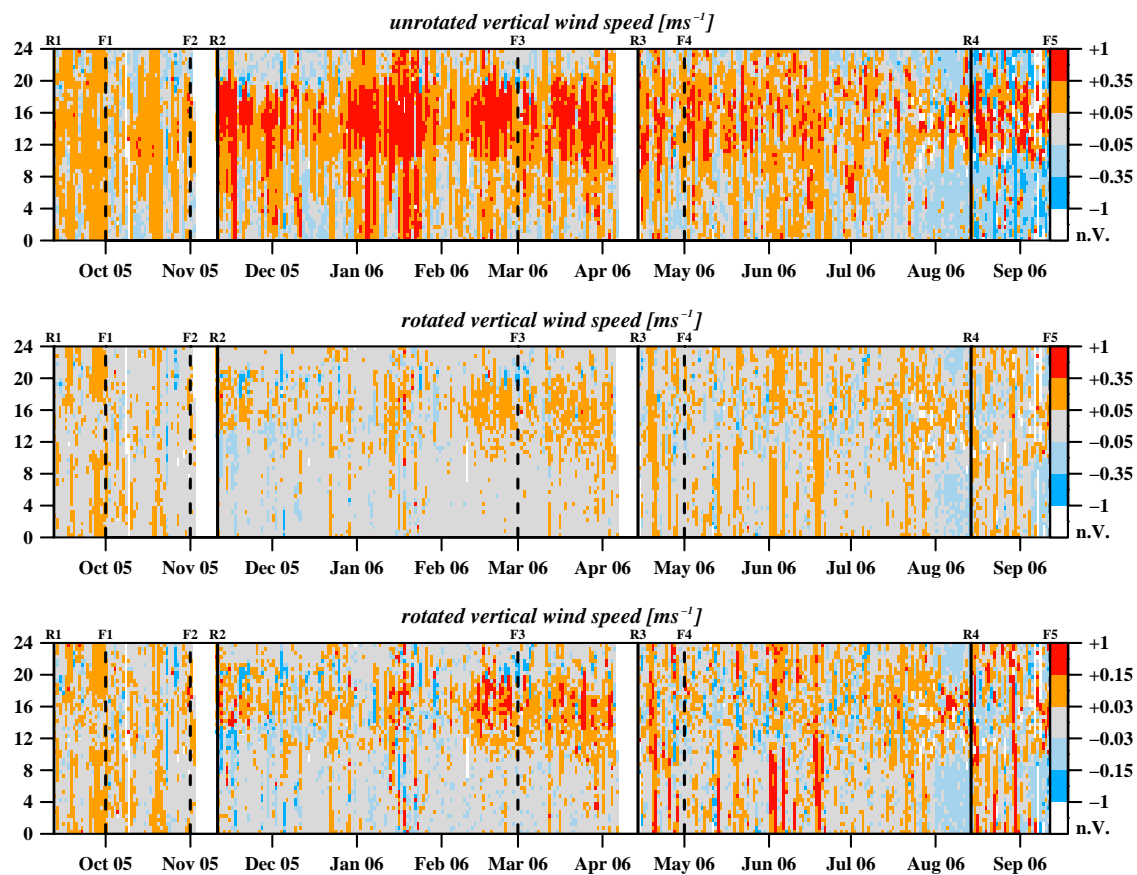

Figure 4-11: Unrotated and rotated vertical wind speed [ms^{-1}] in two classifications. X-axis displays the day of the year, Y-axis displays the time of the day, and colors represent quantities according to the color bar attached. Planar Fit Rotation periods are separated by solid lines, the beginning labeled with index 'R', each followed by the number of the period. Footprint periods are separated by dashed lines, the end labeled with index 'F', each followed by the number of the period.

it seems that, similar to the wind direction (Figure 4-1), a bias commenced after the short data gap and increased by-and-by.

On these accounts, four rotation periods have been introduced (Table 3-1, Figure 4-11). Thereby rotation coefficients α and γ did not alter noticeably throughout the periods observed, indicting constant fetch conditions. In contrast, rotation coefficient β 70 folds during the observation period, with the most remarkable increase from period R3 to period R4, confirming the already afore visually detected bias (Figure 4-1). This bias can be related to a misplacement of the sonic anemometer that, according to the Chinese station operators, presumably initiated during spring storms in 2006, agreeing with the findings of this study.

The Planar Fit Rotation procedure substantially nullified the vertical wind field. For the entire observation period, vertical wind speed values exceeding thresholds of $|0.35 \text{ ms}^{-1}|$ and $|0.15 \text{ ms}^{-1}|$ have been significantly reduced from 15.6 % and 41.1 % before to 0.8 % and 6.7 % respectively after rotation. Values within ranges of $|0.05 \text{ ms}^{-1}|$ and $|0.03 \text{ ms}^{-1}|$ increased from 44.0 % and 28.5 % to 70.2 % and 58.2 % respectively.

Following the temporal assessment, the spatial distribution and degree of elimination of up- / downwind sectors will be addressed. Figure 4-12 displays the results of the footprint analysis. Since footprint period F4 more or less matches footprint period F3, it has been omitted in favor of introducing both approaches representing the entire measurement, F_{w1} and F_{w2}.

As for the extent of the effect level rings and spatial structures, one has to bear in mind, that, according to the footprint approach (Chapter 2.4.5), they are depending on stability, the parameterizations of measurement height and surface roughness. Consequently, even the plots of F_{w1} and F_{w2}, though driven by the same meteorological dataset, appear different because of different roughness length and measurement height parameterizations (Figure 4-12, Figure 4-13): F_{w1} is parameterized by a higher measurement and rougher surface, whereas F_{w2} is parameterized by a lower measurement but throughout smoother surface due to a 20 cm snow cover (Table 3-1). As an effect, the plots of F_{w1} and F_{w2} differentiate by a scaling factor for both, effect level rings and vertical wind feature characteristic, which also must be considered for the interpretation of the remaining footprint period parameterizations. Nevertheless, except for the absolute extend of the footprint, structures of both, effect level rings and vertical wind feature characteristic, remain preserved for either approach, in particular for the central footprint, for homogenous terrain. On this account, parameterization approach F_{w2} will be omitted in following depictions, since parameterization approach F_{w1} covers a greater temporal span of footprint periods and no additional information appears from yet another figure.

As found in a preliminary study (Metzger et al., 2006), which only covered footprint periods F1 and F2, the huge sector of upwind values in the unrotated vertical wind field exceeding the median of $+0.15 \text{ ms}^{-1}$ in the W and SW of the measurement as well as a downwind sector undercutting the threshold in NNW are found throughout
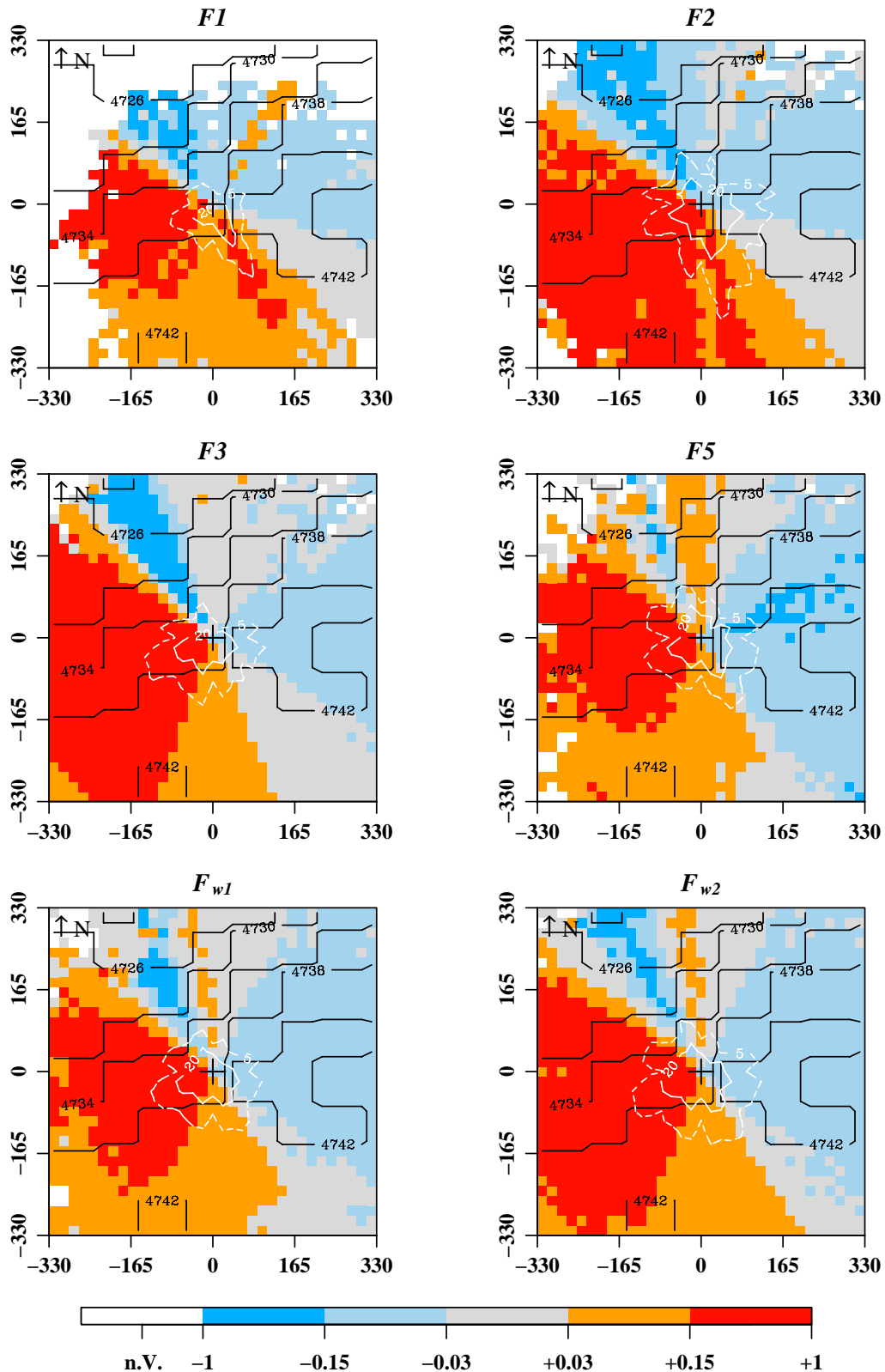
Figure 4-12: Spatial distribution of the median vertical wind speed before Planar Fit Rotation. Values of different footprint periods (labeled with 'F', followed by the period's code) are displayed related to the footprint climatology. The position of the flux measurement is indicated by the central cross-hairs. 5 wind speed classes are distinguished according to the color bar; n.V. indicates that no datasets were available for the matching cell. Black contour lines indicate the elevation a.s.l. [m]; white contour lines display the 5% (dashed) and 20% (solid) effect level rings of the measurements.
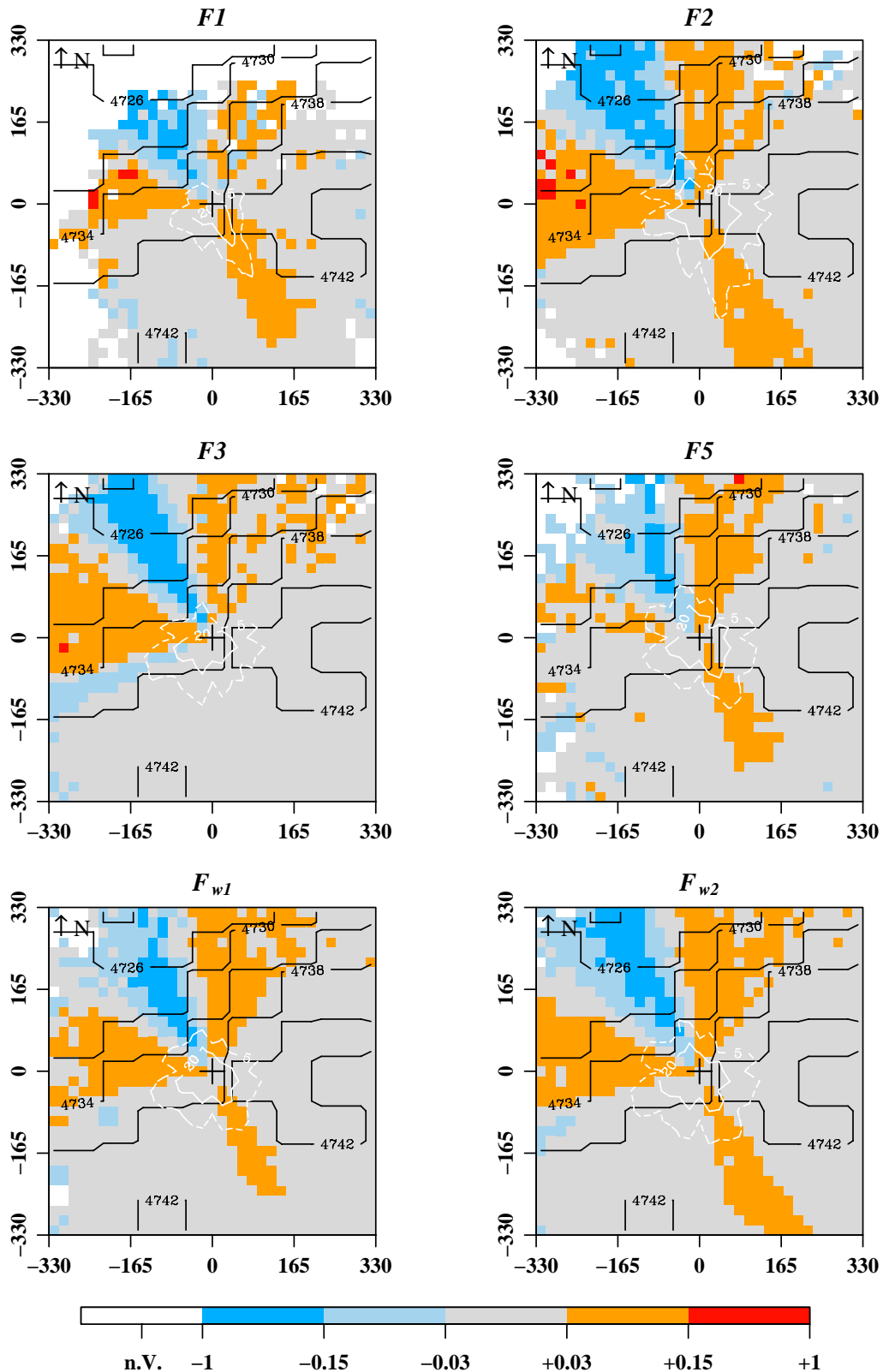
Figure 4-13: Spatial distribution of the median vertical wind speed after Planar Fit Rotation. Values of different footprint periods (labeled with 'F', followed by the period's code) are displayed related to the footprint climatology. The position of the flux measurement is indicated by the central cross-hairs. 5 wind speed classes are distinguished according to the color bar; n.V. indicates that no datasets were available for the matching cell. Black contour lines indicate the elevation a.s.l. [m]; white contour lines display the 5% (dashed) and 20% (solid) effect level rings of the measurements.

the year and also appear in parameterization approach F_{w1} / F_{w2} (Figure 4-12). Narrow upwind / downwind sectors exceeding / undercutting the threshold in SSE / E appear in F1 and F2 / F5 respectively. However, in parameterization approach F_{w1} / F_{w2} corresponding sectors do not display a violation of the threshold anymore. According to the effect level rings, both temporal and persisting structures contribute to the measurement.

Footprint periods F1 and F2 must be regarded as reference, since only during these periods proper mounting of the sonic anemometer can be attested. Even though e.g. the narrow upwind sector in SE appears only here but not in parameterization approach F_{w1} / F_{w2}, it can neither be attributed to a temporal pattern nor be explained by local topography. Rather the vanishing of this characteristic in time and the appearance of a new substantial downwind sector in the E of the measurement in F5 can be interpreted as an aftereffect of the sonic displacement.

After coordinate rotation (Figure 4-13), all footprint periods but F3 and F4 agree with the parameterization approach F_{w1} / F_{w2}: Best sector regarding the elimination of the vertical wind speed for half hour means is SW. Due to coordinate rotation the wind field is clearly leveled in the E area, but the pronounced downwind sector in the NW and three relatively mild upwind sectors in W, NE and SE remain, agreeing with earlier findings (Metzger et al., 2006). The effect level rings indicate that the remaining up- / downwind sectors still contribute to the central footprint and must therefore be discussed critically. The persisting upwind sector in the W of the measurement can be explained by flow distortion due to the LI-COR gas analyzer located in this sector, whereas the persisting downwind sector in the NW and a disturbed sector in the N can be related to flow distortion by the main body of the CSAT3 and the mounting stand respectively. Only in footprint periods F3 and F4, a mediocre upwind sector in SE disappears, coinciding with less southeasterlies during these periods (Figure 4-1). As for the downwind in the NE sector for unrotated values, the installed PBL tower and container for gas measurement can be taken into account for an interpretation.

4.1.2.3   Sensible heat flux

The quality tests for the sensible heat flux consist of the ITC for the vertical wind and the temperature (except for neutral stratification) plus the stationarity test for the covariance of these two parameters (Table 2-1).

At this, neglecting the ITC for temperature, the central footprint is rated 3 or better (Figure 4-14) in general, whereas the measurement position itself is rated 2 and even downgraded to quality flag 5 during F2 and F4. Two sectors continuing to the extended footprint, in SW and from NE to SE, display degraded quality, which mainly stems from neutral conditions prevailing at 54.4 % (Table 4-1) of all cases. During unstable stratification (33.0 % of all cases), now applying the ITC for temperature, the central footprint is rated 3 or better with a deterioration of quality in the E of the measurement. In contrast, measurements during stable conditions (15.6 % of all cases)

are ranging from 3 to 5 with an improvement of quality towards E. As for unstable conditions, mainly all periods but F2 cause the quality aggravation in the E sector. Under neutral conditions, all periods but F1 result in mediocre to bad quality ratings in NW, NE to E and SW in the overview. On the other hand, all periods except for F3 contribute to the sector of bad measurement quality from S to W under stable stratification. Non-stationarity and temperature ITC both more result in a bad quality rating for the E sector under unstable conditions than vertical wind ITC (Figure 4-15, Figure 4-16). Hereby, Figure 4-16 displays a maximum for bad quality ratings of 1 ‰ in this sector. It can be seen from Figure 4-15, that non-stationarity also prevails over vertical wind ITC for neutral conditions, causing the spatial quality characteristics as detected above.
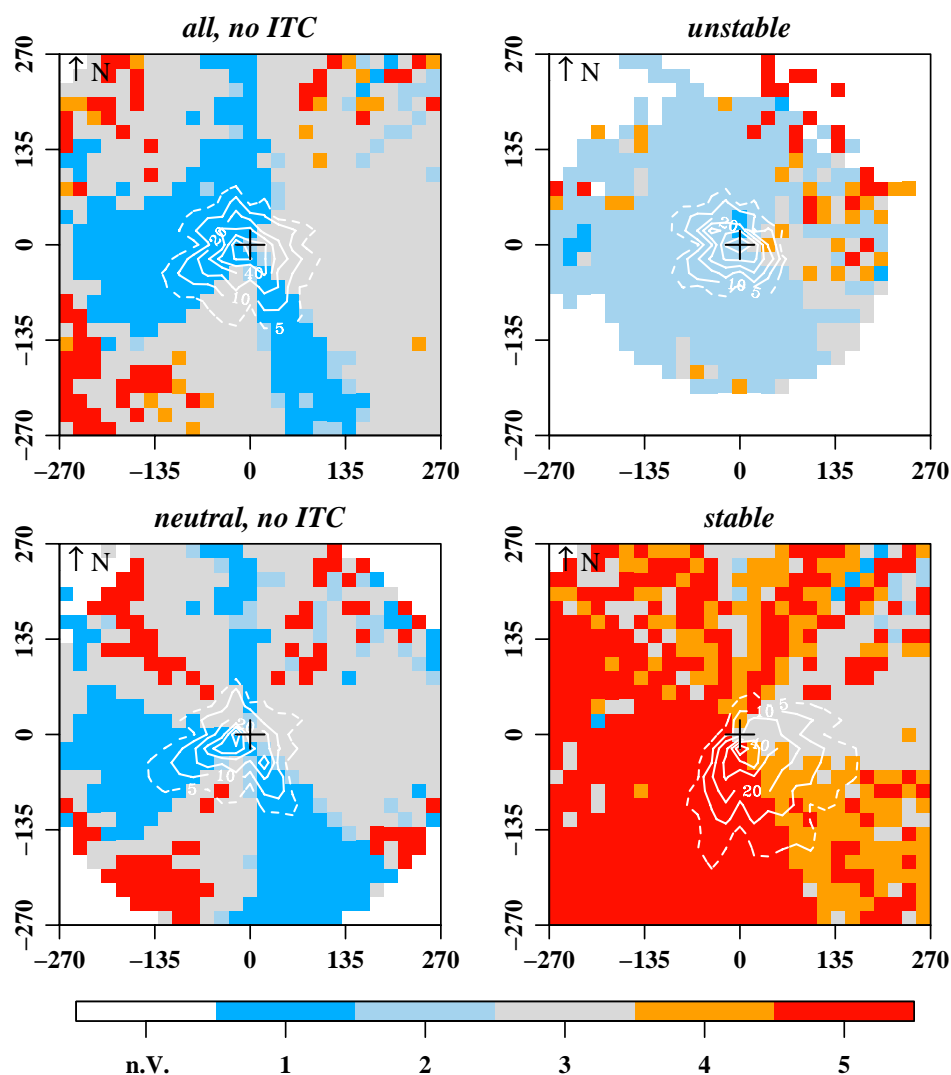

Figure 4-14: Quality rating for the sensible heat flux according to stratification, scenario F_{w1}, as related to footprint climatology. The position of the flux measurement is indicated by the central cross-hairs. 5 quality classes are distinguished according to the color bar; n.V. indicates that no datasets were available for the matching cell. Black contour lines indicate the elevation a.s.l. [m]; white contour lines display the 5% (dashed) and 10%, 20%, 40%, 60%, 80%, 100% (solid) effect level rings of the measurement.
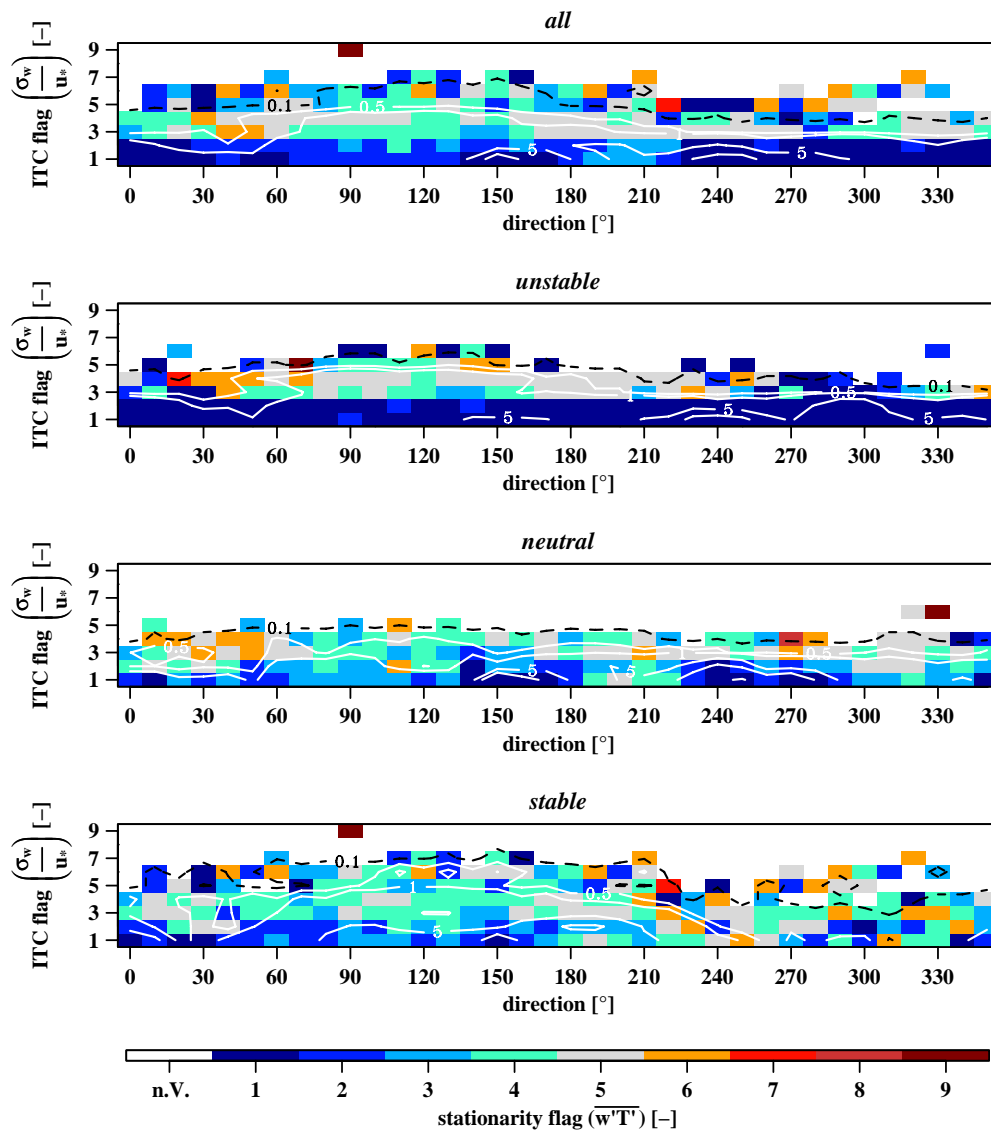
Figure 4-15: Spatial distribution for the median of stationarity according to vertical wind ITC classes for the sensible heat flux over the whole observation period for different stratification regimes. 9 quality classes are distinguished according to the Y-axis and the color bar; n.V. indicates that no datasets were available for the matching cell. Contour lines display the relative measurement density in 0.1 (dashed, black) and 0.5, 1, 5, 10, 20, 30, 40 (solid, white) ‰.

Also for stable stratification, vertical wind ITC displays advantage against stationarity, that aggravates especially for the SW sector (Figure 4-15). For other sectors temperature ITC contributes to quality decreases to the same extend or more than stationarity, particularly in S and SW with a contribution maximum of 10 ‰ (Figure 4-16).

4.1.2.4   Latent heat flux

The quality tests for the latent heat flux consist of the ITC for the vertical wind and the stationarity test for the covariance of vertical and horizontal wind (Table 2-1).
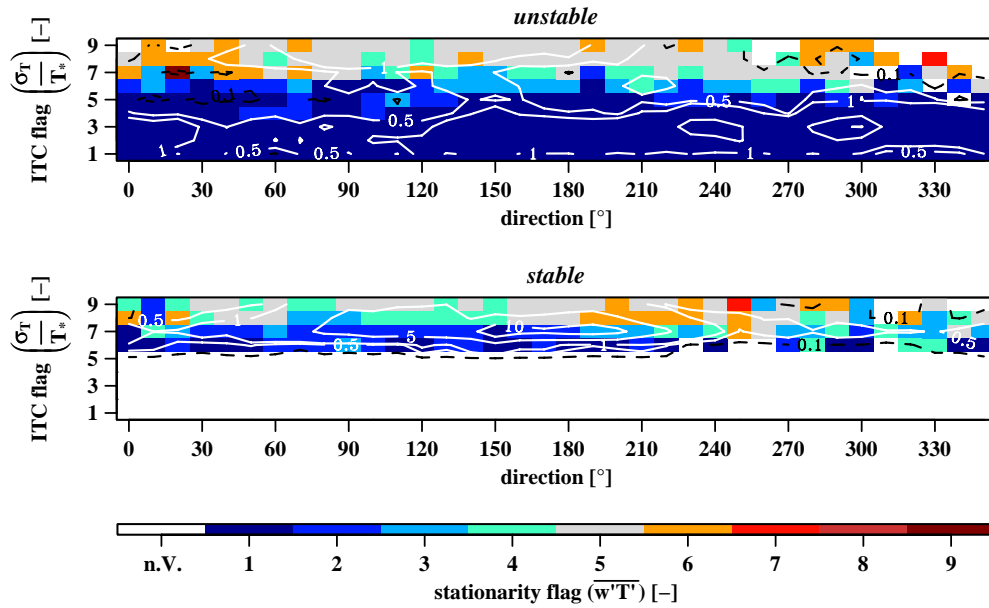
Figure 4-16: Spatial distribution for the median of stationarity according to temperature ITC classes for the sensible heat flux over the whole observation period for different stratification regimes. 9 quality classes are distinguished according to the Y-axis and the color bar; n.V. indicates that no datasets were available for the matching cell. Contour lines display the relative measurement density in 0.1 (dashed, black) and 0.5, 1, 5, 10, 20, 30, 40 (solid, white) ‰.

At this, quality structures of the latent heat flux measurement resemble those of the sensible heat flux for a large part (Figure 4-14, Figure 4-17), with a more pronounced sector of degraded quality ratings in E. Merely measurements under unstable and stable conditions are rated better because of the cease of applying ITC to the humidity time series. The central footprint is again rated 3 or better in general (Figure 4-17), but the measurement position itself is in the overall flagged 3 and during F3 and F4 even downgraded to flag 5. As for unstable conditions, F3, F4 contribute but F5 tips the scales for the badly rated E sector. Under neutral conditions, F1 contributes to the degraded structure in NW, whereas all other periods result in the quality characteristic displayed on the whole. On the other hand, F2 and F5 contribute to the degraded structure in S to NW during stable conditions, whereas F3 and F4 exclusively bring in bad flags for the entire plotting region. As for the measurement of latent heat, in all cases of decreased quality ratings non-stationarity of the time series prevails over ITC of the vertical wind (Figure 4-18), with an accentuation for the SW sector under stable stratification.
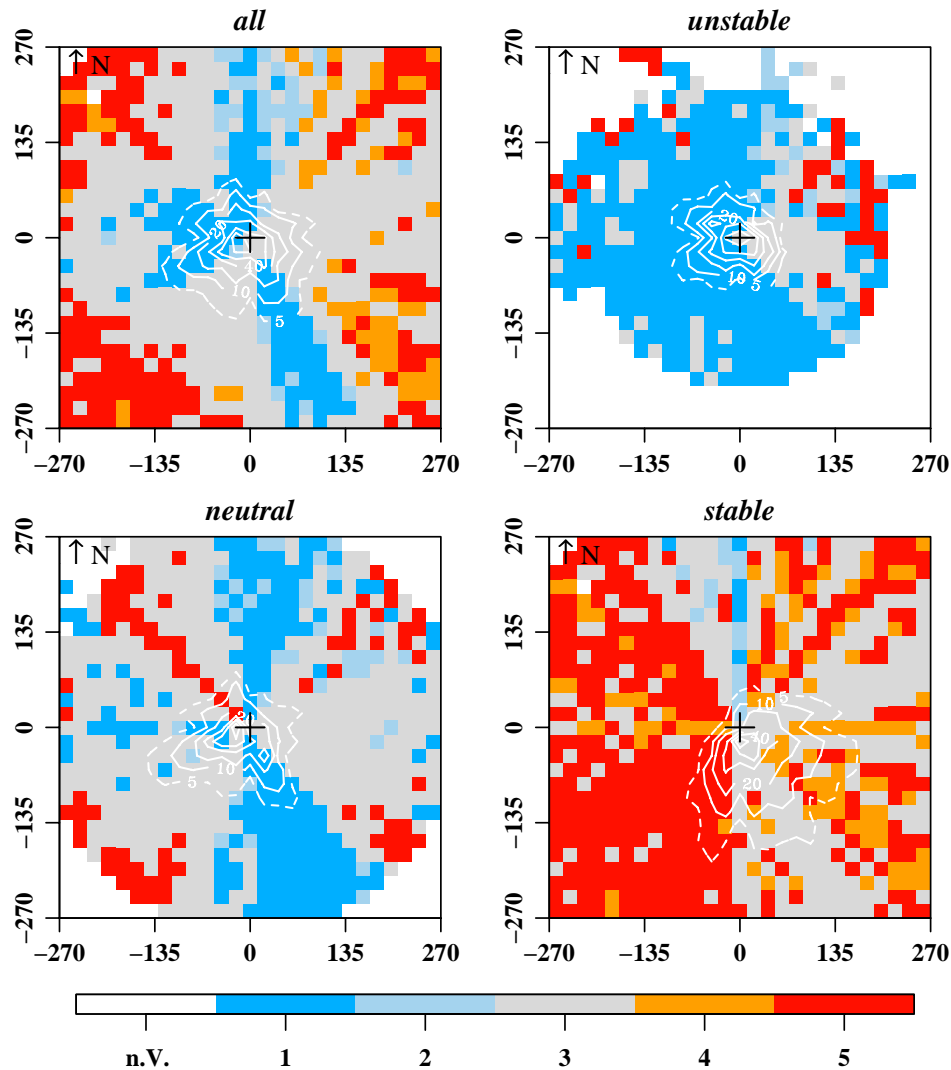
Figure 4-17: Quality rating for the latent heat flux according to stratification, scenario F_{w1}, as related to footprint climatology. The position of the flux measurement is indicated by the central cross-hairs. 5 quality classes are distinguished according to the color bar; n.V. indicates that no datasets were available for the matching cell. Black contour lines indicate the elevation a.s.l. [m]; white contour lines display the 5% (dashed) and 10%, 20%, 40%, 60%, 80%, 100% (solid) effect level rings of the measurement.

4.1.2.5 Momentum flux

The quality tests for the momentum flux consist of the ITC for the horizontal and vertical wind plus the stationarity test for the covariance of the forenamed parameters (table).

At this, quality structures of the momentum flux, exclusive of neutral and stable stratification individually, roughly agree with those of the other flux measurements, but are more uniform barely displaying the worst rating of 5 (Figure 4-14, Figure 4-17, Figure 4-19). Neutral stratification displays better quality than the other fluxes, besides deterioration in SE. Stable conditions actually displays a W-E mirror image to
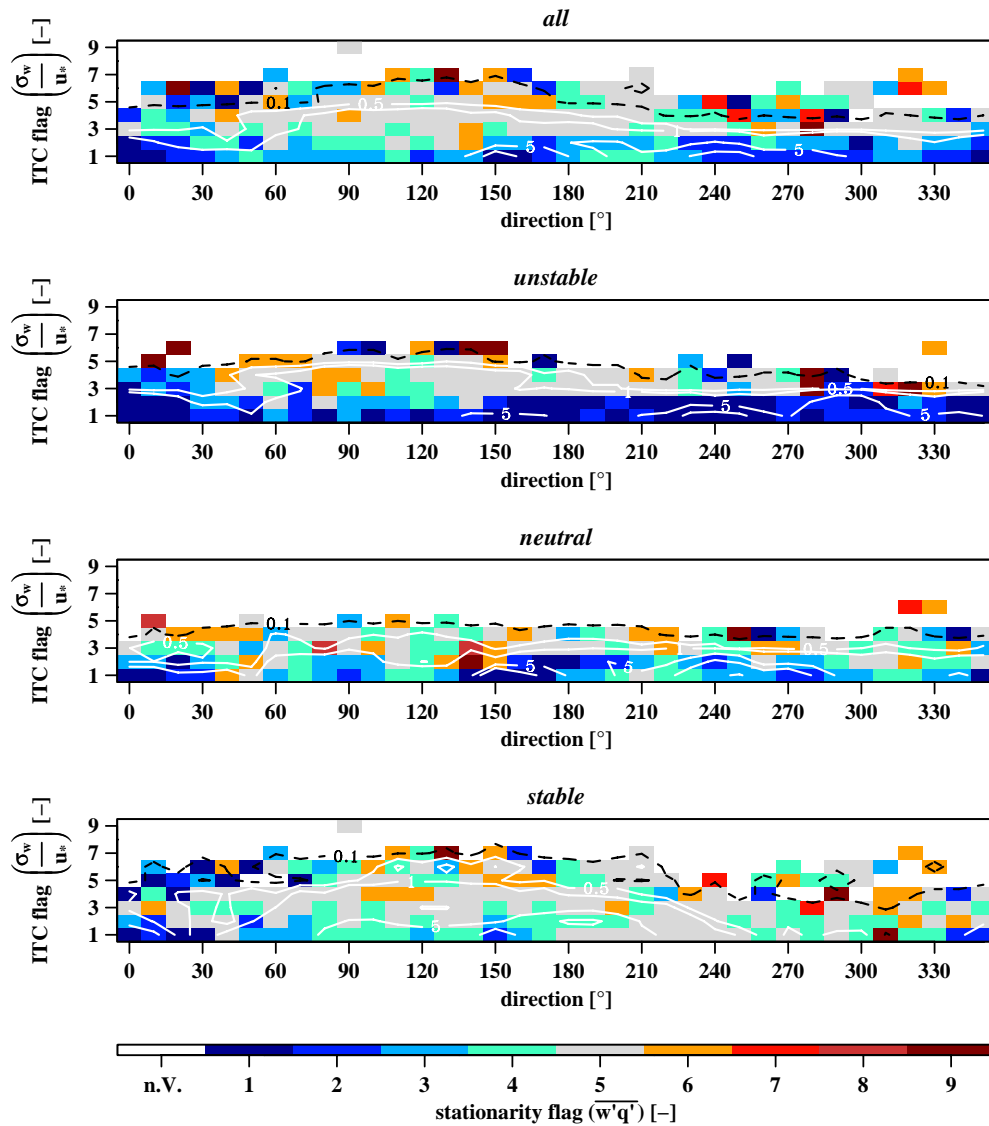
Figure 4-18: Spatial distribution for the median of stationarity according to vertical wind ITC classes for the latent heat flux over the whole observation period for different stratification regimes. 9 quality classes are distinguished according to the Y-axis and the color bar; n.V. indicates that no datasets were available for the matching cell. Contour lines display the relative measurement density in 0.1 (dashed, black) and 0.5, 1, 5, 10, 20, 30, 40 (solid, white) ‰.

the other fluxes, with better ratings in the W instead of E. The central footprint is rated 4 or better in general (Figure 4-19), whereupon the measurement position itself is rated quality flag 3 and during F1 and F2 actually downgraded to flag 4. As for unstable conditions, mainly F3, F4 and F5 cause the quality aggravation in the E sector. Under neutral conditions, F1 contributes to the degraded structure in the NE and all remaining periods particularly result in the NW-SE corridor of mediocre quality ratings. On the other hand, F1 also contributes to the mediocre ratings in the E sector during stable conditions, whereas the remaining periods, particularly F3 to F5 result in the consistently degraded ratings for the E half space.
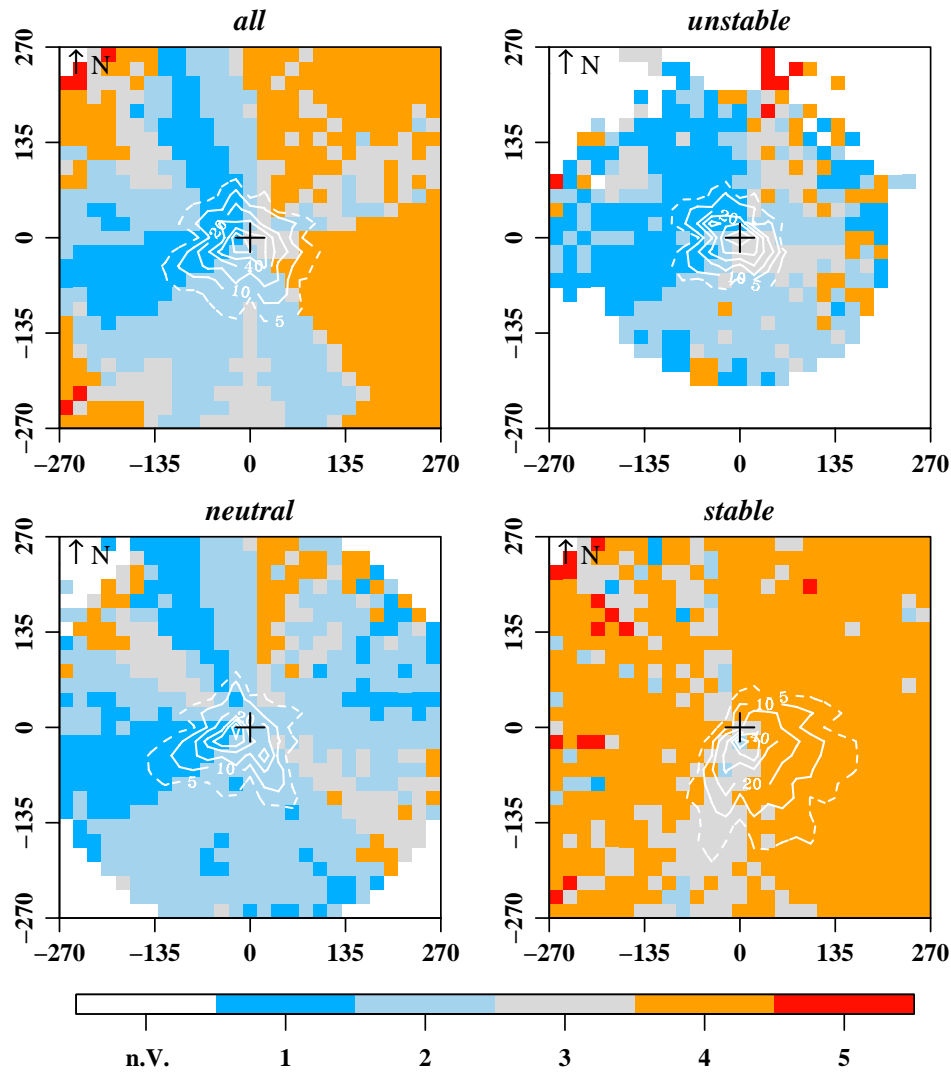
Figure 4-19: Quality rating for the momentum flux according to stratification, scenario F_{w1}, as related to footprint climatology. The position of the flux measurement is indicated by the central cross-hairs. 5 quality classes are distinguished according to the color bar; n.V. indicates that no datasets were available for the matching cell. Black contour lines indicate the elevation a.s.l. [m]; white contour lines display the 5% (dashed) and 10%, 20%, 40%, 60%, 80%, 100% (solid) effect level rings of the measurement.

As for the measurement of the momentum flux, rather failure of horizontal wind ITC criteria (Figure 4-21) for the sectors discussed above is responsible for mediocre quality ratings than vertical wind ITC or stationarity (Figure 4-20).

Furthermore, a contribution maximum of 5 ‰ is displayed for stable conditions around SE for ITC flag 6 (Figure 4-21).

4.1.2.6 CO$_2$ flux

The quality tests for the CO$_2$ flux consist of the ITC for the vertical wind and the stationarity test for the covariance of vertical wind and CO$_2$ concentration (Table 2-1). At this, quality structures of the CO$_2$ flux measurement in the whole resemble those of the sensible- and latent heat flux, but not exactly for neutral and stable stratification
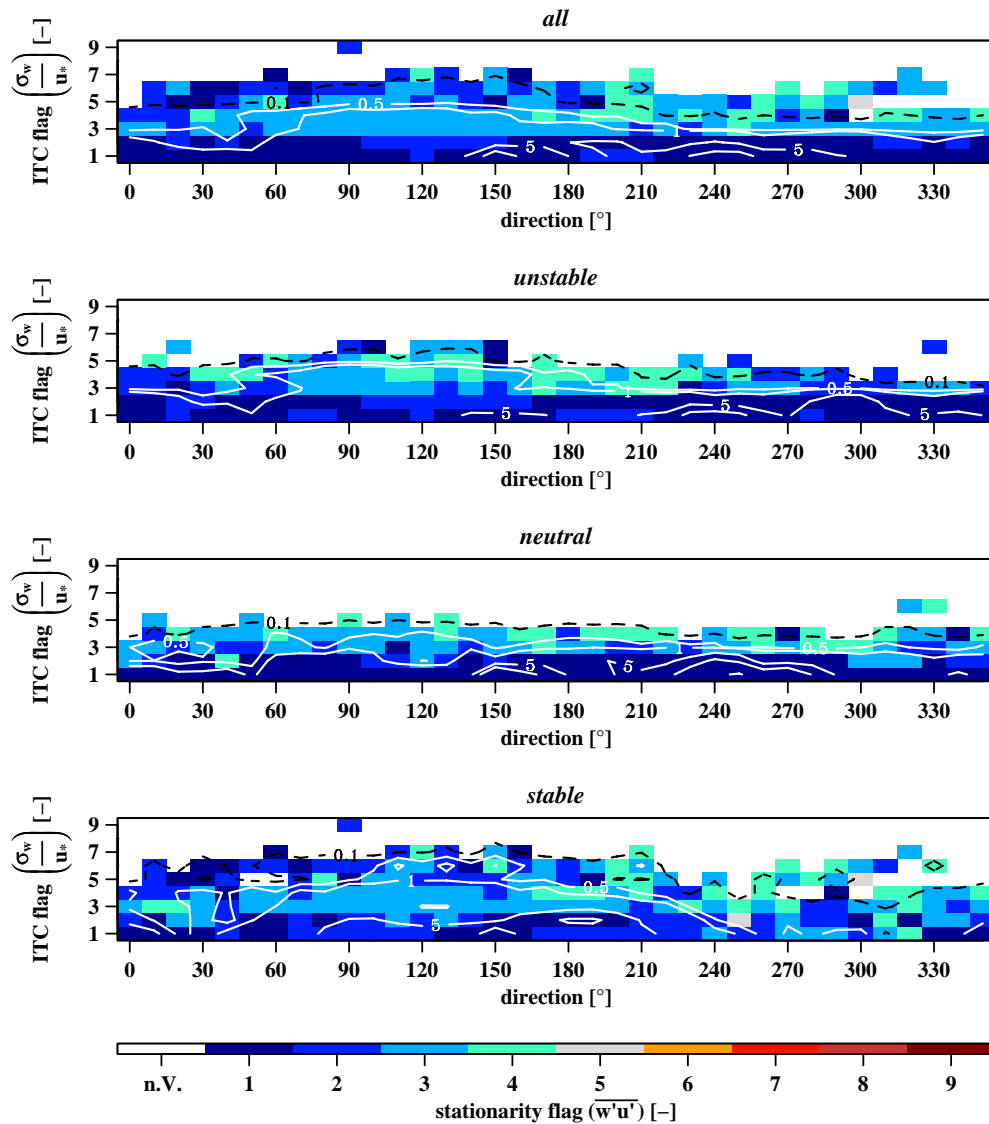
Figure 4-20: Spatial distribution for the median of stationarity according to vertical wind ITC classes for the momentum flux over the whole observation period for different stratification regimes. 9 quality classes are distinguished according to the Y-axis and the color bar; n.V. indicates that no datasets were available for the matching cell. Contour lines display the relative measurement density in 0.1 (dashed, black) and 0.5, 1, 5, 10, 20, 30, 40 (solid, white) ‰.

(Figure 4-14, Figure 4-17, Figure 4-22) individually: During neutral stratification, the N sector of good quality rating is less pronounced and stable stratification does not display as bad ratings in NW as the forenamed fluxes. The central footprint is rated 3 or better in general (Figure 1-21), whereupon the measurement position itself is only rated quality flag 3 and during F3 actually downgraded to flag 5. As for unstable conditions, mainly F3, F4 and F5 cause the quality aggravation in the E sector. Under neutral conditions, all periods but F4 participate with bad quality ratings from NW to SE. On the other hand, F3 to F5 also mainly contribute to the degraded structures in NE and SW during stable conditions, whereas F2 contributes to the latter (SW), too. Quality characteristics of the CO_2 flux are reminiscent to those of the latent heat flux
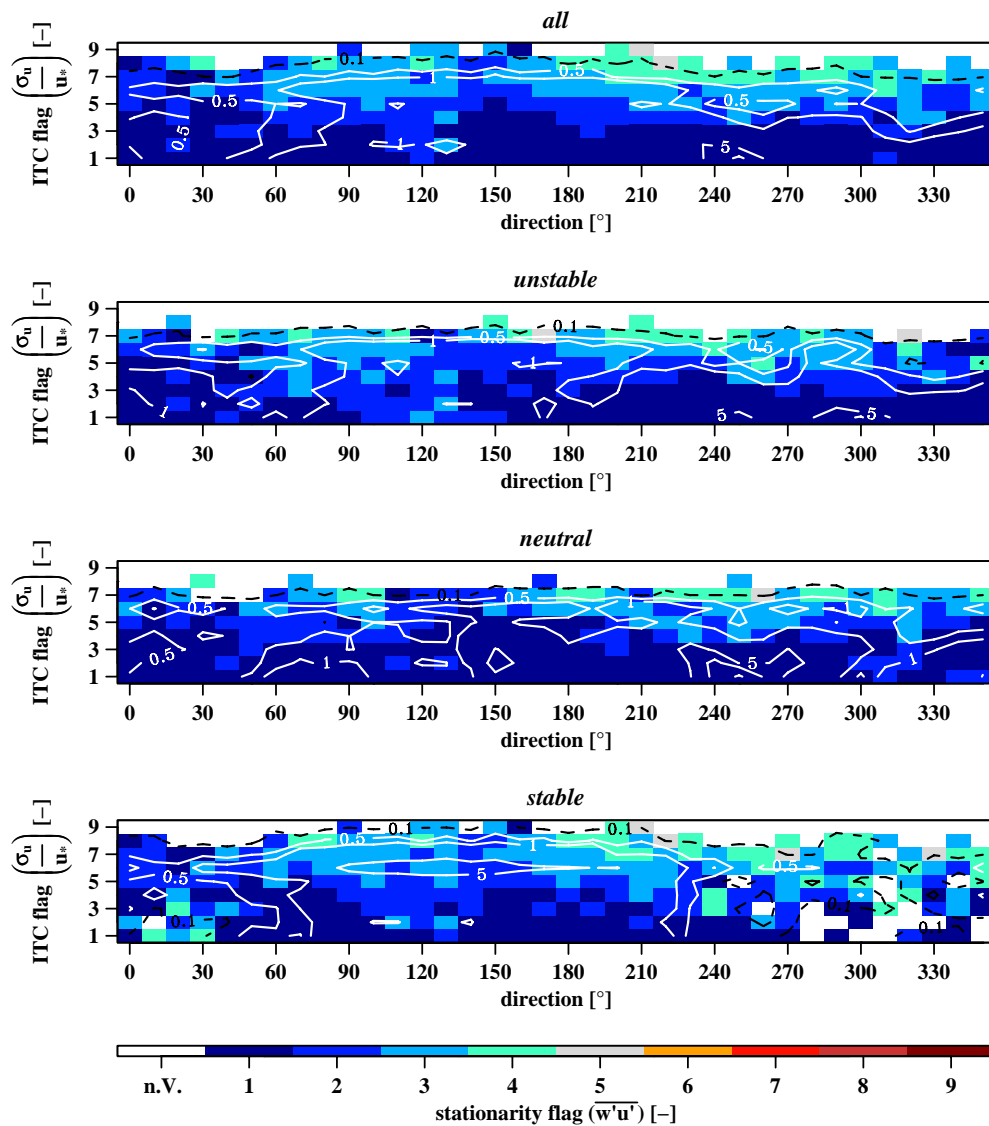
Figure 4-21: Spatial distribution for the median of stationarity according to horizontal wind ITC classes for the momentum flux over the whole observation period for different stratification regimes. 9 quality classes are distinguished according to the Y-axis and the color bar; n.V. indicates that no datasets were available for the matching cell. Contour lines display the relative measurement density in 0.1 (dashed, black) and 0.5, 1, 5, 10, 20, 30, 40 (solid, white) ‰.

(Figure 4-18): in all cases of decreased quality ratings non-stationarity of the time series prevails over ITC of the vertical wind.

Detailed investigation of a data subset for the SE wind sector period from 2005-09-25 to 2005-10-01 (later referred to as SE wind sector period) has shown that for CO_2 measurement 8% of all half hour means in the SE sector are flagged 5, compared to 2 % of all half hour means in all other directions. Thereby 93% of the values in the SE sector failed due to stationarity criteria, the remaining 7% due to the ITC.
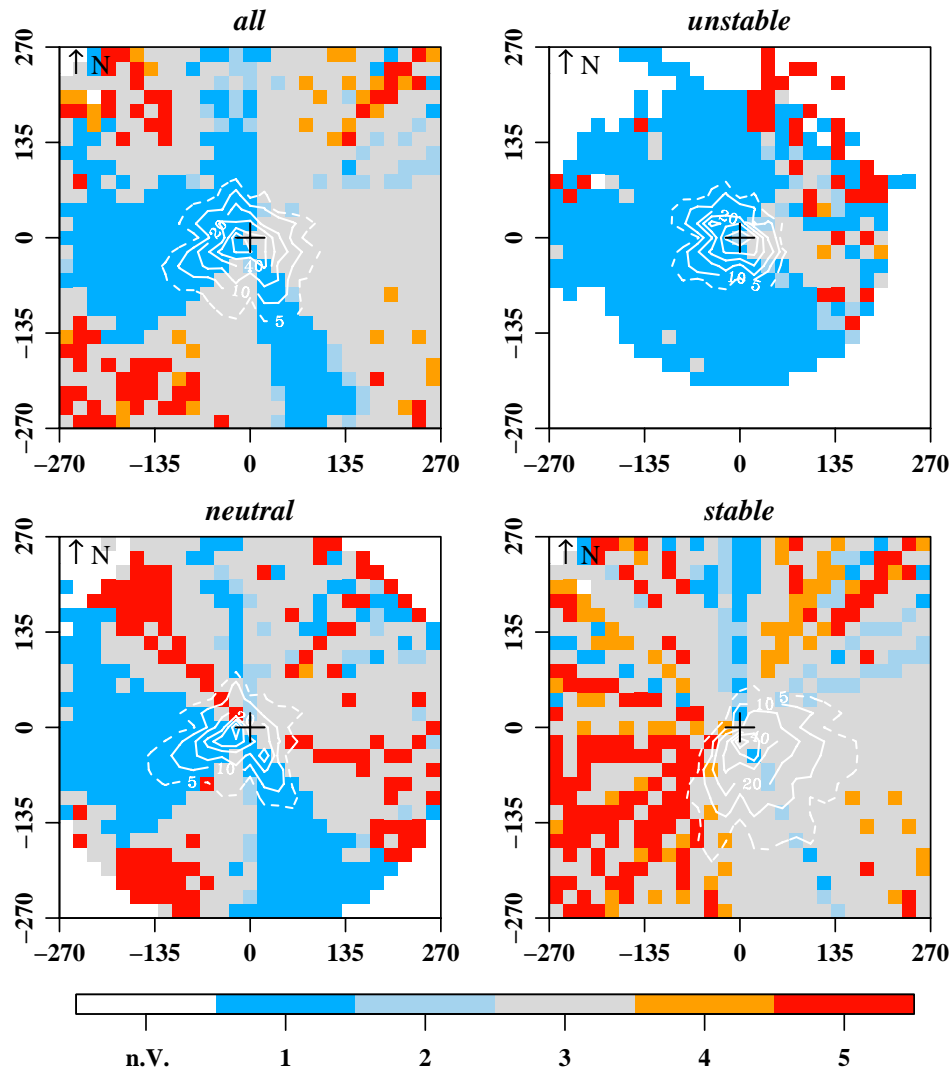
Figure 4-22: Quality rating for the CO_2 flux according to stratification, scenario F_{w1}, as related to footprint climatology. The position of the flux measurement is indicated by the central cross-hairs. 5 quality classes are distinguished according to the color bar; n.V. indicates that no datasets were available for the matching cell. Black contour lines indicate the elevation a.s.l. [m]; white contour lines display the 5% (dashed) and 10%, 20%, 40%, 60%, 80%, 100% (solid) effect level rings of the measurement.

4.1.3   Comprehension

Daytime NEE (Figure 4-7) is only heavily depressed from begin to mid of November 2005, and highest CO_2 uptake rates take place in March at supposedly 20 cm snow cover. The November 2005 NEE depression concurs with a snow cover according to surface Albedo (Figure 4-3) and decreased daytime Bowen ratio (Figure 4-7), supposedly due to thawing processes. Albedo only shows likewise high values only for few days in October 2005 and February 2006, for other times Albedo also agrees with those of dry grey soil (Geiger et al., 1995). At this, a closed snow cover from October 2005 to May 2006 as reported by the Chinese station operators and utilized for the footprint statements has to be put in question. Besides, outgoing longwave radiation (Figure 4-5) from March to June 2006 exceeding 450 Wm^{-2} emphasizes this

suspicion: Assuming a surface temperature of 1.0 °C of melting snow, the maximum possible outgoing longwave radiation for a snow cover would amount to 307.5 Wm^{-2} (Equation 2-18). Even admitting temperatures slightly higher than 10.0 °C, in a thin layer of melting water atop the snow layer, an outgoing longwave radiation of ≈350 Wm^{-2} could not be exceeded. Therefore, reported snow periods don't match with the findings according to the meteorological measurements, a snow period could be accepted at the utmost until end of February 2006.

As for the effect of a shortened snow period on the footprint results, one has to recall that different parameterization of surface roughness and measurement height alters both, effect level rings and vertical wind or quality feature characteristic by the same scaling factor. For this reason, except for the absolute extend of the footprint, structures of both remain preserved for either approach, in particular for the central footprint, and consequentially allows qualitative interpretation.

Regarding land use, Namco site perfectly meets the requirement of having available data that reliably represents a specific type of ecosystem, in this case high alpine grassland.

The situation concerning the influence of local topography on the measurements can be described as comparatively good. But although the effects of the misplacement on the vertical wind field could be corrected within certain resolution limits, additional sensor induced flow distortion must still be reckoned on the calculation of fluxes. Eventually, a sector of ±60 ° opposite the main wind direction should be generally discarded because of flow distortion due to the measurement construction (Foken, 2006). Still, the SE wind sector with constant upwind characteristics for unrotated and rotated values except for F3 and F4 can neither be addressed by the installation, nor by local topography. Contrariwise free fetch condition is given for several kilometers (Figure 3-1).

A degradation of quality rating for the central footprint during wintertime and an enhancement in the warmer time of the year affects all measurements. Generally speaking, non-stationarity of the time series or, where available, ITC for air constituents but barely vertical wind ITC, reveals problematic sectors at Namco station. In average, the central footprint is not rated worse than 3 for all of the fluxes, with few exceptions for the momentum flux occasionally rated 4. Consulting the interpretation of the quality flags as given in chapter 2.4.4, the average measurement quality is evaluated (Table 4-2). Best fluxes for fundamental research with more than 55 % utilizable half hour means are the sensible heat- and the momentum flux, whereas the CO_2- and latent heat fluxes fall behind. For the calculation of monthly or annual sums 75.2 % / 61.5 % and 59.7 % of the half hour means of sensible heat- / CO_2- and latent heat-flux, respectively, can be utilized.

Reduced quality sectors in the central footprint for all fluxes under all stratifications intersect with the SE-NW and SW-NE transects of reduced quality seen from the extended footprints (Figure 4-9, Figure 4-14, Figure 4-17, Figure 4-19). The omnidirectional effects observed agree throughout the different fluxes, therefore flux

Table 4-2: Distribution of measurement quality for the four different fluxes throughout the whole observation period and average station quality (Ø) over all fluxes.

Quality	Q_H	Q_E	u_*	Q_C	Ø
fundamental	57.5	41.5	56.2	47.5	50.7
long-term	17.7	18.1	32.2	14.0	20.5
discard	24.8	40.3	11.6	38.5	28.8

specific causes for quality degrading, such as an additional heat source for the sensible heat flux, can not explain the structures observed. Bad ratings in the NW, NE and SW sector can be explained by flow distortion: the main body of the CSAT3 is placed in the NW, whereas the mast holding the installation is located NE and the SW sector bears two 1 m high solar panels installed 10 m from the measurement. Additionally, PBL tower and gas measurement container in the NE might be withdrawn for reduced quality in this sector. Contrary to the findings of the vertical wind assessment, no interference with EC assumptions is detected in the E sector, where the LI-COR gas analyzer is installed. On the other hand, in the SE sector of reduced quality no obstacles in the fetch of the measurement can be found.

This leaves the SE sector, with an almost perfect level fetch but nevertheless pronounced upwind and bad quality ratings. Here, detailed investigation of the SE wind sector period has shown that for the discussed period four times more values of the CO_2 flux are flagged 5 for the SE sector compared to all other directions, nearly all of them due to instationarity. Recalling the fact that the quality flag assigned to one cell is the median of all measurements with any contribution factor little higher than 0% emphasizes the significance of this subset analysis with throughout higher contributions. Together with the interaction of wind direction, wind speed and stability, these findings give way to the hypothesis, that the instationarity is not caused locally but due to mesoscale flow patterns of the further environment, including Lake Namco and the mountain range in 15 km distance SSE.

4.2 Everest site

4.2.1 Meteorological data

A clear diurnal cycle of wind direction can be identified (Figure 4-23) for the non-monsoon period from October to April, southwesterlies dominate with a transition to northeasterlies during noontime. From begin of July to mid September a change of wind characteristics to northeasterlies can be detected. The wind direction is clearly related to topography. Catabatic wind leads to southwesterlies for the time of low or no solar radiation, whilst anabatic wind during noontime causes northeasterlies. Limitations of catabatic winds with a clear change of wind characteristics to northeasterlies can be detected for the monsoon season which stretches from begin of July to mid September in this region.

Horizontal wind speed values below 5 ms^{-1} dominate, whereupon a clear dependence of horizontal wind speed values exceeding 6.5 ms^{-1} on the non-monsoon season and hereby on the catabatic winds, in particular the glacier wind, is found.

Calculation of actual temperature over sonic temperature, as illustrated in chapter 2.5, showed a maximum alteration of -4.3 K after step 1 (Equation 2-13, Equation 2-14) and +0.1 K, 1.6 % relative to step 1 respectively, after step 2. The annual mean temperature of -0.2 °C after step 1 is only 1.2 K warmer than 270 m higher Namco station. The measurement thereby undercuts the Lhasa reference measurement
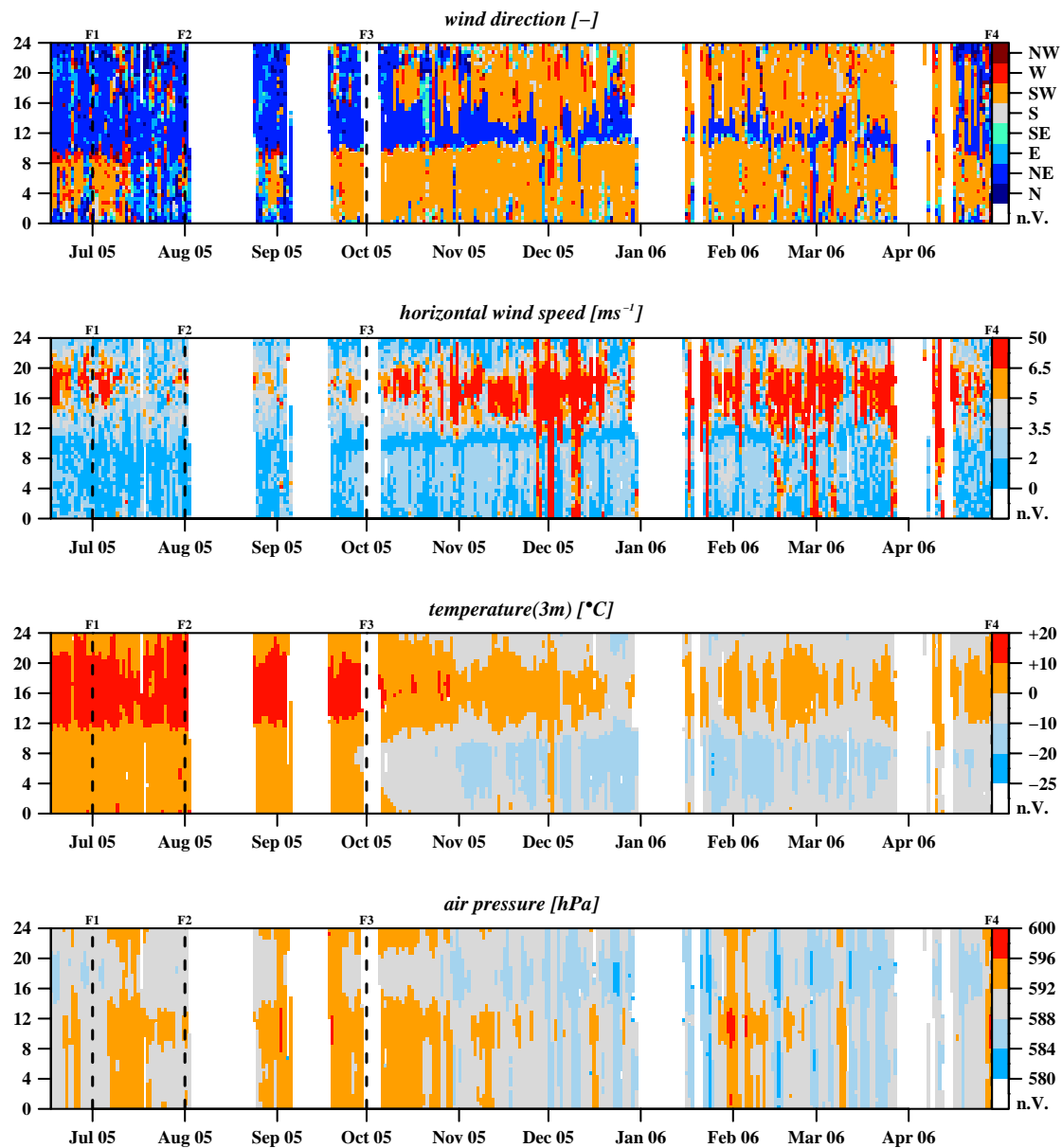

Figure 4-23: Wind direction [-], horizontal wind speed [ms^{-1}], temperature [°C] and air pressure [hPa] for the entire measurement period. X-axis displays the day of the year, Y-axis displays the time of the day, and colors represent quantities according to the color bar attached respectively. Footprint periods are separated by dashed lines, the end labeled with index 'F', each followed by the number of the period.

(Figure 3-3) by 8.8 K at an altitude difference of 825 m, displaying a vertical lapse rate of 10.4 Kkm^{-1}, even surpassing the dry adiabatic lapse rate of 9.8 Kkm^{-1}. This can be accredited to low humidity and the extreme exposure of the measurement in a narrow high alpine valley with comparatively less sunshine hours and local wind regimes. In the cold season of the year, daytime temperatures above the freezing point are still limited around sun apex but much more constant than at Namco station. Still, the measured air temperature values follow the annual cycle of the Lhasa reference station (Figure 3-3).

According to the barometric formula (Equation 2-19), conducting the 30 year average values of atmospheric pressure and temperature for Lhasa reference station (Figure 3-3) and the lapse rate as above as calculation basis, an annual mean atmospheric pressure of 587.9 hPa is expected at Namco station. Hereby the measured average of 587.9 hPa exactly agrees. Barring jerky leaps, one must be suspicious of the diurnal cycle as found similarly at Namco site, posting the same issues as discussed above.
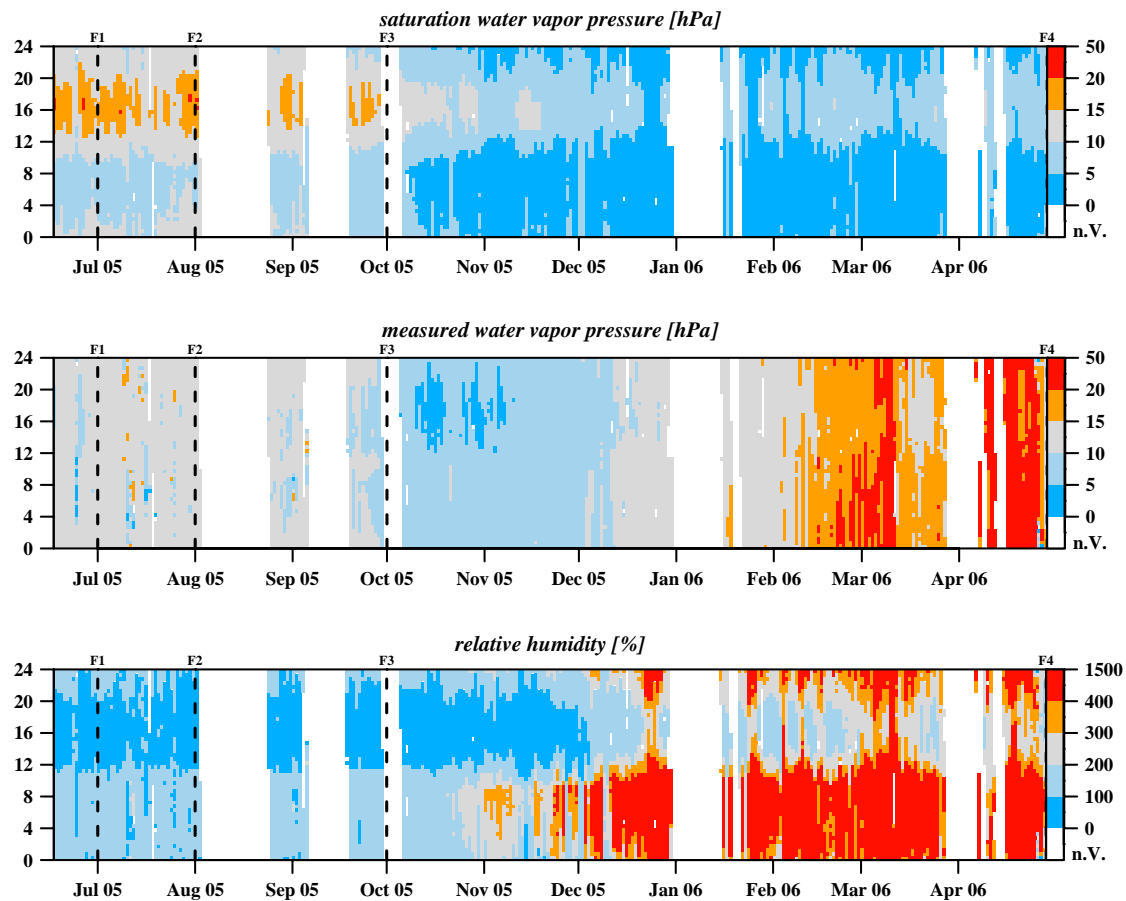

Figure 4-24: Measured water vapor pressure [hPa], saturation water vapor pressure [hPa] and relative humidity [%] for the entire measurement period. X-axis displays the day of the year, Y-axis displays the time of the day, and colors represent quantities according to the color bar attached respectively. Planar Fit Rotation periods are separated by solid lines, the beginning labeled with index 'R', each followed by the number of the period. Footprint periods are separated by dashed lines, the end labeled with index 'F', each followed by the number of the period.

As at the Namco site, the saturation water vapor pressure calculated according to the Magnus formula (Equation 2-15) rarely exceeds the preferably use criteria for infrared hygrometers of 10 hPa (Foken, 2006), again only in the warmer season of the year (Figure 4-24).

Calculation of water vapor pressure over absolute humidity and temperature, as illustrated in chapter 2.5, showed a maximum alteration of -0.47 °hPa after step 1 and +0.01 °hPa, 1.5 % relative to step 1 respectively, after step 2.

Relative humidity calculated for water vapor pressure values after step 1 show up to fifteen fold supersaturation for 78.0 % of all values, especially from December 2005 on, even though saturation water vapor pressure does not decrease noteworthy already from November 2005 on. At this the initiation of high supersaturation does not start abrupt as at Namco site. Applying the preferably use criteria for infrared hygrometers to the calculation of relative humidity would decrease supersaturation to a maximum of twofold for 31.4 % of all values, but discards 78,7 % of all values.
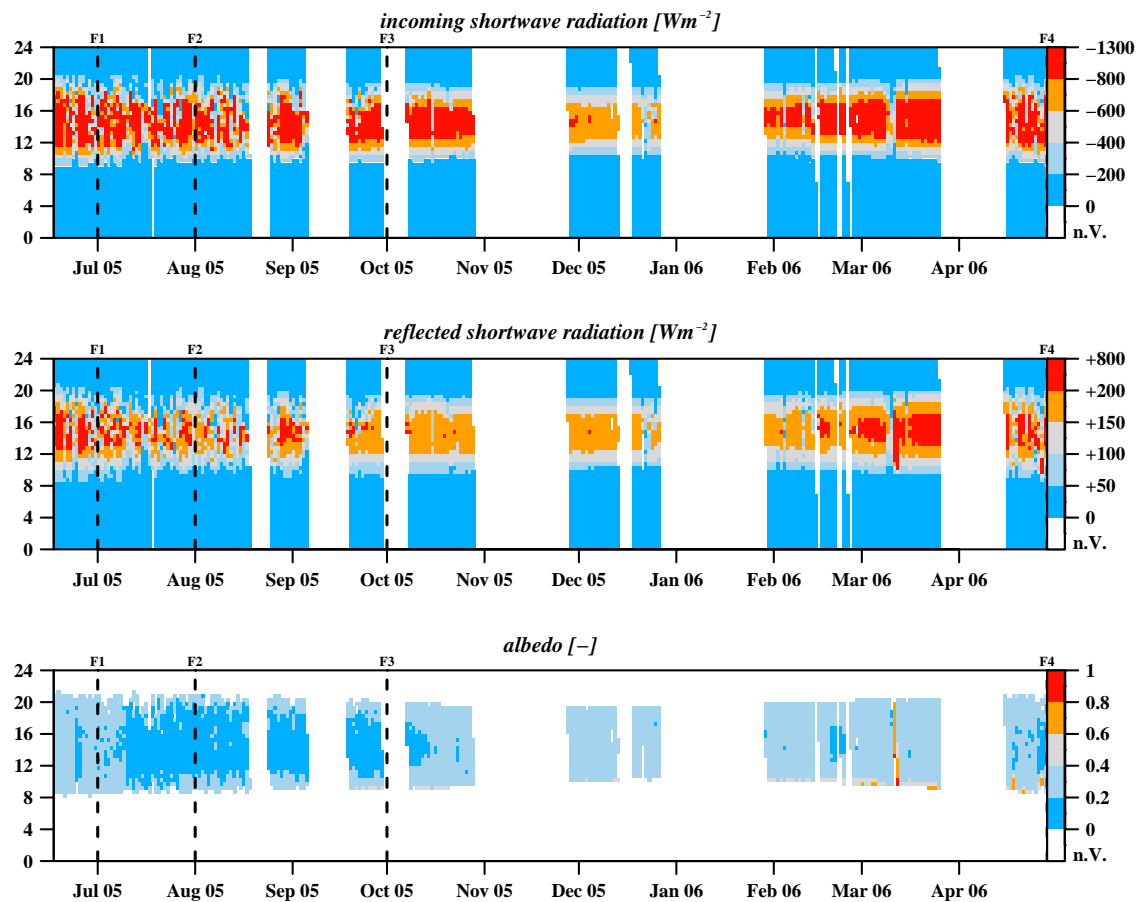
Figure 4-25: Incoming shortwave radiation [Wm^{-2}], reflected shortwave radiation [Wm^{-2}] and Albedo [-] for all cases the incoming shortwave radiation exceeds 50 Wm^{-2}, for the entire measurement period. X-axis displays the day of the year, Y-axis displays the time of the day, and colors represent quantities according to the color bar attached respectively. Planar Fit Rotation periods are separated by solid lines, the beginning labeled with index 'R', each followed by the number of the period. Footprint periods are separated by dashed lines, the end labeled with index 'F', each followed by the number of the period.

Possible reasons and measures for errors in the humidity measurement have been discussed in detail in chapter 4.1.1. The measurement at Everest site abandons the annual cycle of the calculated saturation water vapor pressure around March 2006. Ascertained errors seem to be a matter of offset for the span until then and a matter of drift thereafter. While turbulent measurements only display an offset but not a drift, no influence is to be expected on the flux calculation. Therefore, the latent heat flux calculated for the period after March 2005 must be discarded for the reason of drift in the humidity measurement.

4.2.1.1   Radiative fluxes

According to the dependency of solar radiation on the latitude (Equation 2-16), solar radiation at Everest site is slightly higher than at Namco site. Values ranging from -848.3 Wm^{-2} to -1365.0 Wm^{-2} between winter- and summer solstice are to be expected as extraterrestrial solar radiation. Considering an optical depth of 0.1 for
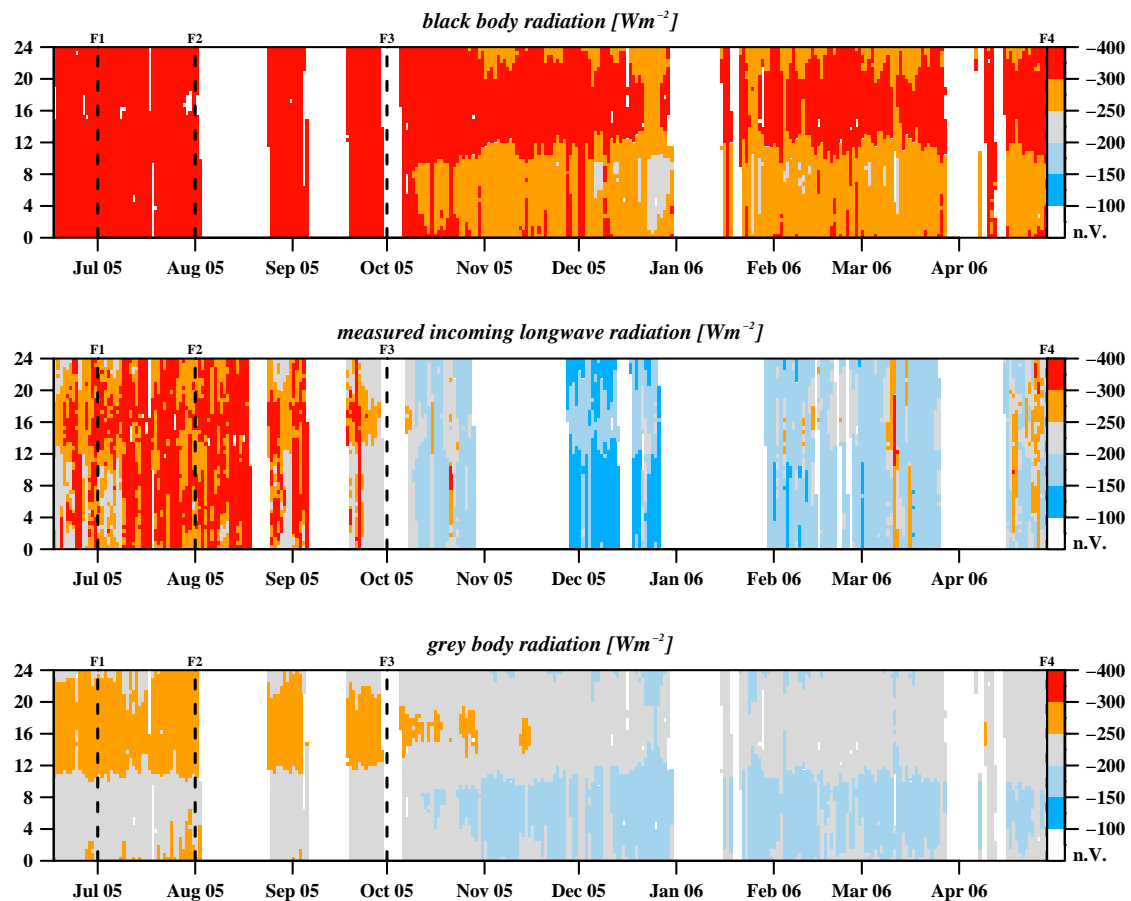

Figure 4-26: Black body radiation [Wm^{-2}], measured incoming longwave radiation [Wm^{-2}] and grey body radiation [Wm^{-2}] for the entire measurement period. Black- and grey body radiation are calculated after the Stefan-Boltzmann law with emissivities of 1 and 0.7 respectively. X-axis displays the day of the year, Y-axis displays the time of the day, and colors represent quantities according to the color bar attached respectively. Planar Fit Rotation periods are separated by solid lines, the beginning labeled with index 'R', each followed by the number of the period. Footprint periods are separated by dashed lines, the end labeled with index 'F', each followed by the number of the period.

clear and 0.8 for overcast conditions, daily maxima of solar radiation at surface level ranging from -233.1 Wm^{-2} to -721.8 Wm^{-2} at winter- and from -615.1 Wm^{-2} to -1234.7 Wm^{-2} at summer solstice are to be expected (Equation 2-17). Assuming that the solar radiation is the only shortwave radiation source and entirely emitted in the spectral range of the CM3 pyranometer use, which is from 305 nm to 2800 nm, measured incoming shortwave radiation (Figure 4-25) fits well within the calculated ranges, with more fluctuations during the monsoon season than at Namco site, that can be related to intermittent dense cloud cover and precipitation.

  Daytime Albedo values ranging from 0 to 1 indicate a proper measurement of the reflected shortwave radiation. Albedo agrees with values for dry grey soil (0.25 - 0.30) in the colder and dryer, with those of moist grey soil (0.10 - 0.12) and grass (0.18 – 0.20) for the warmer and wetter period of the year (Geiger et al., 1995). Maxima of Albedo exceeding 0.6 might indicate an occasional snowfall in March 2006, but persisting snow cover is not reported for Everest site.
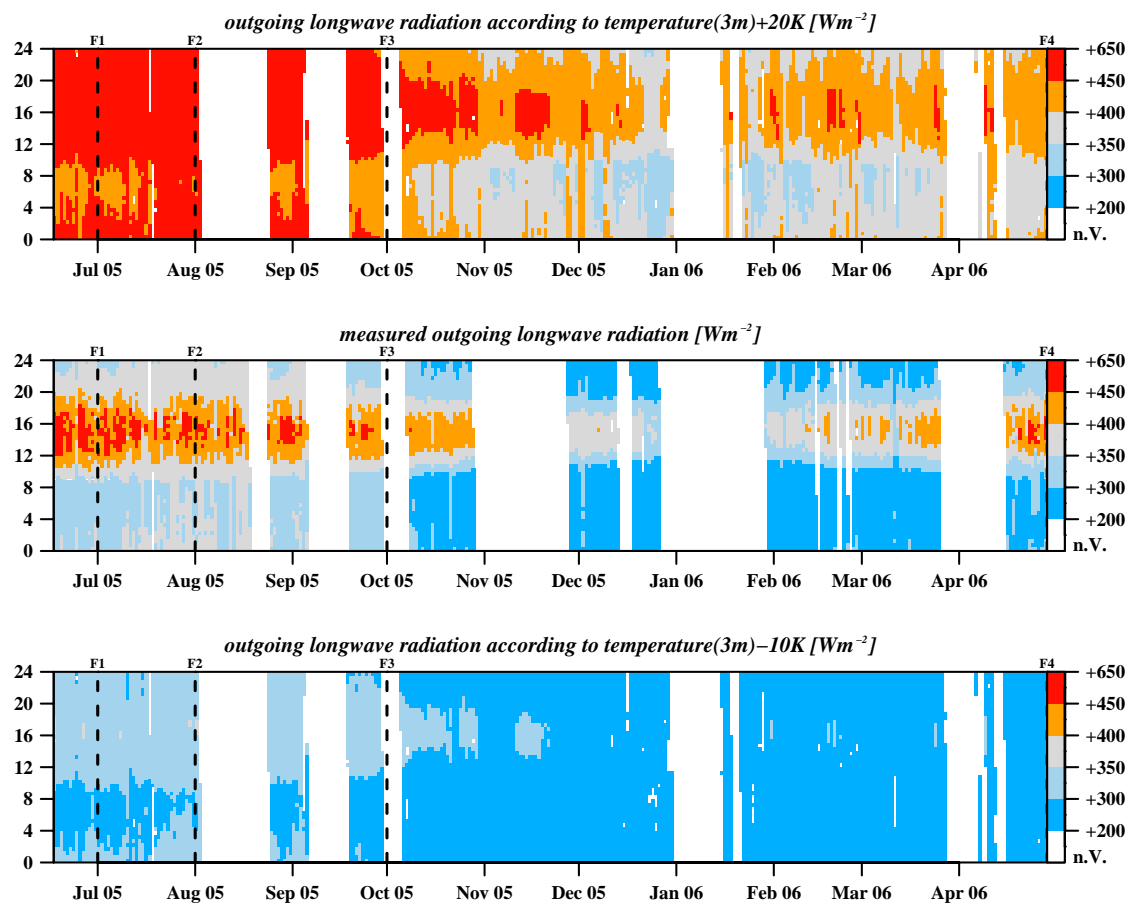

Figure 4-27: Outgoing longwave radiation according to temperature(3m)+20K [Wm^{-2}], measured outgoing longwave radiation [Wm^{-2}] and outgoing longwave radiation according to temperature(3m)-10K [Wm^{-2}]. Parameterizations according to temperature(3m) are calculated after the Stefan-Boltzmann law with temperature deviations as stated. X-axis displays the day of the year, Y-axis displays the time of the day, and colors represent quantities according to the color bar attached respectively. Planar Fit Rotation periods are separated by solid lines, the beginning labeled with index 'R', each followed by the number of the period. Footprint periods are separated by dashed lines, the end labeled with index 'F', each followed by the number of the period.

To check the plausibility of incoming longwave radiation, measured values are compared to black- and grey body radiation with emissivities of 1 and 0.7 respectively (Equation 2-18, Figure 4-26). At this, measured values match black body radiation during the warmer season, whereas two critical periods in August and September 2005 can not be tested because of lacking temperature values. Still, black body radiation before and thereafter agrees with the measurement and the reference climate chart (Figure 3-3) does not show a pronounced decline of temperature for this period. But measured values undercut grey body radiation full-time from October 2005 to January 2006 and during daytime from February to April 2006. Since these findings are analogous to those from Namco site, chapter 4.1.1.1 can be consulted for corresponding discussion.

To check plausibility of outgoing longwave radiation, measured values are compared to the black body radiation according to the measured temperature within
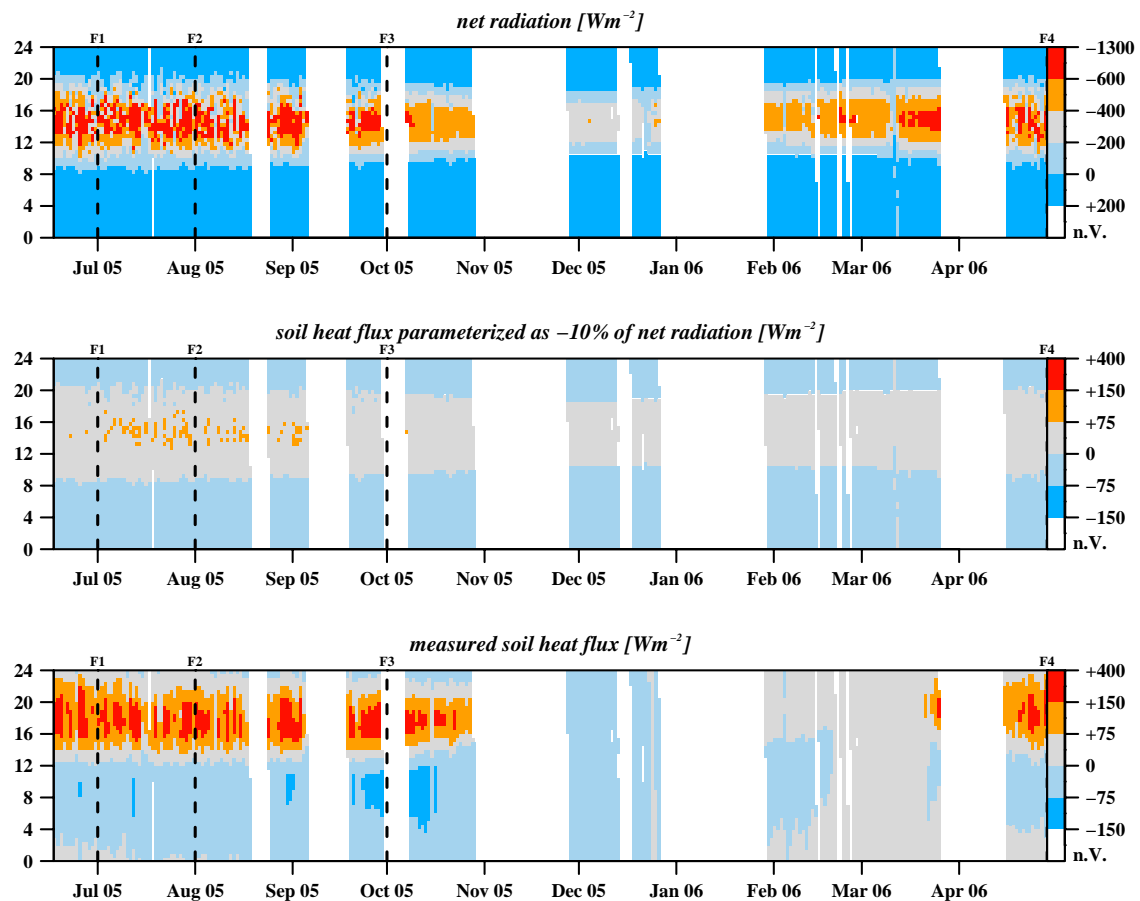

Figure 4-28: Net radiation [Wm^{-2}], soil heat flux parameterized as -10% of net radiation [Wm^{-2}] and measured soil heat flux [Wm^{-2}] for the entire measurement period. X-axis displays the day of the year, Y-axis displays the time of the day, and colors represent quantities according to the color bar attached respectively. Planar Fit Rotation periods are separated by solid lines, the beginning labeled with index 'R', each followed by the number of the period. Footprint periods are separated by dashed lines, the end labeled with index 'F', each followed by the number of the period.

certain ranges (Equation 2-18, Figure 4-27). In a mesoscale model approach covering an area near Namco site, 20 % of all cells exceed a surface temperature of 40 °C for 12th of June 1998 (Ma et al., 2002). Since the annual maximum of 3 m temperature at Everest site only amounts to 18.1 °C, the broadening of the deviation for the daytime test from +5 K to +20 K seems obvious. The deviation of the nighttime test has been broadened from -5 K to -10 K due to extremely low humidity, atmosphere constituents and catabatic winds. At this, measured values exceed the probability ranges only in late April 2006. In other respects, the outgoing longwave radiation dataset seems consistent.

   The net radiation (Figure 4-28) is slightly higher than at Namco site and according to its latitude agrees well with the field observations of GAME Tibet (Ma et al., 2005).

   Unlike the winter time, the soil heat flux shows a diurnal pattern from late March to November with a delay to the net radiation of about three to four hours, which is caused by the low heat conductivity of soil combined with the installation depth. In December 2005, the soil releases heat to the surface, whereas from February 2006 on, heat is again dumped from the surface to the soil indicating operability of the heat flux plate. Indeed, the simple parameterization approach of the soil heat flux as -10 % of the net radiation (Stull, 1988) is exceeded by the measurement However, the measurement stays in the range of $|200|$ Wm^{-2} as observed during the GAME Tibet project on the TP and can be physically alleged. Therefore the surface heat flux can be regarded as trustworthy.

4.2.1.2   Turbulent fluxes

In contrast to Namco site, sensible heat flux does not dominate the surface-atmosphere heat exchange. As for the monsoon, the most humid period (Figure 4-24), the cycle of the year (Figure 4-29) does not correspond to the net radiation measurement (Figure 4-28). The maxima in early spring agree with an overlapping period of little precipitation according to the Lhasa reference measurement, little melting water from the glacier due to low temperatures and the monsoon season not yet set in, therefore sparse evaporable water is available for the latent heat flux. In general, values ranging from -100 to +200 Wm^{-2}, as found at Namco site, have also been reported during the CAMP Tibet project (Ma et al., 2005).

   As for Everest site, the significance of the latent heat flux is uncertain, since it can not be assured that humidity fluctuations needed to derive the flux are measured properly. In general, latent heat flux dominates the surface-atmosphere heat exchange and rather than the sensible heat flux follows the net radiation measurement (Figure 4-28). This indicates sufficient water supply, which can be explained by the situation of the measurement in a braided river system. During monsoon season, additional moisture is supplied and the latent heat flux clearly outranges the sensible heat flux. Keeping the increasing sensible heat flux in mind, the latent heat flux shows a clear superelevation against the net radiation after February 2006, going along with the bias found in the humidity measurement (Figure 4-24). The LI-7500 offset before plus
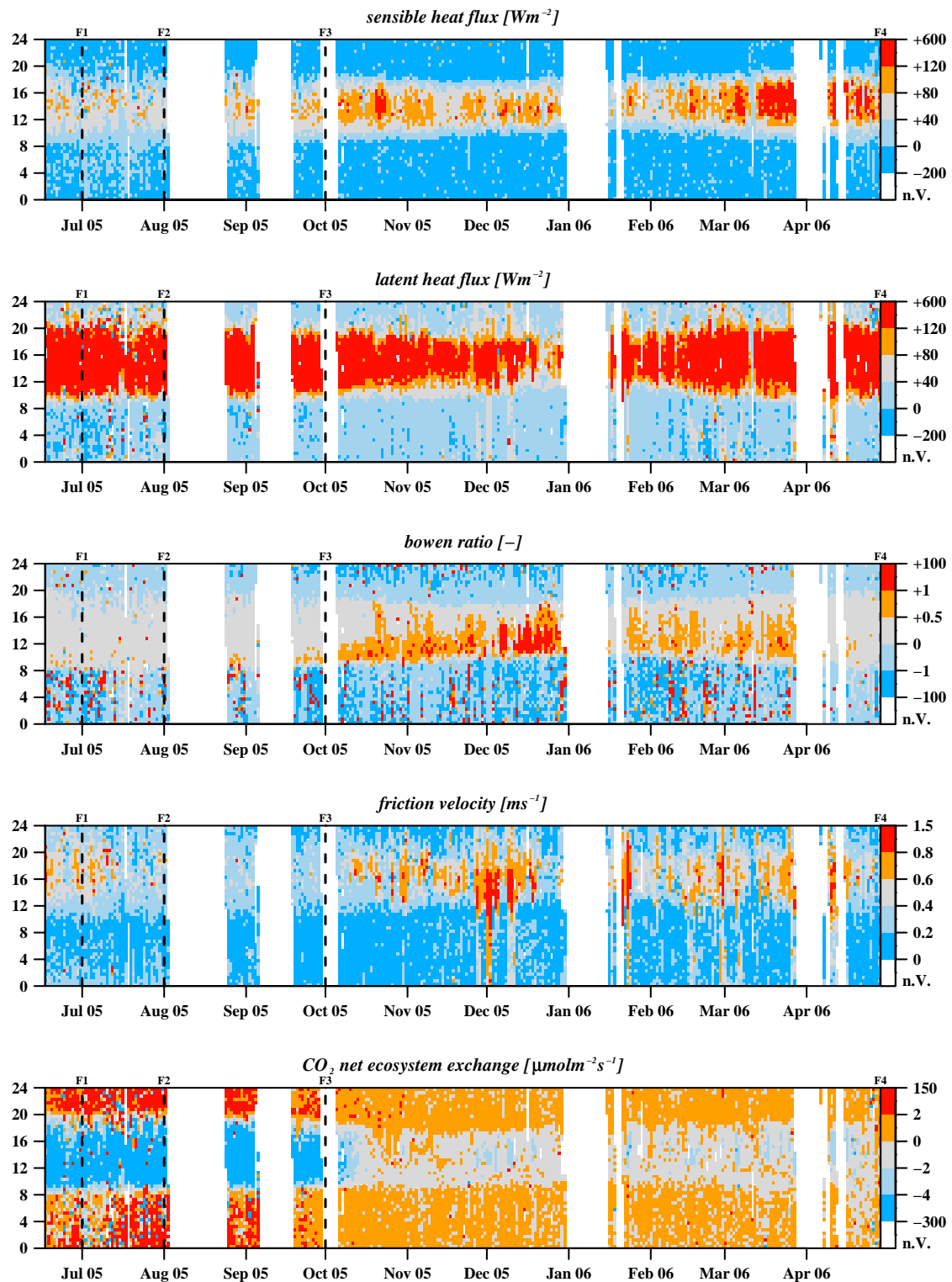
Figure 4-29: Sensible heat flux [Wm^{-2}], latent heat flux [Wm^{-2}], bowen ratio [-], friction velocity [ms^{-1}] and CO$_2$ NEE [µmolm^{-2}s^{-1}] for the entire measurement period. X-axis displays the day of the year, Y-axis displays the time of the day, and colors represent quantities according to the color bar attached respectively. Planar Fit Rotation periods are separated by solid lines, the beginning labeled with index 'R', each followed by the number of the period. Footprint periods are separated by dashed lines, the end labeled with index 'F', each followed by the number of the period.

additional bias after March 2006 legitimates the calculation of the latent heat flux only before March 2006. No precipitation data has yet been made available, but would greatly supplement this evaluation.

The calculation of the Bowen ratio highlights the findings as addressed above. In general, Everest site shows same annual characteristics but a little earlier than Namco site and at a more humid scale. The diurnal cycle displays a narrower window for daytime patterns due to the surrounding mountain crests. Daytime Bowen ratio reflects environmental conditions typical for grassland (Bo≈0.5) with a dryer winter period (Stull, 1988). Negative values point at the oasis effect taking place in the early evening and dew formation in the early morning.

Friction velocity bears analogy to the horizontal wind speed (Figure 4-23) with high values in daytime and shallow breeze at night, displaying a higher contrast than at Namco site which can be explained due to the mountain valley wind regime. The surface layer kinetic energy reaches its maximum in wintertime, not reaching as many high values as Namco site which results of the non free fetch conditions as compared to Namco site.

With an annual NEE of -150.2 gCm^{-2}, Everest site matches Namco site. Unlike the latter, the major CO_2 uptake period concentrates on the monsoon period providing sufficient photosynthetic active radiation and precipitation. Therefore plants do not have to bear any water stress. CO_2 uptake takes place from around 08:00 to 19:00 (BST) and CO_2 release from around 20:00 to 08:00 (BST). During other times of the year, the diurnal pattern persists, but CO_2 release balances CO_2 uptake. In general, the annual pattern and diurnal magnitude better corresponds earlier studies (Zhao et al., 2006) than Namco site. Thereby characteristic patterns are major CO_2 uptake from mid May to mid October and no high fluxes before end of April. But for a clearer filing, values for May and June are necessary to be conducted.

4.2.1.3 Energy balance

Unlike the jumpy residuum found at Namco site (Figure 4-8), the residuum at Everest site displays a clear diurnal and annual pattern (Figure 4-30) more or less following the net radiation (Figure 4-28), whereas the increasing bias in humidity measurement is visible at the end of time series. The diurnal pattern shows three bands, band 1 from midnight to 10:00 with nearly closed energy balance in summer and values down to -150 Wm^{-2} in winter, band 2 from 10:00 to 17:00 with values exceeding +150 Wm^{-2} all around the year and band 3 thereafter with values undercutting -150 Wm^{-2}. Considering the delay in soil heat flux (Figure 4-28), the residuum of band 3 seems to be triggered by the soil heat flux. Assuming superimposition of band 3 over band 2, energy balance would be nearly closed in summertime. The non annullable daytime residuum in winter coincides with low soil heat flux. This might be explainable by the small daytime penetration depth of net radiation into the soil and consequently unregistered heat storage above the installation depth of heat flux plate.
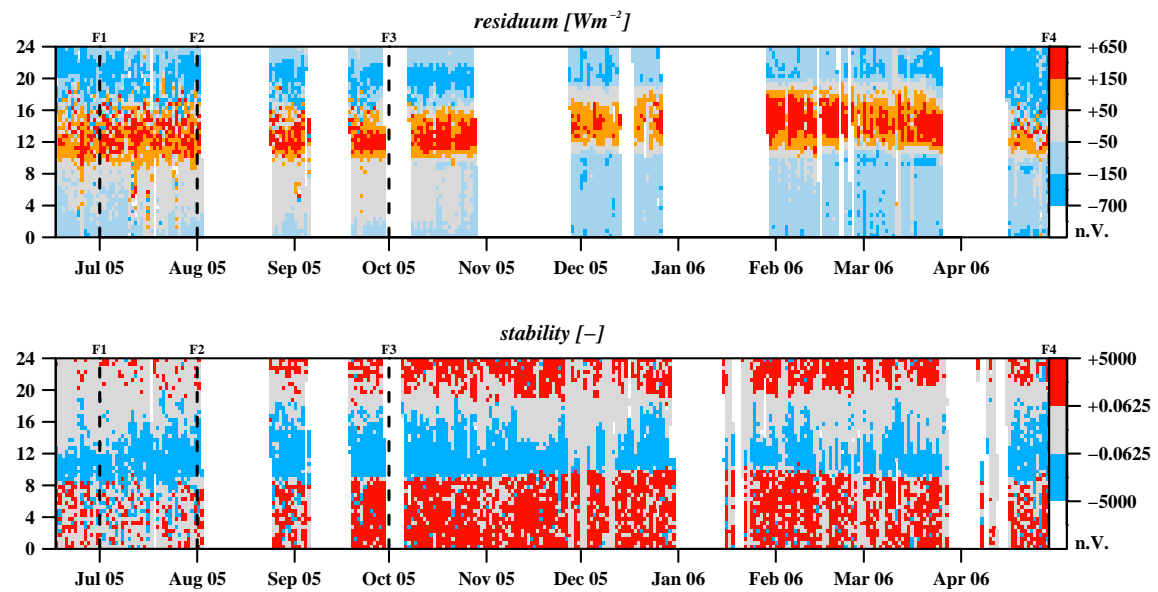
Figure 4-30: Residuum [Wm⁻²] and stability [-] for the entire measurement period. X-axis displays the day of the year, Y-axis displays the time of the day, and colors represent quantities according to the color bar attached respectively. Planar Fit Rotation periods are separated by solid lines, the beginning labeled with index 'R', each followed by the number of the period. Footprint periods are separated by dashed lines, the end labeled with index 'F', each followed by the number of the period.

Stability displays a continuous circle of the year with stable stratification at night and first labile to neutral stratification at daytime. The measurement period splits up in 24.3 % unstable, 45.3 % neutral and 30.5 % stable cases, with its most stable period in winter, most neutral cases in early summer and most unstable cases in late summer (Table 4-3).

As contrasted with Namco station, the transition from labile over neutral to stable stratification, which coincides with the initiation of the catabatic wind (Chapter 3.1.3.1) in the afternoon, is more distinct (Figure 4-30). Further, during monsoon season, stable stratification nearly diminishes and neutral stratification prevails at night. It can easily be seen that the consumption of turbulent energy by buoyancy (positive stability) at nighttime decreases because of isochronous relative maxima of friction velocity and the prevailing of latent heat flux over sensible heat flux (Figure 4-29).

Table 4-3: Distribution of stratification throughout the whole observation period (F_w) and within the footprint periods F1 – F4 [%].

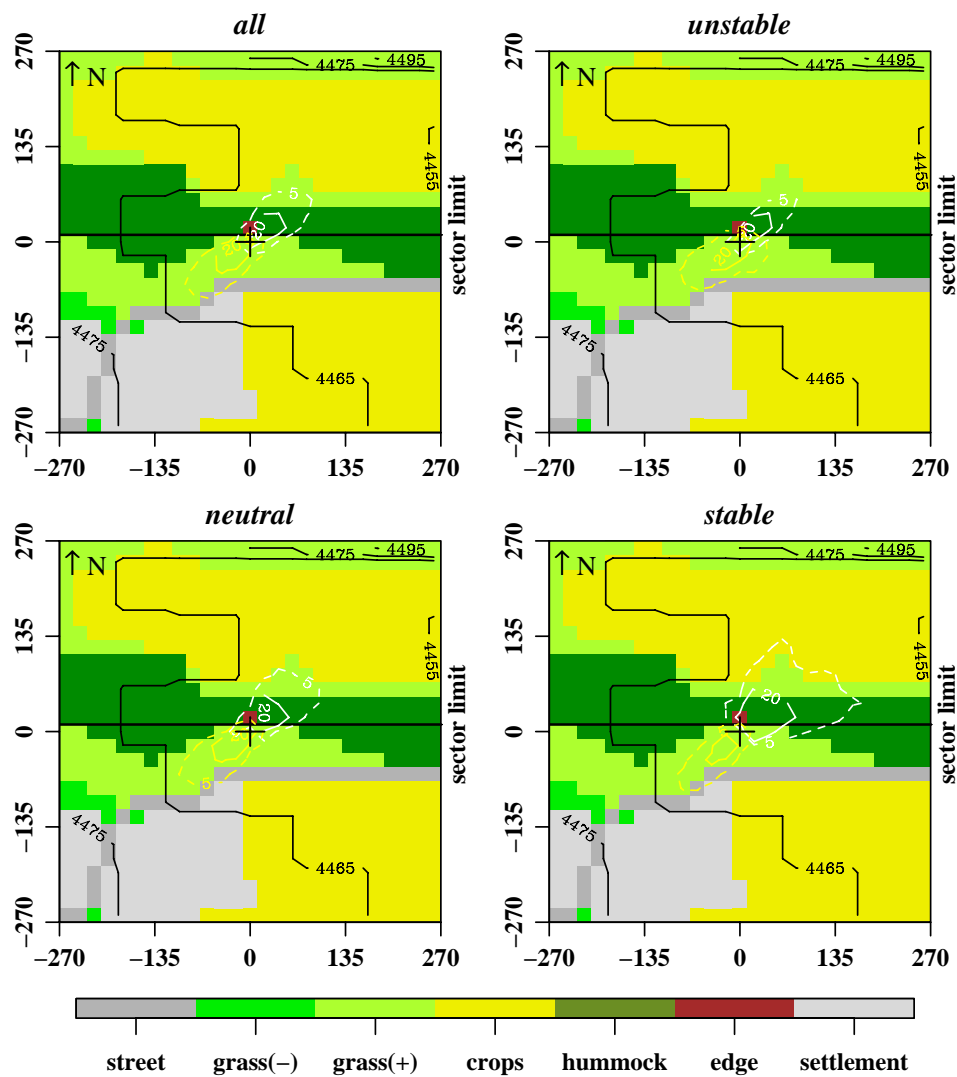| Footprint period	F_1	F_2	F_3	F_4	F_w
unstable	22.3	32.5	34.4	21.5	24.3
neutral	63.6	57.4	33.6	43.3	45.3
stable	14.1	10.1	32.0	35.3	30.5

Figure 4-31: Land use contribution according to stratification, scenario F_{w1}, as related to footprint climatology. The position of the flux measurement is indicated by the central cross-hairs. 5 land use classes are distinguished according to the color bar. The black horizontal line indicates the spatial limit for the independent analysis of northern and southern sector; black contour lines indicate the elevation a.s.l. [m]. Yellow and white contour lines display the 5% (dashed) and 20% (solid) effect level rings of the measurements, whereby yellow lines display the results for the southern, white lines for the northern sector.

4.2.2   Quality assessment

Based on the QA tools and, an assessment of land use contribution, vertical wind field and the spatial quality structures for the four fluxes under investigation is to be given.

4.2.2.1   Land use contribution

Agreeing with the dominating wind directions SW and NE, the central footprint is aligned along this corridor, with two centers corresponding to the articulate diurnal cycle of wind direction. Regarding the 0.4 m higher measurement height towards the N half space because of the adjoining edge prognosticating a larger footprint

compared to the S half space, the SW sector is in fact slightly dominating due to the temporal distribution (Figure 4-23). This fact also explains the extension of the footprint towards NE during stable conditions, though southwesterlies prevailing. As for the area covered by this measurement, multiplying the maximum E-W extension with the maximum north-south extension of the 5 % effect level ring yields the total area, so as to be comparable to the more omnidirectional Namco site. For Everest site, the total area for all stratifications amounts from 2.88 ha for F4 to 4.7 ha for F1 with an average of 3.6 ha for scenario F_{w1}. From Figure 4-31 can be seen, that the central footprint mainly covers the land use of type grass(-) and hummock. Under all stratifications slight influences of the road in the S part and especially during stable conditions contributions from the agriculture land is observed.

For the assessment of the land use contribution, land use type edge has been restored to the adjacent land use type hummock. At Everest site, land use types grass(+) and hummock dominate with an average contribution of 61.5 % and 22.8 % respectively, followed by street, settlement and crops with each ≈5 % contribution to the measurement (Figure 4-32). Maximum average contributions are achieved in F4 for type grass(+) with 68.9 % and in F1, F2 for type hummocks with more than 46 % contribution. Type crops contributes with a maximum of 9.3 % in F2, whereas street and settlement never surpass 7 % contribution (F4) and type grass(-) has a minor part with 1.3 % contribution (F4) at maximum.

As to create the target land cover type grassland, land use types grass(+), hummock and grass(-) have been recombined, so as to contrasted them against crops, street and
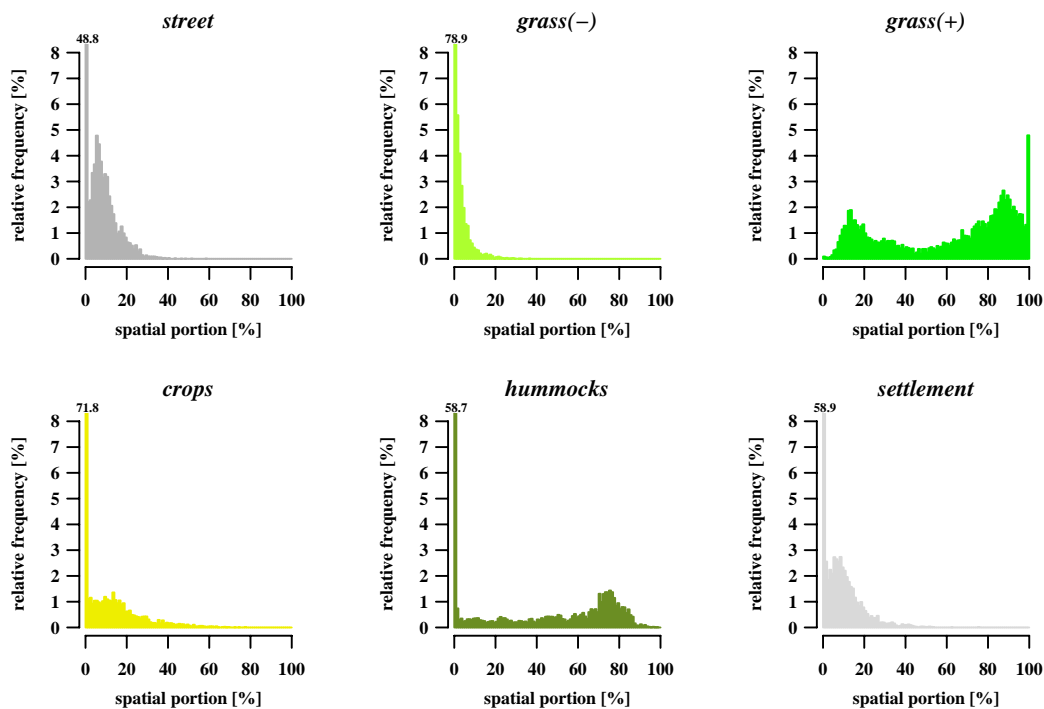

Figure 4-32: Frequency of spatial contribution for land use types as indicated for scenario F_{w1}.

settlement. At this, introduced a threshold of 80 % of spatial contribution for the target land coverage type attesting data representativity (Göckede et al., 2004), in average 85.4 % of all measurements surpass this threshold with a maximum of 89.4 % in F1 and a minimum of 84.3 % in F4.

4.2.2.2   Vertical wind

Measurements at the Everest site exceed the thresholds of $|0.35\text{ ms}^{-1}|$ and $|0.15\text{ ms}^{-1}|$ for 25.8 % and 55.3 % of the unrotated vertical wind speed half hour mean values (Figure 4-33). Downwind represents the biggest share of values exceeding the threshold of $|0.35\text{ ms}^{-1}|$, mainly in the evening hours in non-monsoon season coinciding with southwesterlies (Figure 4-23). On the other hand, upwind mainly prevails during monsoon season, synchronized with aggrandized northeasterlies. Since this states a clear dependence on up-/ downwind on facing wind sectors, only one Planar Fit Rotation for the entire measurement period could significantly reduce vertical wind speed values exceeding forenamed thresholds to 0.3 % and 3.6 %
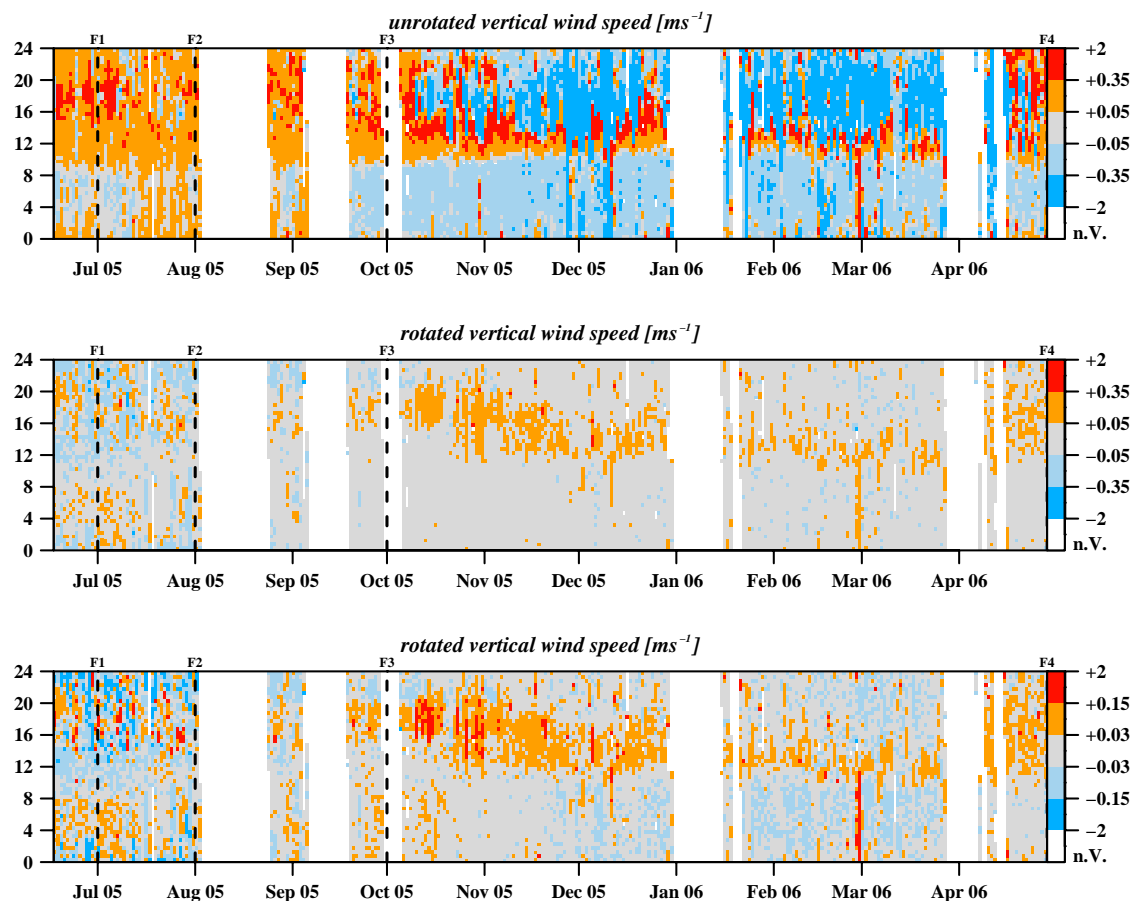

Figure 4-33: Unrotated and rotated vertical wind speed $[\text{ms}^{-1}]$ in two classifications. X-axis displays the day of the year, Y-axis displays the time of the day, and colors represent quantities according to the color bar attached. Planar Fit Rotation periods are separated by solid lines, the beginning labeled with index 'R', each followed by the number of the period. Footprint periods are separated by dashed lines, the end labeled with index 'F', each followed by the number of the period.
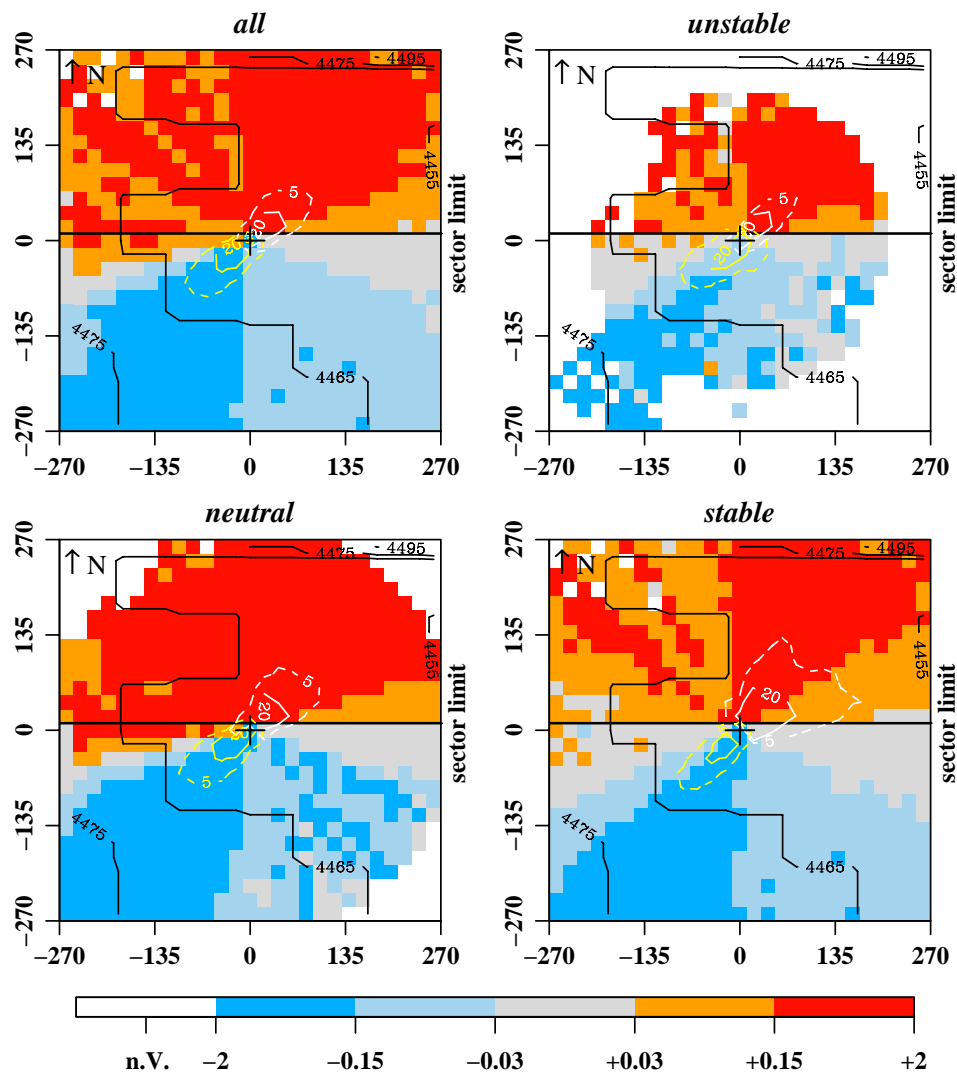
Figure 4-34: Spatial distribution of the median vertical wind speed before Planar Fit Rotation according to stratification, scenario F_{w1}, as related to footprint climatology. The position of the flux measurement is indicated by the central cross-hairs. 5 wind speed classes are distinguished according to the color bar; n.V. indicates that no datasets were available for the matching cell. The black horizontal line indicates the spatial limit for the independent analysis of northern and southern sector; black contour lines indicate the elevation a.s.l. [m]. Yellow and white contour lines display the 5% (dashed) and 20% (solid) effect level rings of the measurements, whereby yellow lines display the results for the S, white lines for the N sector.

respectively. Hereat values within ranges of $|0.05$ ms$^{-1}|$ and $|0.03$ ms$^{-1}|$ even increased from 28.6 % and 25.2 % to 81.4 % and 64.5 % respectively.

Since the dependence of vertical wind direction and intensity on the diurnal and annual cycle of wind direction could be clearly revealed above, the depictions of its spatial assessment will concentrate on the footprint scenario F_{w1} (Figure 4-34). As found in a preliminary study (Metzger et al., 2006), which only covered part of F4, upwind exceeding the median threshold of $|0.15$ ms$^{-1}|$ is throughout the year approaching from NE where a steep slope is located within the extended footprint

(300 m). The anabatic wind, according to topography deriving from E-NE directions is deflected here. As a consequence of the created pressure, the air is expanding not only horizontally but vertically as well, which leads to an upward tendency. This tendency is intensified by a small edge of 40 cm height that elevates the measurement against the surface in N. Downward air movement is mainly restricted to the SW sector and few occurrences in the SE. It can be attributed to the catabatic wind in general and glacier wind in the evening hours in particular, moving down the more gentle slope on the SW of the tower on a large stretch. This pattern is restricted to non-monsoon season (F), but immanent in such way that it can be traced in footprint
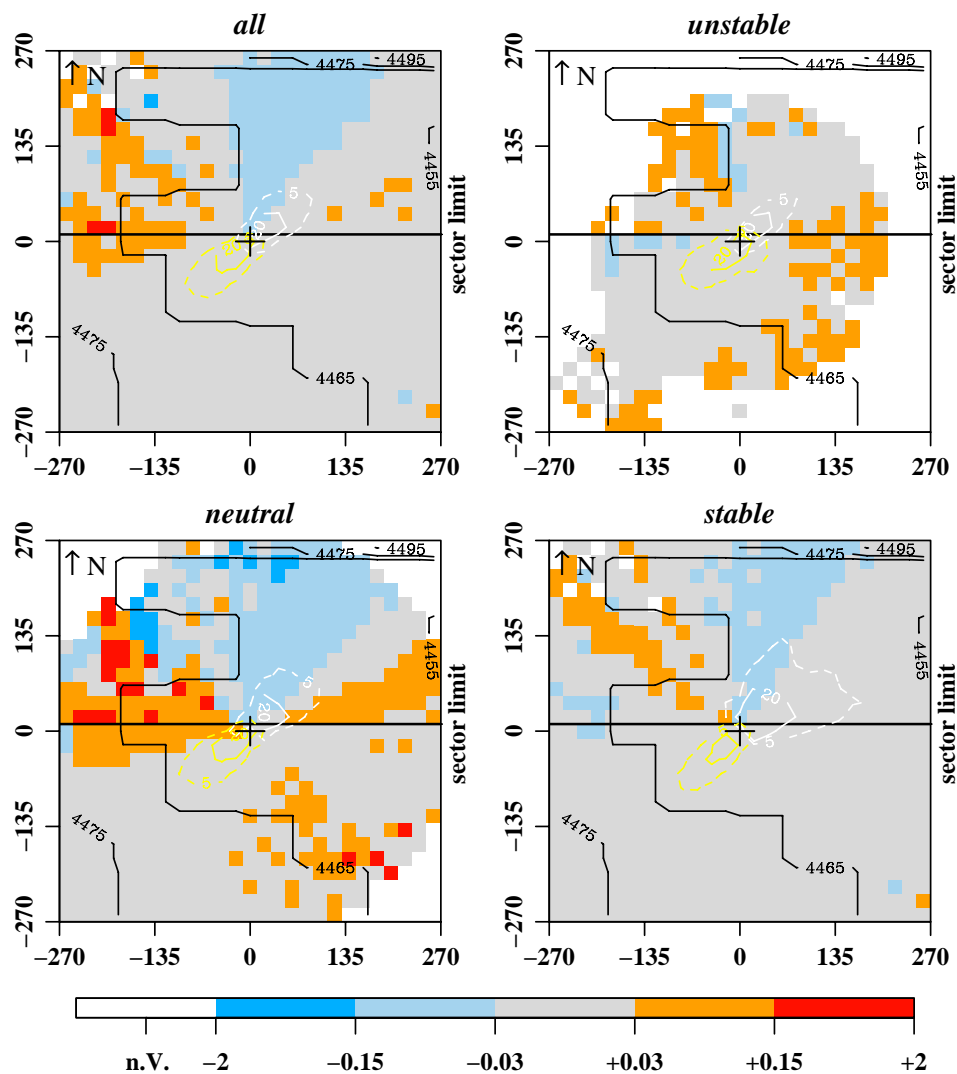

Figure 4-35: Spatial distribution of the median vertical wind speed after Planar Fit Rotation according to stratification, scenario F_{w1}, as related to footprint climatology. The position of the flux measurement is indicated by the central cross-hairs. 5 wind speed classes are distinguished according to the color bar; n.V. indicates that no datasets were available for the matching cell. The black horizontal line indicates the spatial limit for the independent analysis of northern and southern sector; black contour lines indicate the elevation a.s.l. [m]. Yellow and white contour lines display the 5% (dashed) and 20% (solid) effect level rings of the measurements, whereby yellow lines display the results for the S, white lines for the N sector.

scenario F_{w1}. It directly effects the measurement located on a slightly towards NE declined plane (Figure 3-1). In the contrary, local topography effects can not account for non-zero vertical wind values on the NW-SE stretch, as particularly evident under neutral stratification and found throughout the year. No sensor or mounting stand induced flow distortion can be ascertained from the unrotated wind field.

Coordinate rotation generally leads to a leveling of the wind field in the S sector and muted reversal of vertical wind field in NE, the latter mainly during unstable cases (Figure 4-35). However, especially during the monsoon period (F1, F2) the wind field displays a whole SSE half space with upwind values beyond $|0.03 \ ms^{-1}|$, in particular during neutral conditions. The vertical wind field in the SW-NE transect is slightly leveled, but eminently during neutral conditions still displays violations of the
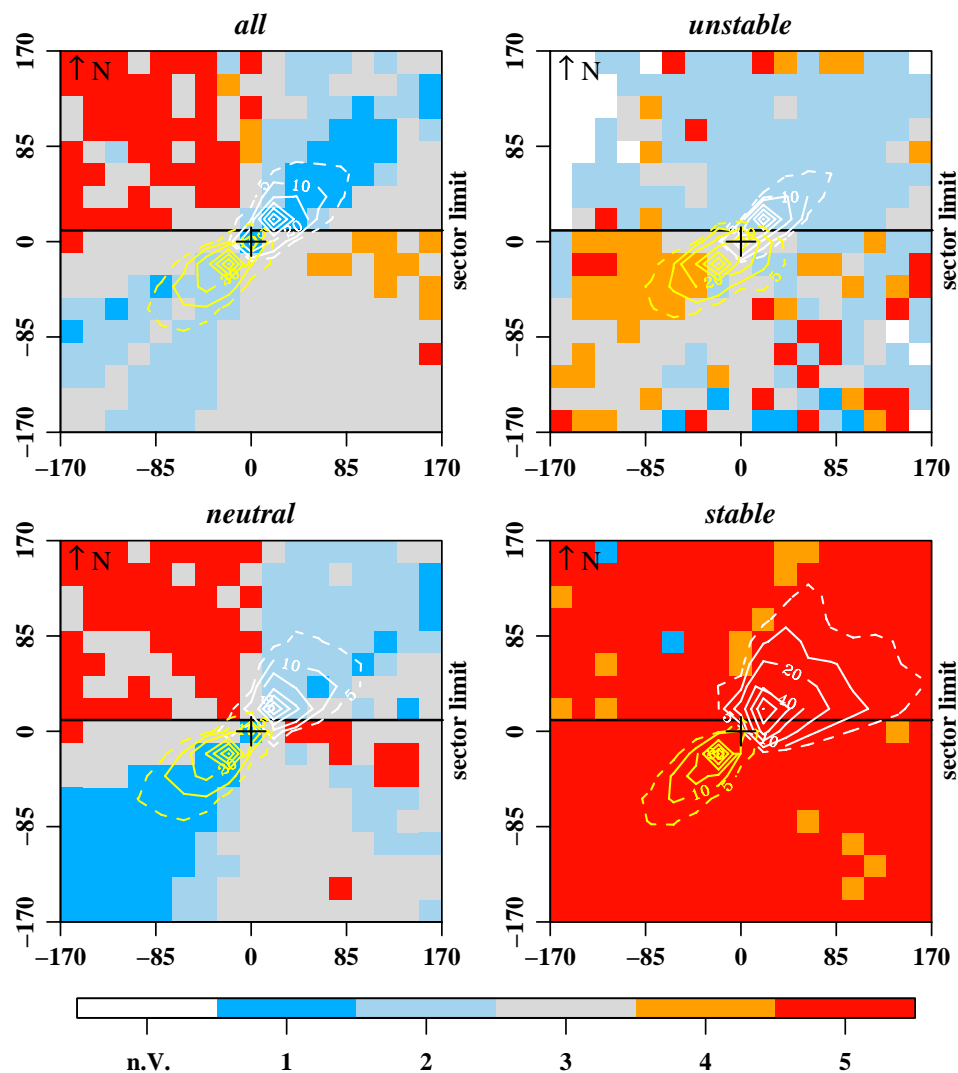

Figure 4-36: Quality rating for the sensible heat flux according to stratification, scenario F_{w1}, as related to footprint climatology. The position of the flux measurement is indicated by the central cross-hairs. 5 quality classes are distinguished according to the color bar; n.V. indicates that no datasets were available for the matching cell. Black contour lines indicate the elevation a.s.l. [m]; white contour lines display the 5% (dashed) and 10%, 20%, 40%, 60%, 80%, 100% (solid) effect level rings of the measurement.

threshold of |0.35 ms^{-1}|, principally stemming from the non-monsoon season F4. Because of the different flow characteristics, the introduction of monsoon- / non-monsoon- rotation periods could further nullify the vertical wind field.

4.2.2.3 Sensible heat flux

Neglecting the ITC for temperature, the central footprint is mainly rated 1 or 2 for all stratifications (Figure 4-36), whereas the measurement position itself is rated 1. These patterns remain throughout all footprint periods. The NE-SW corridor is thoroughly rated comparatively well, whereas temperature ITC with up to 30 ‰ displays a remarkable contribution to a slight degrading in the extended footprint in NE under unstable stratification (Figure 4-38). Further, the quality decreases in the extended

Figure 4-37: Spatial distribution for the median of stationarity according to vertical wind ITC classes for the sensible heat flux over the whole observation period for different stratification regimes. 9 quality classes are distinguished according to the Y-axis and the color bar; n.V. indicates that no datasets were available for the matching cell. Contour lines display the relative measurement density in 0.1 (dashed, black) and 0.5, 1, 5, 10, 20, 30, 40 (solid, white) ‰.
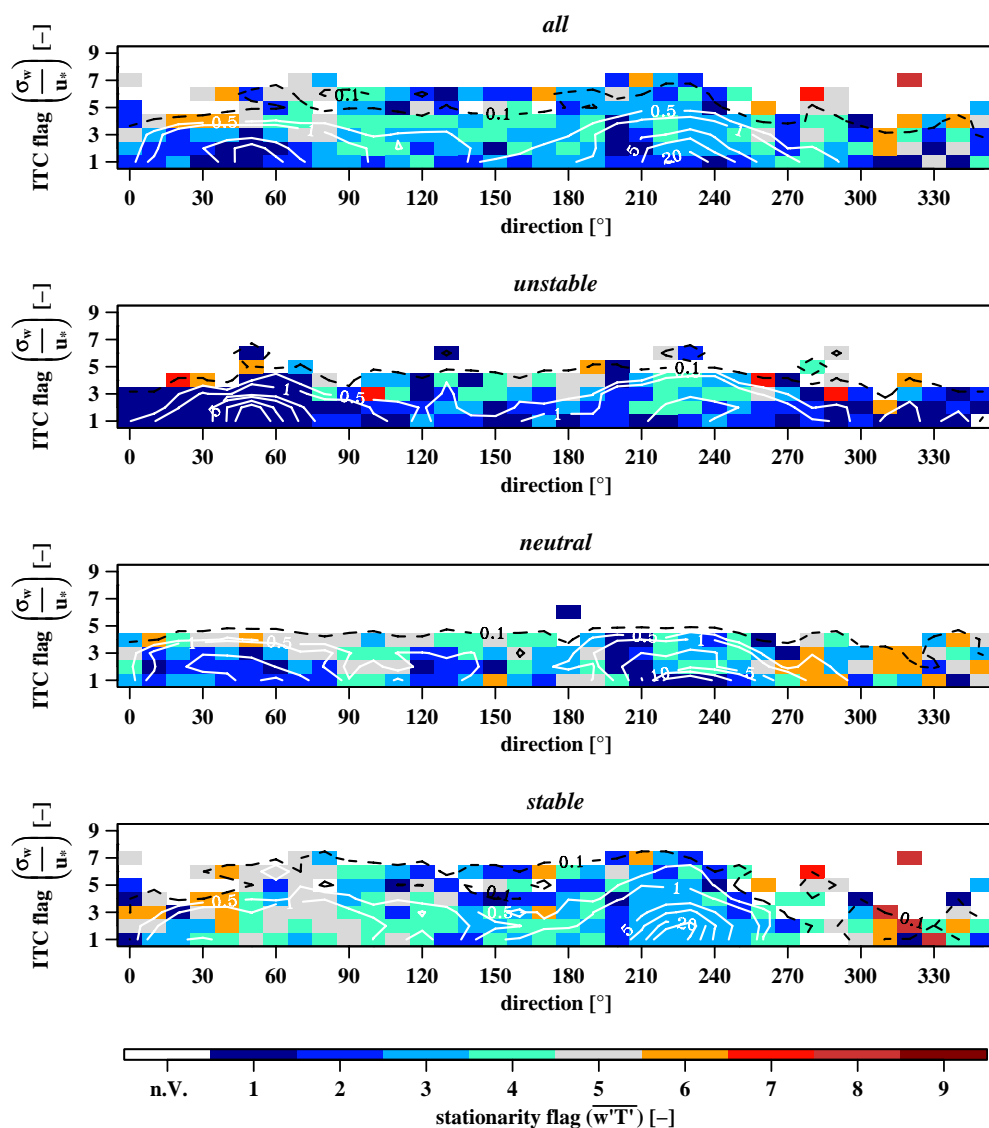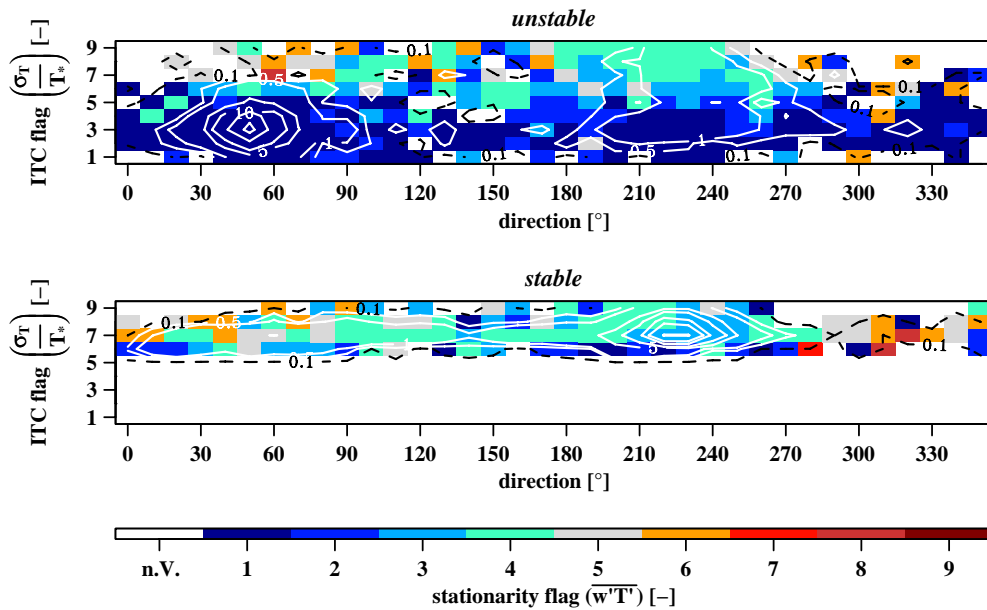
Figure 4-38: Spatial distribution for the median of stationarity according to temperature ITC classes for the sensible heat flux over the whole observation period for different stratification regimes. 9 quality classes are distinguished according to the Y-axis and the color bar; n.V. indicates that no datasets were available for the matching cell. Contour lines display the relative measurement density in 0.1 (dashed, black) and 0.5, 1, 5, 10, 20, 30, 40 (solid, white) ‰.

footprint towards SE and particularly in the NW, here mainly originating from instationarity during neutral and stable cases, whereat relative contributions are as low as 0.1 ‰ under neutral stratification (Figure 4-36, Figure 4-37). All stratifications contribute to the decreased SE sector, whereas only under neutral conditions stationarity, but otherwise ITC for temperature would be crucial. Under stable conditions, with up to 40 ‰ relative contribution, temperature ITC displays a remarkable degrading for the measurements in the SW sector (Figure 4-38). Bad quality ratings in this sector solely stem from the non-monsoon season (F4), whereas measurements during monsoon season only show bad ratings for the reaming sectors due to both, ITC and stationarity. This might be explained by heat emission from the village in combination with slow catabatic winds at nighttime: Since the ITC are a test on the stochastic distribution of turbulence elements, the test must fail, if organized structures occur. In the present case, these organized structures might be thermal eddies induced by heat emission from the village.

4.2.2.4   Latent heat flux

Latent heat flux displays a nearly flawless rating of 1 in the central footprint (Figure 4-39), and is in average rated better than the sensible heat flux, in particular during stable conditions, whereby one must keep in mind, that for this case no ITC are formulated for humidity but for temperature. During monsoon season, the SW sector is rated slightly worse than average, whereas during non-monsoon season the NE
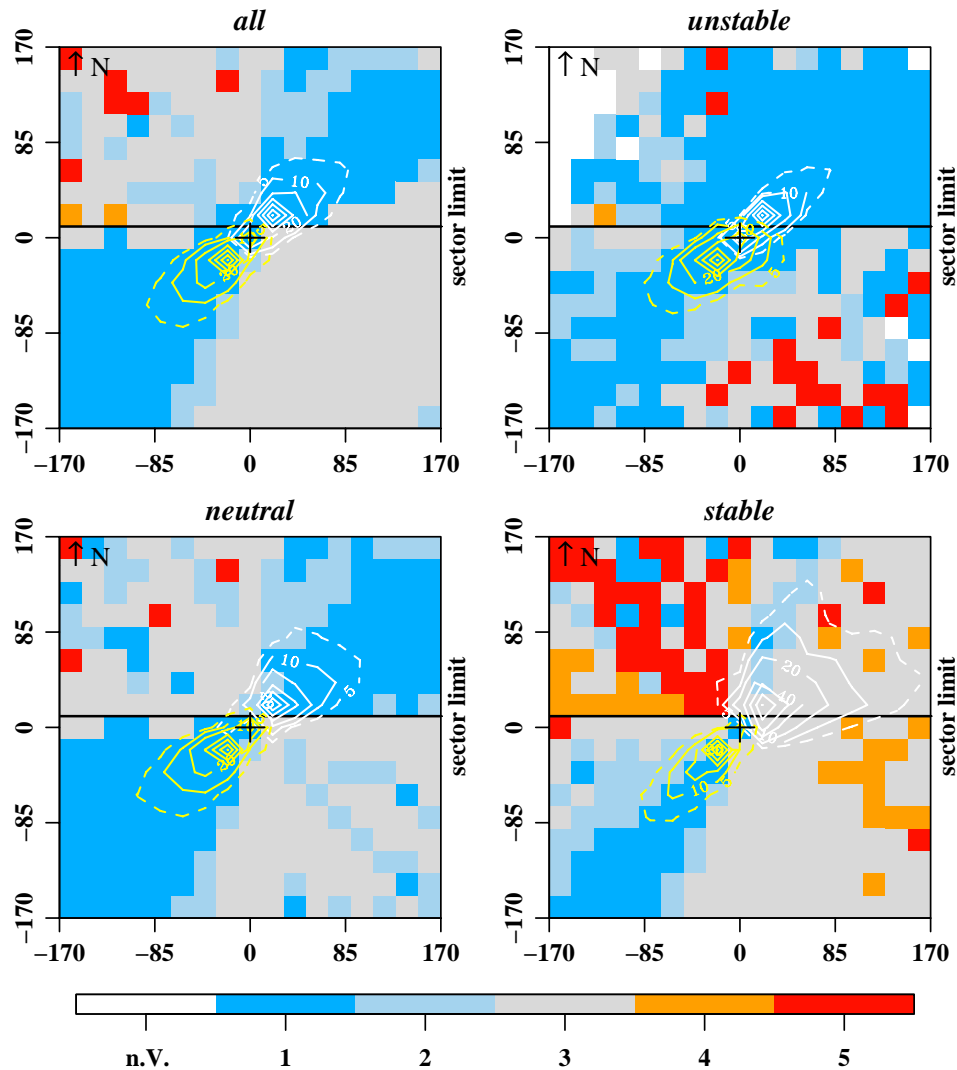
Figure 4-39: Quality rating for the latent heat flux according to stratification, scenario F_{w1}, as related to footprint climatology. The position of the flux measurement is indicated by the central cross-hairs. 5 quality classes are distinguished according to the color bar; n.V. indicates that no datasets were available for the matching cell. Black contour lines indicate the elevation a.s.l. [m]; white contour lines display the 5% (dashed) and 10%, 20%, 40%, 60%, 80%, 100% (solid) effect level rings of the measurement.

sector is degraded. As seen from the sensible heat flux, a transect of decreased quality ratings ranges from NW to SE, particularly pronounced during F1. As for the SE sector, mainly unstable conditions contribute due to the failure of stationarity. For the same reason the NW sector is downgraded under stable conditions which, despite low relative contribution, represents the main reason for a slight overall degrading.

4.2.2.5   Momentum flux

Momentum flux displays similar quality structures as the forenamed fluxes, but slightly worse ratings for the central footprint, which is in average 2 (Figure 4-40). Deteriorated sectors such as the NW-SE transect at Everest site are developed more homogenous than for sensible- and latent heat flux, as also seen at Namco site, here rated with 3 to 4. Also found for the other fluxes but noticeably pronounced for the
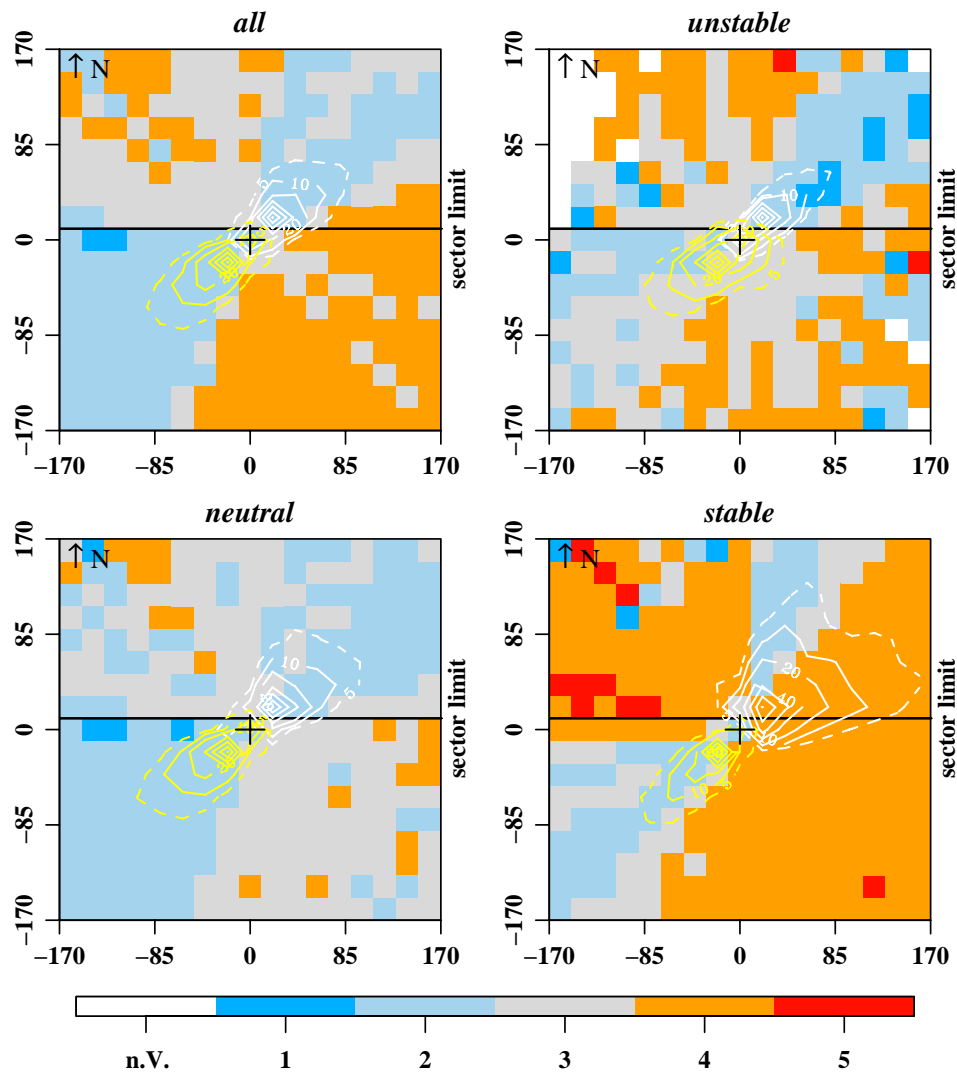
Figure 4-40: Quality rating for the momentum flux according to stratification, scenario F_{w1}, as related to footprint climatology. The position of the flux measurement is indicated by the central cross-hairs. 5 quality classes are distinguished according to the color bar; n.V. indicates that no datasets were available for the matching cell. Black contour lines indicate the elevation a.s.l. [m]; white contour lines display the 5% (dashed) and 10%, 20%, 40%, 60%, 80%, 100% (solid) effect level rings of the measurement.

momentum flux is the fact, that this transect barely received bad ratings during the monsoon season (F1-F3), but all the more in the non-monsoon season (F4). But contrary to the forenamed fluxes, not the stationarity criteria leads to a bad flagging of the transect under discussion, but rather the ITC for horizontal wind, in particular under stable stratification with relative contributions up to 1 ‰ (Figure 4-41). It can also be clearly seen, that more measurements contribute from the SE than from the NW sector. Furthermore, a contribution maximum of 5 ‰ is displayed for stable conditions around SE for ITC flag 6 (Figure 4-21).
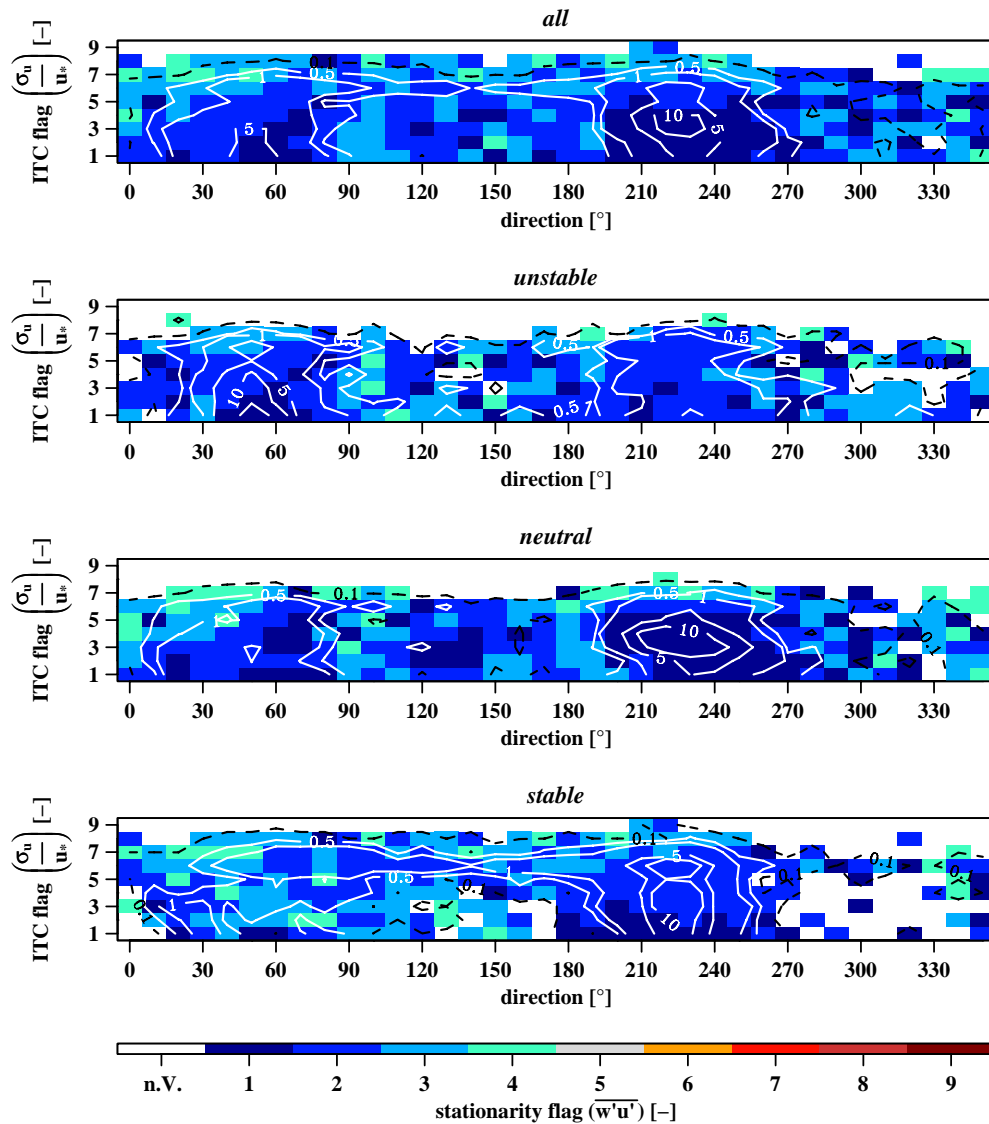
Figure 4-41: Spatial distribution for the median of stationarity according to horizontal wind ITC classes for the momentum flux over the whole observation period for different stratification regimes. 9 quality classes are distinguished according to the Y-axis and the color bar; n.V. indicates that no datasets were available for the matching cell. Contour lines display the relative measurement density in 0.1 (dashed, black) and 0.5, 1, 5, 10, 20, 30, 40 (solid, white) ‰.

4.2.2.6 CO_2 flux

Quality characteristics of the CO_2 flux are reminiscent to the sensible heat flux (Figure 4-36, Figure 4-42): The central footprint is mainly rated 1 and 2, whereat the NW sector in the extended footprint is rated as bad as 5 due to instationarity. As well, also the NE sector under stable stratification, not displaying impairment for momentum- and latent heat flux, is rated 5 due to instationarity (Figure 4-43). A possible explanation for this pattern, which can not be traced in the allover view, is that CO_2 coming past the sensor is concentrated in bubbles due to increased nighttime CO_2 release under incomplete developed turbulence. Such process is likely for the marshland in this sector and would lead to a failure of the stationarity criteria as
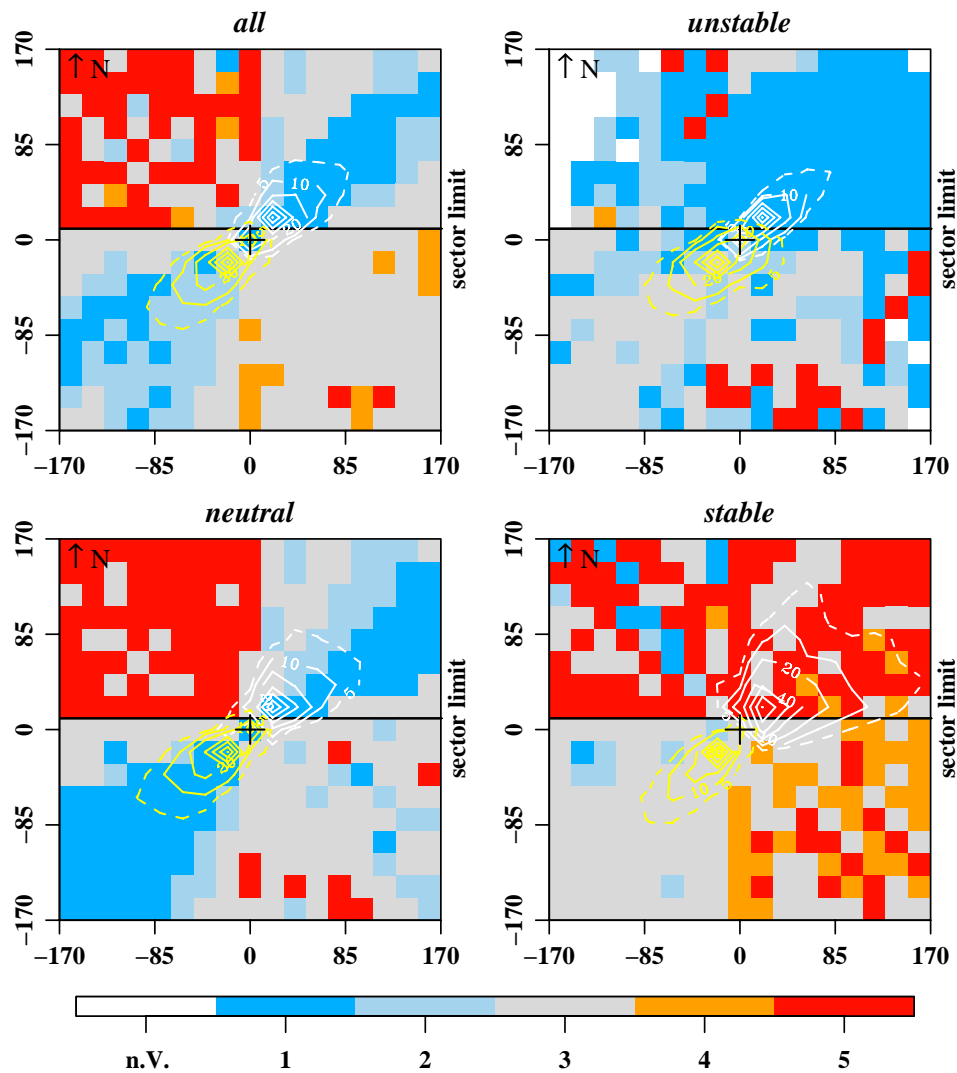
Figure 4-42: Quality rating for the CO_2 flux according to stratification, scenario F_{w1}, as related to footprint climatology. The position of the flux measurement is indicated by the central cross-hairs. 5 quality classes are distinguished according to the color bar; n.V. indicates that no datasets were available for the matching cell. Black contour lines indicate the elevation a.s.l. [m]; white contour lines display the 5% (dashed) and 10%, 20%, 40%, 60%, 80%, 100% (solid) effect level rings of the measurement.

applied in this study. Quality characteristics are quite constant in time, with the exception of only F4 contributing to the degraded ratings in the NW sector under stable stratification.

4.2.3   Comprehension

A clear distinction between monsoon- and non-monsoon periods can be attested from the meteorological variables under investigation. Thus the glacier wind in particular and anabatic / catabatic in general are only developed in non-monsoon season, whereas during monsoon season northeasterlies continue prevailing at night. This pattern overlaps with a transition from stable to neutral cases at night. As for the
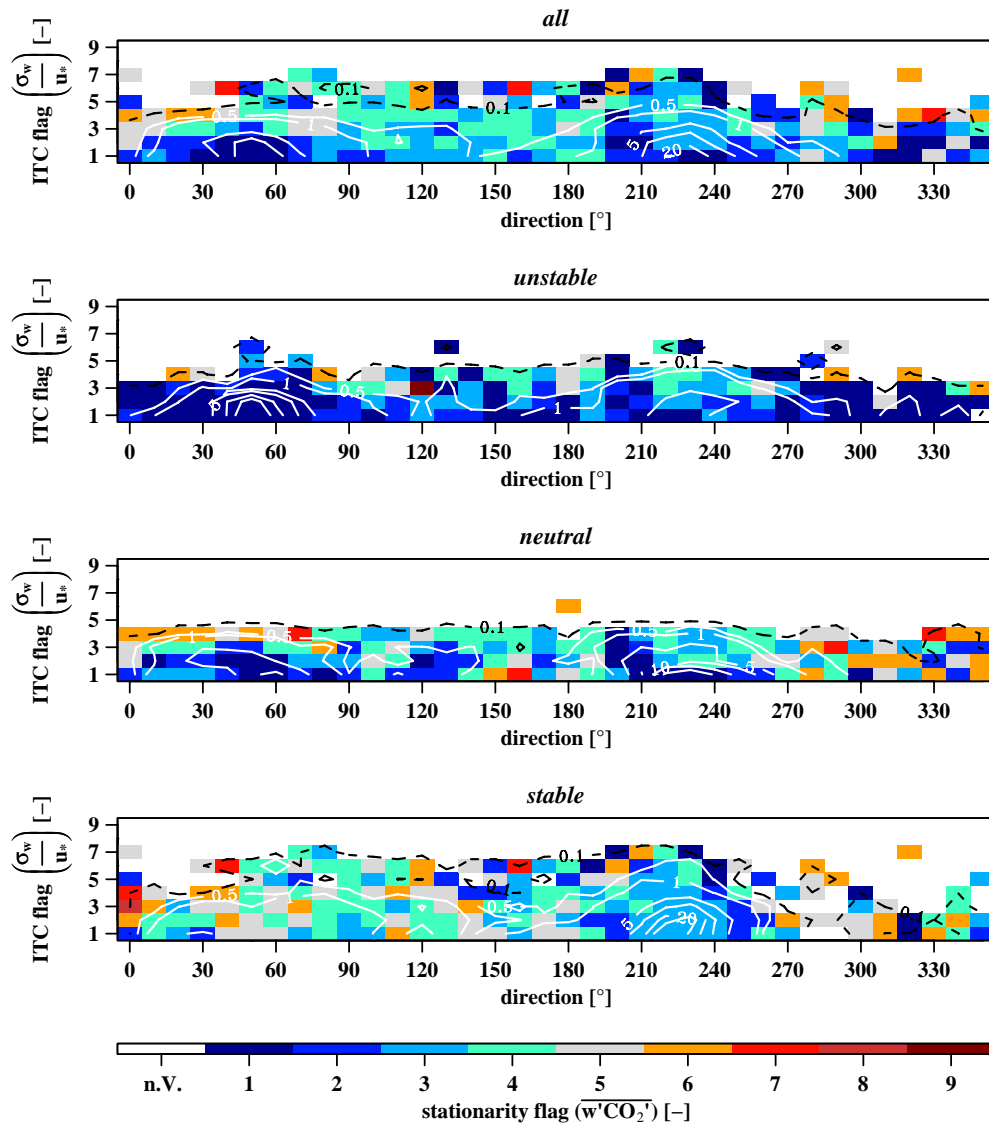
Figure 4-43: Spatial distribution for the median of stationarity according to vertical wind ITC classes for the CO_2 flux over the whole observation period for different stratification regimes. 9 quality classes are distinguished according to the Y-axis and the color bar; n.V. indicates that no datasets were available for the matching cell. Contour lines display the relative measurement density in 0.1 (dashed, black) and 0.5, 1, 5, 10, 20, 30, 40 (solid, white) ‰.

sufficient water supply due to the marshland, latent heat flux in general outreaches sensible heat flux. Minimum / maximum of sensible- /latent heat flux during monsoon season coincide with the annual maximum CO_2 uptake and the sensible heat flux reaches its maximum during the relatively dry pre-monsoon season.

As for land use contribution to the measurement, Everest site does not surpass the threshold 95 % for homogenous terrain as does Namco site. In particular influences of the farmland with up to 9.3 % contribution affect the measurement. In addition, a clear seasonal dependency of the interferences has been found, with more contributions of crops from NE during monsoon season (F1 – F3) and by settlement

Table 4-4: Distribution of measurement quality for the four different fluxes throughout the whole observation period and average station quality (Ø) over all fluxes.

Quality	Q_H	Q_E	u_*	Q_C	Ø
fundamental	54.8	55.0	44.0	44.6	49.6
long-term	24.3	14.9	32.0	18.6	22.5
discard	20.9	30.1	24.0	36.8	28.0

and street from SW during non-monsoon season, clearly conforming to the annual wind regime (Figure 4-23).

The topographical situation at Everest site must be regarded as relatively complicated, enforced by the situation of the measurement on a roughness step. Nevertheless vast sectors of up-/ downwind along the valleys inclination could be aligned satisfactorily due to the Planar Fit Rotation, solely aforesaid roughness step leads to non- annullable vertical winds in the central footprint. Else, no device or installation induced flow distortion could be detected.

Despite contributions of up to 6.4 % during F4, no major effect of the road or the village in the S half space of the measurement on the fluxes of sensible heat- and CO_2 has been detected, with exception of the sensible heat flux under stable stratification. In average, the central footprint is not rated worse than 3 for all of the fluxes. Consulting the interpretation of the quality flags as given in chapter 2.4.4, a statement on the average measurement quality can be given (Table 4-4). Best fluxes for fundamental research are the heat fluxes, whereat the sensible heat flux with 79.1 % utilizable half hour means is even more profitable for the calculation of monthly or annual sums of fluxes. With merely 63.2 % the CO_2 considerably falls behind, mainly due to contributions from NE under stable stratification (35.3 % of all cases during F4, Table 4-3), in particular during the non-monsoon period (F4).

Worse than average flags assigned for the extended footprint in a NW-SE transect are found provoked by instationarity. Hereat the NW sector was mainly compromised during neutral conditions which prevail in the afternoon. In particular the momentum flux, though here due to horizontal wind ITC, shows a dependency of bad ratings in this sector on the non-monsoon season and therewith on the glacier wind. Together with the SE sector, mainly degraded during unstable and stable conditions with no characteristic annual cycle, a corridor of compromised quality is formed. Since the vertical wind evaluation (Figure 4-34, Figure 4-35) shows disturbances for only part of the discussed transect and is even leveled for the SE sector after rotation, this pattern can not be solely accounted to local effects. Further, no instruments were aligned in these directions, which arises the question, whether e.g. a cross valley wind system is superimposed rectangular to the along valley wind system (Whiteman, 2000), causing organized structures that lead to failure of the QA tests.

5   Conclusions

Fluxes of sensible- and latent heat, momentum and CO_2 have been derived and interpreted for annual time series of Namco and Everest station employing EC technique. Hereat the QA procedure applied has proofed substantially necessary for both of the sites investigated. Optimum and disturbed fetch characteristics have been determined based on the analysis of the unrotated vertical wind component, as well as basic assumptions underlying the EC method have been checked for all fluxes investigated. An indication for possible reasons of compromised test results allows for the amendment of the measurement layout as well as it indicates the limits of EC measurement technique. In the following the key findings of this study will be lined out.

5.1   Annual time series of Namco and Everest station

The two sites investigated substantially differ in exposure, which has to be considered for an appropriate assessment. Whereas Namco site is situated on an open plain in central Tibet, Everest site is located in a pronounced valley 25 km N of the glacier edge near Mount Everest in S Tibet. As was expected due to the difference in exposure, the findings show monsoonal influence to be less evident at Namco site than at Everest site. However, measurement errors such as the misalignment of the sonic anemometer at Namco site affecting the time series of e.g. wind direction and vertical wind speed as well as the insufficiently accurate humidity measurement increase the peril to overlook a muted monsoonal influence.

Both sites display a diurnal cycle of wind direction that can at least be qualitatively related to landscape features, whereat Everest site is underlying changes in wind direction during the monsoon time. Both, high wind speeds and lower pressure prevail in winter, whereat humidity measurement throughout the year displays an offset at both sites and even a drift at Everest site after March 2005 that leads to a discard of the dataset and consecutively derived latent heat flux thereafter. The Radiation measurements in general could be confirmed, but the installation of the soil heat flux measurement at Namco site demands inspection. For Namco site, the sensible heat flux is the dominant heat transport mechanism, whereas at Everest site latent heat flux prevails following the monsoonal cycle. Such influence is probably also detectable for the latent heat flux at Namco site in September 2005, but not approvable since fluxes at comparatively high level are already reached in May, which is still pre-monsoon season. The CO_2 dynamics at Namco site increases earlier in the year and holds on longer than at Everest site, at which the maximum in dynamics is found in the monsoon season with comparatively higher uptake / release rates. However, annual estimates of NEE are alike and confirm that alpine meadows on the Tibet Plateau are small carbon sinks (Yu et al., 2006a). The Residuum at both sites amount to more than 30 % of the net radiation, but is barely assessable for Namco site because of falsified soil heat flux. At Namco site, neutral stratification is more dispersed

throughout the day, whereas at Everest site, with comparatively more stable cases, stability classes clearly correlate to the daytime.

5.2 Quality evaluation

Land use contribution analysis has revealed a high representativity of the Namco measurement for alpine grassland studies with an average target land use contribution of 95.8 %, whereas Everest site falls behind with 85.4 % on average.

Analysis of the unrotated vertical wind field for the Everest site has shown, that approximately 1/4 of the measurements do not fulfill the assumptions necessary for a physically correct processing of the data. This significantly decreases the overall representativity of the calculated fluxes and demands special caution in utilizing the results. Further, for all fluxes at both sites sectors underlying high flow-distortion were found. Measurement periods heavily affected by disturbed sectors only allow for the usage in continuously running measurement programs for obtaining monthly or annual sums of fluxes.

Keeping this in mind, the flux measurements at both sites fulfill the tests for ITC and stationarity to an extent that the results can be regarded as suitable for fundamental research for ≈50 % on average of the half hour means. At this point it must be recalled, that no ITC criteria can be applied to the measurements of CO_2 and H_2O, which consequently leads to a less stringent assessment of their flux quality.

5.3 Measures to improve the data quality

Problems with the pressure measurement have been found, manifested as jerky leaps in the time series. These compromise the calculated air densities and consequently the calculation of energy and air constituent fluxes by up to 4.4 %. Therefore, calibration and setup of the sensor must be revised to cut down uncertainties for the calculated fluxes.

Both sites had to struggle with humidity measurements, creating uncertainty for the derivation of the latent heat flux. Since a spike test has been carried out on the raw data of absolute humidity, a processing failure can be expelled; instead, calibration and maintenance reasons must be addressed. To avoid an offset for tiny water vapor measurements, the zero water must be very accurately set to zero due to the insensitivity of infrared hygrometers. Hereunto, a dry-gas cylinder should be used and additionally one or two desiccant tubes with Magnesium Perchlorate should be put in the path prior to the LI-7500 to really ensure that the air is dry. The water vapor tends to be very 'sticky' and can sometimes cling to the inside of the tubing and equipment for a long time. One should allow the zero, dry gas to flow through for at least 10 minutes (Johnson, 2007). In addition, calibrating at field conditions at the temperature and pressure to be observed will help eliminating any zero drift creating good specifications down to -25 °C: Zero drift can move the water vapor up to $\pm 0.05 \, mmolmol^{-1}K^{-1}$ caused by the LI-7500 internal electronics due to contracting/expanding from laboratory (indoor) to outside conditions. The LI-7500

uses 'ideal gas law' principles and additional calculations to make corrections necessary due to temperature changes and pressure changes in the gas measured through the LI-7500 open path. These principally allow the LI-7500 to output correct CO_2 and H_2O readings regardless of temperature/pressure changes. However, the internal electronics of the LI-7500 change uncharacteristically with temperature and can expand and / or contract quite uniquely and there is not a way to correct for this (Johnson, 2007). Moreover, the optical windows of the LI-7500 should be cleaned after each rainfall event or at least once a week. Contamination or dew formation on the windows can lead to a drift of the measurement signal (Mauder, 2007). Besides, the non cost-intensive installation of a capacitive hygrometer could assess the reliability of the infrared hygrometer due to correlation of the measurements. When the correlation is sufficiently high (i.e. near unity), the dynamic calibration works well (Tanaka et al., 2003), which would help to assess future problems. If the forenamed measures can not be carried out for logistics or organizational reasons or do not improve the measurement quality, there is still the more cost intensive alternative to install an ultra-violet hygrometer, which is more sensitive to low humidities but displays aging of the light source limiting the use period to about 1000 hours (Foken, 2006).

As for the calculation of plausibility ranges for the longwave radiation measurements, surface temperature as derived by an infrared thermometer would help to properly assess the outgoing longwave radiation, as would at least thermistor values of the pyrgeometer help to carry out this task conform to the test conditions.

At Namco site, the proper installation of the heat flux plate has to be examined, since the time series occasionally even displayed wrong sided mounting. Further, it has to be assured, that necessary corrections have been carried out and a different sensor type can be installed for checking purposes (Liebethal and Foken, 2006). As for the energy balance closure, the time delay of the soil heat flux due to installation depth of 10 cm and low heat conductivity of the soil should be deducted. Then it would be synchronized to the other energy balance components, which in case of Everest site could lead to a considerable improve.

Further, several improvements for the methodology of flux calculation and QA are conceivable. For instance device induced flow distortion, particularly at Namco site, has been revealed due to the vertical wind assessment, but without direct consequences on the quality rating. Rather should the sector from 255 ° to 15 ° be excluded for elementary research at this site. This task could - site specifically depending on the vertical wind assessment - be implemented in an allover flagging scheme together with stationarity, ITC and land use contribution (Foken, 2006). Regarding the footprint processing, it is advisable to integrate an accumulation mode for succession of roughness length in the circle of the year. Therewith the assumption of a scaling factor connecting the footprints of different roughness length parameterizations as valid for homogenous terrain would be obsolete, which would enable the calculation of more representative long term footprints also for

inhomogeneous sites as Everest with patchy differences in roughness length. Further, applying an unsupervised classification approach such as e.g. self organizing map, could lead to a more objective assessment of diurnal and annual patterns in the time series under investigation. Ultimately, the fluxes of this study could be calculated for different quality levels, so as to reveal the bias due to physical incorrect data processing and representativity of fragmentary datasets, which could be combined with an assessment of gap-filling techniques.

5.4 Outlook

Still, a few indications for both sites are unsolved. Such are the diurnal cycle of wind direction at Namco site as well as findings of transects with vertical wind directions contradicting local topography or bad quality ratings due to instationarity despite a flawless fetch. Regarding the complex terrain at both sites, this gives way to the hypothesis, that mesoscale flow patterns are superimposed to (Everest) or even dominate (Namco) the boundary layer circulation. As summarized for six European forest sites (Aubinet et al., 2005), the significance of advection depends critically on site topography and spatial source / sink heterogeneity, in particular during stable nighttime conditions. But considerably less information exists on the importance of advection for grassland (Hammerle et al., 2007). To further promote the flux measurement and research, accelerate data sharing and improve the data quality, it is necessary to present a methodological system of flux estimation and evaluation over complex terrain and to develop the integrated research that combines the flux measurement, stable isotope measurement, remote sensing observation and GIS technique combined with numerical modeling approaches (Yu et al., 2005). Such validations are partly carried out on the TP e.g. on ground-measured surface reflectance, surface temperature, net radiation, soil heat flux, sensible- and latent heat fluxes as compared to satellite derived values (Ma et al., 2006).

Still, our understanding of the vertical atmosphere structure above high alpine terrain, such as the dimension of boundary layer and its relation to supra regional circulation is limited, aggravated by local topography and glacier wind effects. Consequentially, findings derived from point measurements can not be simply upscaled in spatial and temporal manner. All the more, multi-instrument point measurements (WP, RASS, Radiosonde, EC) including cutting edge post field data processing routines as presented in this study can provide a high quality data basis corrected for violations of manifold assumptions brought along by the measurement techniques commonly in use.

Introducing upscaling approaches to these findings, so as to understand the water and energy cycle e.g. on scale of the TP, subjects as e.g. the quantitative understanding of channeled airflow in the vicinity of valley junctions are major challenges (Drobinski et al., 2006). Only under the requirement of a high quality data basis, large-eddy simulation such as the Advanced Regional Prediction System (Chow et al., 2006) is able to address this issue and further reveal e.g. local cross-valley

circulation, as hypothesized in this study (Weigel et al., 2006). Further, the application of e.g. a regional atmospheric model (Lu et al., 2005), run with detailed terrain data and tested against ground truth of high quality time series, can help to reveal the spatiotemporal dynamics and impact of atmospheric circulations in high alpine terrain. Therewith, an instrument for proper areal upscaling of energy and matter fluxes to the scale of the TP can be created and their effects on atmospheric circulation, carbon- and water cycle over China, Asia and the globe can be understood more accurate, only now allowing for the currently best possible formulations of sustainable management practices.

Acknowledgements

References

Amiro, B.D., 1998. Footprint climatologies for evapotranspiration in a boreal catchment. Agricultural and Forest Meteorology, 90: 195.

Asanuma, J., Ishikawa, H., Tamagawa, I., Ma, Y.M., Hayashi, T., Qi, Y.Q. and Wang, J.M., 2005. Application of the band-pass covariance technique to portable flux measurements over the Tibetan Plateau. Water Resources Research, 41.

Aubinet, M., Grelle, A., Ibrom, A., Rannik, U., Moncrieff, J., Foken, T., Kowalski, A.S., Martin, P.H., Berbigier, P., Bernhofer, C., Clement, R., Elbers, J., Granier, A., Grunwald, T., Morgenstern, K., Pilegaard, K., Rebmann, C., Snijders, W., Valentini, R. and Vesala, T., 2000. Estimates of the annual net carbon and water exchange of forests: The EUROFLUX methodology, Advances in Ecological Research, Vol 30. Advances in Ecological Research, pp. 113-175.

Aubinet, M., Berbigier, P., Bernhofer, C.H., Cescatti, A., Feigenwinter, C., Granier, A., Grunwald, T.H., Havrankova, K., Heinesch, B., Longdoz, B., Marcolla, B., Montagnani, L. and Sedlak, P., 2005. Comparing CO2 storage and advection conditions at night at different carboeuroflux sites. Boundary-Layer Meteorology, 116: 63-94.

Baldocchi, D., Falge, E., Gu, L.H., Olson, R., Hollinger, D., Running, S., Anthoni, P., Bernhofer, C., Davis, K., Evans, R., Fuentes, J., Goldstein, A., Katul, G., Law, B., Lee, X.H., Malhi, Y., Meyers, T., Munger, W., Oechel, W., Paw, U.K.T., Pilegaard, K., Schmid, H.P., Valentini, R., Verma, S. and Vesala, T., 2001. FLUXNET: A new tool to study the temporal and spatial variability of ecosystem-scale carbon dioxide, water vapor, and energy flux densities. Bull Amer Meteorol Soc, 82: 2415-2434.

Baldocchi, D.D., 2003. Assessing the eddy covariance technique for evaluating carbon dioxide exchange rates of ecosystems: past, present and future. Global Change Biology, 9: 479-492.

Barford, C.C., Wofsy, S.C., Goulden, M.L., Munger, J.W., Pyle, E.H., Urbanski, S.P., Hutyra, L., Saleska, S.R., Fitzjarrald, D. and Moore, K., 2001. Factors controlling long- and short-term sequestration of atmospheric CO2 in a mid-latitude forest. Science, 294: 1688-1691.

Bauer, S.J. and Raith, W., 1997. Erde und Planeten. de Gruyter, Berlin, XV, 727 pp.

Brach, E.J., Desjardins, R.L. and Stamour, G.T., 1981. Open Path Co2 Analyzer. Journal of Physics E-Scientific Instruments, 14: 1415-1419.

Central Intelligence Agency, U.S.A., 2001. China (political) map #802714. University of Texas Libraries, Austin.

Choi, T.J., Hong, J.Y., Kim, J., Lee, H.C., Asanuma, J., Ishikawa, H., Tsukamoto, O., Gao, Z.Q., Ma, Y.M., Ueno, K., Wang, J.M., Koike, T. and Yasunari, T., 2004. Turbulent exchange of heat, water vapor, and momentum over a Tibetan prairie by eddy covariance and flux variance measurements. Journal of Geophysical Research-Atmospheres, 109.

Chow, F.K., Weigel, A.P., Street, R.L., Rotach, M.W. and Xue, M., 2006. High-resolution large-eddy simulations of flow in a steep Alpine valley. Part I: Methodology, verification, and sensitivity experiments. Journal of Applied Meteorology and Climatology, 45: 63-86.

Curtis, P.S., Hanson, P.J., Bolstad, P., Barford, C., Randolph, J.C., Schmid, H.P. and Wilson, K.B., 2002. Biometric and eddy-covariance based estimates of annual carbon storage in five eastern North American deciduous forests. Agricultural and Forest Meteorology, 113: 3-19.

Drobinski, P., Bastin, S., Dusek, J., Zangl, G. and Flamant, P.H., 2006. Flow splitting at the bifurcation between two valleys: idealized simulations in comparison with Mesoscale Alpine Programme observations. Meteorology and Atmospheric Physics, 92: 285-306.

Ehman, J.L., Schmid, H.P., Grimmond, C.S.B., Randolph, J.C., Hanson, P.J., Wayson, C.A. and Cropley, F.D., 2002. An initial intercomparison of micrometeorological and ecological inventory estimates of carbon exchange in a mid-latitude deciduous forest. Global Change Biology, 8: 575-589.

Finnigan, J.J., Clement, R., Malhi, Y., Leuning, R. and Cleugh, H.A., 2003. A re-evaluation of long-term flux measurement techniques - Part I: Averaging and coordinate rotation. Boundary-Layer Meteorology, 107: 1-48.

Foken, T. and Wichura, B., 1996. Tools for quality assessment of surface-based flux measurements. Agricultural and Forest Meteorology, 78: 83-105.

Foken, T., Göckede, M., Mauder, M., Mahrt, L., Amiro, B. and Munger, W., 2004. Post-field data quality control. In: X. Lee, W. Massman and B. Law (Editors), Handbook of Micrometeorology: a Guide for Surface Flux Measurement and Analysis. Atmospheric and Oceanographic Sciences Library. Kluwer, Dordrecht, pp. 181-208.

Foken, T., 2006. Angewandte Meteorologie. Springer-Verlag, Heidelberg, 326 pp.

Fu, Y.L., Yu, G.R., Sun, X.M., Li, Y.N., Wen, X.F., Zhang, L.M., Li, Z.Q., Zhao, L. and Hao, Y.B., 2006. Depression of net ecosystem CO2 exchange in semi-arid Leymus chinensis steppe and alpine shrub. Agricultural and Forest Meteorology, 137: 234-244.

Fuehrer, P.L. and Friehe, C.A., 2002. Flux corrections revisited. Boundary-Layer Meteorology, 102: 415-457.

Gao, D., 1985. The glacier wind in the Rongbu Valley of Mt. Everest. Journal of Glaciology and Geocryology, 3: 249-256.

Gao, Y.X., Tang, M.C., Luo, S.W., Shen, Z.B. and Li, C., 1981. Some Aspects of Recent Research on the Qinghai-Xizang Plateau Meteorology. Bulletin of the American Meteorological Society, 62: 31-35.

Gao, Z.Q., Wang, J.M., Ma, Y.M., Kim, J., Choi, T.J., Lee, H.C., Asanuma, J. and Su, Z.B., 2000. Calculation of near-surface layer turbulent transport and analysis of surface thermal equilibrium features in Nagqu of Tibet. Physics and Chemistry of the Earth Part B-Hydrology Oceans and Atmosphere, 25: 135-139.

Gao, Z.Q., Bian, L.G., Wang, J.X. and Lu, L.G., 2003. Discussion on calculation methods of sensible heat flux during GAME/Tibet in 1998. Advances in Atmospheric Sciences, 20: 357-368.

Garrat, J.R., 1975. Limitations of the eddy correlation technique for determination of turbulent fluxes near the surface. Boundary Layer Meteorology, 8: 255-259.

Geiger, R., Aron, R. and Todhunter, P., 1995. The climate near the ground. Vieweg, Braunschweig, XVI, 528 pp.

Göckede, M., Rebmann, C. and Foken, T., 2004. A combination of quality assessment tools for eddy covariance measurements with footprint modelling for the characterisation of complex sites. Agricultural and Forest Meteorology, 127: 175-188.

Göckede, M., Markkanen, T., Hasager, C.B. and Foken, T., 2006. Update of a footprint-based approach for the characterisation of complex measuring sites. Boundary-Layer Meteorology, 118: 635-655.

Gu, L.H., Falge, E.M., Boden, T., Baldocchi, D.D., Black, T.A., Saleska, S.R., Suni, T., Verma, S.B., Vesala, T., Wofsy, S.C. and Xu, L.K., 2005a. Objective threshold determination for nighttime eddy flux filtering. Agricultural and Forest Meteorology, 128: 179-197.

Gu, S., Tang, Y.H., Du, M.Y., Kato, T., Li, Y.N., Cui, X.Y. and Zhao, X.A., 2003. Short-term variation of CO_2 flux in relation to environmental controls in an alpine meadow on the Qinghai-Tibetan Plateau. Journal of Geophysical Research-Atmospheres, 108.

Gu, S., Tang, Y., Du, M., Cui, X., Kato, T., Li, Y. and Zhao, X., 2005b. Effects of temperature on CO_2 exchange between the atmosphere and an alpine meadow. Phyton-Annales Rei Botanicae, 45: 361-370.

Gu, S., Tang, Y.H., Cui, X.Y., Kato, T., Du, M.Y., Li, Y.N. and Zhao, X.Q., 2005c. Energy exchange between the atmosphere and a meadow ecosystem on the Qinghai-Tibetan Plateau. Agricultural and Forest Meteorology, 129: 175-185.

Hammerle, A., Haslwanter, A., Schmitt, M., Bahn, M., Tappeiner, U., Cernusca, A. and Wohlfahrt, G., 2007. Eddy covariance measurements of carbon dioxide, latent and sensible energy fluxes above a meadow on a mountain slope. Boundary-Layer Meteorology, 122: 397-416.

Hirota, M., Tang, Y.H., Hu, Q.W., Hirata, S., Kato, T., Mo, W.H., Cao, G.M. and Mariko, S., 2006. Carbon dioxide dynamics and controls in a deep-water wetland on the Qinghai-Tibetan Plateau. Ecosystems, 9: 673-688.

Hu, H.P., Ye, B.S., Zhou, Y.H. and Tian, F.Q., 2006. A land surface model incorporated with soil freeze/thaw and its application in GAME/Tibet. Science in China Series D-Earth Sciences, 49: 1311-1322.

Huxman, T.E., Turnipseed, A.A., Sparks, J.P., Harley, P.C. and Monson, R.K., 2003. Temperature as a control over ecosystem CO2 fluxes in a high-elevation, subalpine forest. Oecologia, 134: 537-546.

Johnson, D., 2007. Personal Communication.

Jones, E.P., Ward, T.V. and Zwick, H.H., 1978. Fast Response Atmospheric Co2 Sensor for Eddy Correlation Flux Measurements. Atmospheric Environment, 12: 845-851.

Kaimal, J.C. and Wyngaard, J.C., 1990. The Kansas and Minnesota Experiments. Boundary-Layer Meteorology, 50: 31-47.

Kaimal, J.C. and Gaynor, J.E., 1991. Another Look at Sonic Thermometry. Boundary-Layer Meteorology, 56: 401-410.

Kato, T., Tang, Y.H., Gu, S., Cui, X.Y., Hirota, M., Du, M.Y., Li, Y.N., Zhao, Z.Q. and Oikawa, T., 2004a. Carbon dioxide exchange between the atmosphere and an alpine meadow ecosystem on the Qinghai-Tibetan Plateau, China. Agricultural and Forest Meteorology, 124: 121-134.

Kato, T., Tang, Y.H., Gu, S., Hirota, M., Cui, X.Y., Du, M.Y., Li, Y.N., Zhao, X.Q. and Oikawa, T., 2004b. Seasonal patterns of gross primary production and ecosystem respiration in an alpine meadow ecosystem on the Qinghai-Tibetan Plateau. Journal of Geophysical Research-Atmospheres, 109.

Kato, T., Tang, Y.H., Gu, S., Hirota, M., Du, M.Y., Li, Y.N. and Zhao, X.Q., 2006. Temperature and biomass influences on interannual changes in CO2 exchange in an alpine meadow on the Qinghai-Tibetan Plateau. Global Change Biology, 12: 1285-1298.

Köppen, W., 1931. Grundriss der Klimakunde. Walter de Gruyter, Berlin, 387 pp.

Li, M., Ma, Y.M., Ma, W., Hu, Z., Ishikawa, H., Su, Z. and Sun, F., 2006a. Analysis of turbulence characteristics over the northern Tibetan Plateau area. Advances in Atmospheric Sciences, 23: 579-585.

Li, Y.N., Sun, X.M., Zhao, X.Q., Zhao, L., Xu, S.X., Gu, S., Zhang, F.W. and Yu, G.R., 2006b. Seasonal variations and mechanism for environmental control of NEE of CO2 concerning the Potentilla fruticosa in alpine shrub meadow of Qinghai-Tibet Plateau. Science in China Series D-Earth Sciences, 49: 174-185.

Liebethal, C. and Foken, T., 2003. On the significance of the Webb correction to fluxes. Boundary-Layer Meteorology, 109: 99–106.

Liebethal, C. and Foken, T., 2004. On the significance of the Webb correction to fluxes. Corrigendum. Boundary-Layer Meteorology, 113: 301.

Liebethal, C. and Foken, T., 2006. On the use of two repeatedly heated sensors in the determination of physical soil parameters. Meteorologische Zeitschrift, 15: 293-299.

Lu, L., Denning, A.S., da Silva-Dias, M.A., da Silva-Dias, P., Longo, M., Freitas, S.R. and Saatchi, S., 2005. Mesoscale circulations and atmospheric CO2 variations in the Tapajo´s Region, Para´, Brazil. Journal of Geophysical Research, 110: 1-17.

Ma, Y.M., Su, Z.B., Li, Z.L., Koike, T. and Menenti, M., 2002. Determination of regional net radiation and soil heat flux over a heterogeneous landscape of the Tibetan Plateau. Hydrological Processes, 16: 2963-2971.

Ma, Y.M., Su, Z.B., Koike, T., Yao, T.D., Ishikawa, H., Ueno, K. and Menenti, M., 2003. On measuring and remote sensing surface energy partitioning over the Tibetan Plateau - from GAME/Tibet to CAMP/Tibet. Physics and Chemistry of the Earth, 28: 63-74.

Ma, Y.M., Fan, S., Ishikawa, H., Tsukamoto, O., Yao, T., Koike, T., Zuo, H., Hu, Z. and Su, Z., 2005. Diurnal and inter-monthly variation of land surface heat fluxes over the central Tibetan Plateau area. Theoretical and Applied Climatology, 80: 259-273.

Ma, Y.M., Zhong, L., Su, Z.B., Ishikawa, H., Menenti, M. and Koike, T., 2006. Determination of regional distributions and seasonal variations of land surface heat fluxes from Landsat-7 Enhanced Thematic Mapper data over the central Tibetan Plateau area. Journal of Geophysical Research-Atmospheres, 111.

Ma, Y.M., Yao, T., Ishikawa, H. and Koike, T., 2007. Study of land surface heat fluxes and water cycle over the Tibetan plateau. In: R. Baudo, G. Tartari, E. Vuillermoz and J.F. Shroder Jr. (Editors), Mountains: Witnesses of global changes. Developments in earth surface processes. Elsevier Science, London, pp. 315-330.

Massman, W.J. and Lee, X., 2002. Eddy covariance flux corrections and uncertainties in long-term studies of carbon and energy exchanges. Agricultural and Forest Meteorology, 113: 121-144.

Mauder, M. and Foken, T., 2004. Documentation and Instruction Manual of the Eddy Covariance Software Package TK2, Department of Micrometeorology, University of Bayreuth, Bayreuth.

Mauder, M., 2007. Personal Communication.

Metzger, S., Ma, Y.M., Markkanen, T., Göckede, M., Li, M. and Foken, T., 2006. Quality assessment of Tibetan Plateau Eddy Covariance measurements utilizing Footprint modeling. Advances in Earth Sciences, 21: 1260-1267.

Moore, C.J., 1986. Frequency response corrections for eddy correlation systems. Boundary-Layer Meteorology, 37: 17-35.

Obukhov, A.M., 1951. Investigation of the micro-structure of wind in the near surface layer of the atmosphere (in Russian). Izvestia AN SSSR, seria Geofizika, 3: 49-68.

Obukhov, A.M., 1960. O strukture temperaturnogo polja i polja skorostej v uslovijach konvekcii. AN SSSR, ser. Geofiz. Izv.: 1392–1396.

Ohtaki, E. and Matsui, T., 1982. Infrared Device for Simultaneous Measurement of Fluctuations of Atmospheric Carbon-Dioxide and Water-Vapor. Boundary-Layer Meteorology, 24: 109-119.

Paw, K.T., Baldocchi, D.D., Meyers, T.P. and Wilson, K.B., 2000. Correction of eddy-covariance measurements incorporating both advective effects and density fluxes. Boundary-Layer Meteorology, 97: 487-511.

Rannik, U., Markkanen, T., Raittila, J., Hari, P. and Vesala, T., 2003a. Turbulence statistics inside and over forest: Influence on footprint prediction. Boundary-Layer Meteorology, 109: 163-189.

Rannik, Ü., Aubinet, M., Kurbanmuradov, O., Sabelfeld, K.K., Markkanen, T. and Vesala, T., 2000. Footprint analysis for measurements over a heterogeneous forest. Boundary-Layer Meteorology, 97: 137-166.

Rannik, Ü., Markkanen, T., Raittila, J., Hari, P. and Vesala, T., 2003b. Turbulence statistics inside and over forest: Influence on footprint prediction. Boundary-Layer Meteorol. , 109: 163-189.

Rebmann, C., Göckede, M., Foken, T., Aubinet, M., Aurela, M., Berbigier, P., Bernhofer, C., Buchmann, N., Carrara, A., Cescatti, A., Ceulemans, R., Clement, R., Elbers, J.A., Granier, A., Grunwald, T., Guyon, D., Havrankova, K., Heinesch, B., Knohl, A., Laurila, T., Longdoz, B., Marcolla, B., Markkanen, T., Miglietta, F., Moncrieff, J., Montagnani, L., Moors, E., Nardino, M., Ourcival, J.M., Rambal, S., Rannik, Ü., Rotenberg, E., Sedlak, P., Unterhuber, G., Vesala, T. and Yakir, D., 2005. Quality analysis applied on eddy covariance measurements at complex forest sites using footprint modelling. Theoretical and Applied Climatology, 80: 121-141.

Reynolds, O., 1895. On the dynamical theory of incompressible viscous fluids and the determination of criterion. Philosophical Transactions of Royal Society of London, A174: 935–982.

Schmid, H.P., 1994. Source areas for scalars and scalar fluxes. Boundary- Layer Meteorology, 67: 293-318

Schotanus, P., Nieuwstadt, F.T.M. and De Bruin, H.A.R., 1983. Temperature measurement with a sonic anemometer and its application to heat and moisture fluctuations. Boundary-Layer Meteorology, 26: 81-93.

Scrase, F.J., 1930. Some Characteristics of Eddy Motion in the Atmosphere. Geophysical Memoirs 52. Meteorological Office, London, pp. 56.

Seibert, P., Beyrich, F., Gryning, S.E., Joffre, S., Rasmussen, A. and Tercier, P., 2000. Review and intercomparison of operational methods for the determination of the mixing height. Atmospheric Environment, 34: 1001-1027.

Shi, P.L., Sun, X.M., Xu, L.L., Zhang, X.Z., He, Y.T., Zhang, D.Q. and Yu, G.R., 2006. Net ecosystem CO_2 exchange and controlling factors in a steppe - Kobresia meadow on the Tibetan Plateau. Science in China Series D-Earth Sciences, 49: 207-218.

Sonntag, D., 1990. Important new values of the physical constants of 1986, vapour pressure formulations based on the ITS-90, and psychrometer formulae. Zeitschrift für Meteorologie, 40: 340-344.

Stull, R.B., 1988. An Introduction to Boundary Layer Meteorology. Atmospheric sciences library. Kluwer Academic Publishers, Dordrecht , Boston, London, 666 pp.

Sun, F., Ma, Y., Li, M., Ma, W., Tian, H. and Metzger, S., 2007. Boundary layer effects above a Himalayan valley. Geophysical Research Letters, accepted 2007-03.

Swinbank, W.C., 1951. The Measurement of Vertical Transfer of Heat and Water Vapor by Eddies in the Lower Atmosphere. Journal of Meteorology, 8: 135-145.

Tanaka, K., Ishikawa, H., Hayashi, T., Tamagawa, I. and Ma, Y.M., 2001. Surface energy budget at Amdo on the Tibetan Plateau using GAME/Tibet IOP98 data. Journal of the Meteorological Society of Japan, 79: 505-517.

Tanaka, K., Tamagawa, I., Ishikawa, H., Ma, Y.M. and Hu, Z.Y., 2003. Surface energy budget and closure of the eastern Tibetan Plateau during the GAME-Tibet IOP 1998. Journal of Hydrology, 283: 169-183.

Thomas, C. and Foken, T., 2002. Re-evaluation of integral turbulence characteristics and their parameterisations - 15th Conference on Turbulence and Boundary Layers, Wageningen, NL. Am. Meteorol. Soc.: pp. 129-132.

Thomson, D.J., 1987. Criteria for the selection of stochastic models of particle trajectories in turbulent flows J. Fluid Mech 180: 529-556

Trewartha, G.T. and Horn, L.H., 1980. An introduction to climate. McGraw-Hill, New York, 416 pp.

Troen, I. and Petersen, E.L., 1989. European Wind Atlas. Published for the Commission of the European Communities, Directorate General for Science, Research and Development (Brussels, Belgium) by Risö National Laboratory, Roskilde, Denmark, 240 pp.

Turnipseed, A.A., Anderson, D.E., Blanken, P.D., Baugh, W.M. and Monson, R.K., 2003. Airflows and turbulent flux measurements in mountainous terrain Part 1. Canopy and local effects. Agricultural and Forest Meteorology, 119: 1-21.

Turnipseed, A.A., Anderson, D.E., Burns, S., Blanken, P.D. and Monson, R.K., 2004. Airflows and turbulent flux measurements in mountainous terrain Part 2: Mesoscale effects. Agricultural and Forest Meteorology, 125: 187-205.

Vickers, D. and Mahrt, L., 1997. Quality control and flux sampling problems for tower and aircraft data. Journal of Atmospheric and Oceanic Technology, 14: 512-526.

Walter, H. and Lieth, H., 1960. Klimadiagramm-Weltatlas. Fischer, Jena, pp. [loose leaf edition].

Webb, E.K., Pearman, G.I. and Leuning, R., 1980. Correction of the flux measurements for density effects due to heat and water vapour transfer. Quarterly Journal of The Royal Meteorological Society, 106: 85-100.

Weigel, A.P., Chow, F.K., Rotach, M.W., Street, R.L. and Xue, M., 2006. High-resolution large-eddy simulations of flow in a steep Alpine valley. Part II: Flow structure and heat budgets. Journal of Applied Meteorology and Climatology, 45: 87-107.

Weischet, W. and Endlicher, W., 2000. Regionale Klimatologie Teil 2 Die Alte Welt, Europa, Afrika, Asien. Teubner, Stuttgart, 625 pp.

Whiteman, C.D., 2000. Mountain meteorology : fundamentals and applications. Oxford University Press, New York, 355 pp.

Wilczak, J.M., Oncley, S.P. and Stage, S.A., 2001. Sonic anemometer tilt correction algorithms. Boundary-Layer Meteorology, 99: 127-150.

Wilson, K., Goldstein, A., Falge, E., Aubinet, M., Baldocchi, D., Berbigier, P., Bernhofer, C., Ceulemans, R., Dolman, H., Field, C., Grelle, A., Ibrom, A., Law, B.E., Kowalski, A., Meyers, T., Moncrieff, J., Monson, R., Oechel, W., Tenhunen, J., Valentini, R. and Verma, S., 2002. Energy balance closure at FLUXNET sites. Agricultural and Forest Meteorology, 113: 223-243.

Wyngaard, J.C., Cote', O.R. and Izumi, Y., 1971. Local free convection, similarity and the budgets of shear stress and heat flux. J Atmos Sci, 28: 1171–1182.

Xu, L.L., Zhang, X.Z., Shi, P.L. and Yu, G.R., 2005a. Establishment of apparent quantum yield and maximum ecosystem assimilation on Tibetan Plateau alpine meadow ecosystem. Science in China Series D-Earth Sciences, 48: 141-147.

Xu, L.L., Zhang, X.Z., Shi, P.L. and Yu, G.R., 2006. Response of canopy quantum yield of alpine meadow to temperature under low atmospheric pressure on Tibetan Plateau. Science in China Series D-Earth Sciences, 49: 219-225.

Xu, S.X., Zhao, X.Q., Fu, Y.L., Zhao, L., Li, Y.N., Cao, G.M., Gu, S., Wang, Q.X. and Du, M.Y., 2005b. Characterizing CO_2 fluxes for growing and non-growing seasons in a shrub ecosystem on the Qinghai-Tibet Plateau. Science in China Series D-Earth Sciences, 48: 133-140.

Xu, S.X., Zhao, X.Q., Li, Y.N., Zhao, L., Yu, G.R., Sun, X.M. and Cao, G.M., 2005c. Diurnal and monthly variations of carbon dioxide flux in an alpine shrub on the Qinghai-Tibet Plateau. Chinese Science Bulletin, 50: 539-543.

Yanai, M.H., Li, C.F. and Song, Z.S., 1992. Seasonal Heating of the Tibetan Plateau and Its Effects on the Evolution of the Asian Summer Monsoon. Journal of the Meteorological Society of Japan, 70: 319-351.

Yang, K., Koike, T., Ishikawa, H. and Ma, Y.M., 2004. Analysis of the surface energy budget at a site of GAME/Tibet using a single-source model. Journal of the Meteorological Society of Japan, 82: 131-153.

Ye, D.Z., 1981. Some Characteristics of the Summer Circulation over the Qinghai-Xizang (Tibet) Plateau and Its Neighborhood. Bulletin of the American Meteorological Society, 62: 14-19.

Ye, D.Z. and Wu, G.X., 1998. The role of the heat source of the Tibetan Plateau in the general circulation. Meteorology and Atmospheric Physics, 67: 181-198.

Yu, G.R., Zhang, L.M., Sun, X.M., Fu, Y.L. and Li, Z.Q., 2005. Advances in carbon flux observation and research in Asia. Science in China Series D-Earth Sciences, 48: 1-16.

Yu, G.R., Fu, Y.L., Sun, X.M., Wen, X.F. and Zhang, L.M., 2006a. Recent progress and future directions of ChinaFLUX. Science in China Series D-Earth Sciences, 49: 1-23.

Yu, G.R., Wen, X.F., Sun, X.M., Tanner, B.D., Lee, X.H. and Chen, J.Y., 2006b. Overview of ChinaFLUX and evaluation of its eddy covariance measurement. Agricultural and Forest Meteorology, 137: 125-137.

Zhang, J., Zhu, B. and Zhu, F., 1988. Advances in the Qinghai-Xizang Plateau Meteorology - The Qinghai-Xizang Meteorology Experiment (QXPMEX, 1979) and Research. Chinese Science Press, Beijing, 268 pp.

Zhang, Y.Q. and Tang, Y.H., 2005. Inclusion of photoinhibition in simulation of carbon dynamics of an alpine meadow on the Qinghai-Tibetan Plateau. Journal of Geophysical Research-Biogeosciences, 110.

Zhao, L., Li, Y.N., Gu, S., Zhao, X.Q., Xu, S.X. and Yu, G.R., 2005a. Carbon dioxide exchange between the atmosphere and an alpine shrubland meadow during the growing season on the Qinghai-Tibetan Plateau. Journal of Integrative Plant Biology, 47: 271-282.

Zhao, L., Li, Y.N., Zhao, X.Q., Xu, S.X., Tang, Y.H., Yu, G.R., Gu, S., Du, M.Y. and Wang, Q.X., 2005b. Comparative study of the net exchange of CO2 in 3 types of vegetation ecosystems on the Qinghai-Tibetan Plateau. Chinese Science Bulletin, 50: 1767-1774.

Zhao, L.A., Li, Y.N., Xu, S.X., Zhou, H.K., Gu, S., Yu, G.R. and Zhao, X.Q., 2006. Diurnal, seasonal and annual variation in net ecosystem CO2 exchange of an alpine shrubland on Qinghai-Tibetan plateau. Global Change Biology, 12: 1940-1953.

Appendix

A detailed documentation of the sites, an R-interface for the data exchange between TK2 and Terrafex and the R-scripts for plots of type 'Hofmüller', 'Stationartiy / ITC', 'Landuse footprints', 'QA footprints' (introduced in chapter 3.4) and the landuse distribution histograms (Figure 4-10 and Figure 4-32) are available on request from the data archive of the Department of Micrometeorology, University of Bayreuth. As well, the raw data and the entire 'work' folder including all steps of this study are archived there.

On this account, few pictures to get an impression on the 'real' sites so as to supplement the parameterizations of this study are listed here (Picture 1, Picture 2).
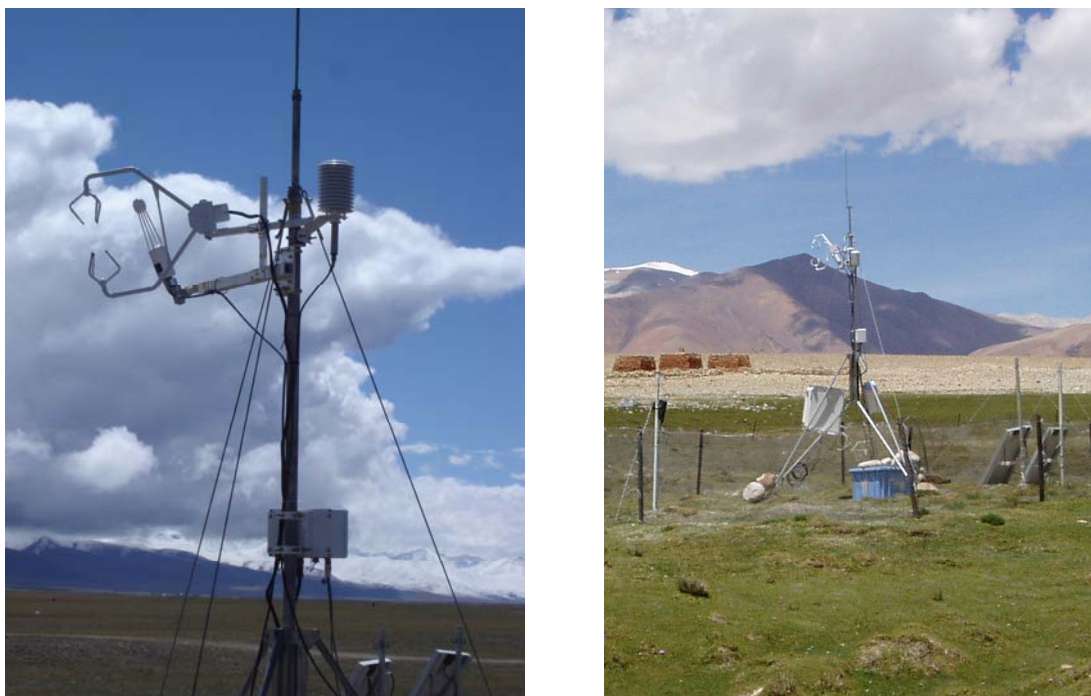
Picture 1: Installation at Namco site (left) and Everest site (right), view towards E.

Picture 2: Fetch condition at Everest site. Panorama starts on the left side from bottom to top (E to NW) and continuous on the right side from bottom to top (W to SE).

Eidesstattliche Erklärung

Ich erkläre an Eides Statt, dass ich meine Diplomarbeit „Quality assessment of Eddy Covariance measurements above Tibetan Plateau grasslands" selbständig und ohne Benutzung anderer als der angegebenen Hilfsmittel angefertigt habe, und dass ich alle Stellen, die ich wörtlich oder sinngemäß aus Veröffentlichungen entnommen habe, als solche kenntlich gemacht habe. Die Arbeit hat bisher in gleicher oder ähnlicher Form oder auszugsweise noch keiner Prüfungsbehörde vorgelegen.

Bayreuth, den 30.04.2007

_____

Stefan Metzger